# UNIVERSIDAD DE MALAGA

Tesis Doctoral por Compendio de Publicaciones

# ESTUDIOS DE PROPAGACIÓN DE GRIETAS MEDIANTE CORRELACIÓN DE IMÁGENES Y MECÁNICA DE LA FRACTURA

**Mehdi Mokhtarishirazabad**

Málaga, Marzo 2019

# UNIVERSIDAD DE MALAGA

Departamento de Ingeniería Civil, de Materiales y Fabricación

Tesis Doctoral por Compendio de Publicaciones

## ESTUDIOS DE PROPAGACIÓN DE GRIETAS MEDIANTE CORRELACIÓN DE IMÁGENES Y MECÁNICA DE LA FRACTURA

## MULTI-PARAMETER FRACTURE MECHANICS ANALYSIS OF FATIGUE CRACK PROPAGATION BY DIGITAL IMAGE CORRELATION

Autor:

MEHDI MOKHTARISHIRAZABAD

Ingeniero de Materiales- Metalurgia Industrial por la Universidad Ferdowsi de Mashhad, Irán

Director:

D. PABLO LÓPEZ CRESPO

Tesis doctoral presentada en la

ESCUELA DE INGENIERÍAS INDUSTRIALES de la UNIVERSIDAD DE MÁLAGA

para la obtención del Grado de Doctor

Málaga, Marzo de 2019

D. Pablo López Crespo, Doctor del Área de Ciencia de Materiales e Ingeniería Metalúrgica, de la Universidad de Málaga, como Director de la Tesis Doctoral.

"ESTUDIOS DE PROPAGACIÓN DE GRIETAS MEDIANTE CORRELACIÓN DE IMÁGENES Y MECÁNICA DE LA FRACTURA"

Presentada por D. Mehdi Mokhtarishirazabad en la ESCUELA DE INGENIERÍAS INDUSTRIALES de la UNIVERSIDAD DE MÁLAGA para la obtención del Grado de Doctor.

Hace constar que dicha tesis queda avalada por los siguientes artículos de investigación:

1. M. Mokhtarishirazabad, P. Lopez-Crespo, B. Moreno, A. Lopez-Moreno, M. Zanganeh, Evaluation of crack-tip fields from DIC data: A parametric study, International Journal of Fatigue, Volume 89, 2016, Pages 11-19.
2. M. Mokhtarishirazabad, P. Lopez-Crespo, B. Moreno, A. Lopez-Moreno, M. Zanganeh, Optical and analytical investigation of overloads in biaxial fatigue cracks, International Journal of Fatigue, Volume 100, Part 2, 2017, Pages 583-590.
3. Mokhtarishirazabad M, Lopez-Crespo P, Zanganeh M. Stress intensity factor monitoring under cyclic loading by digital image correlation, Fatigue & Fracture of Engineering Materials and Structures, Volume 41, 2018; Pages 2162–2171.

En Málaga, a X de Marzo de 2018

*Fdo: Pablo López Crespo*

*Director*

*Fdo: Belén Moreno Morales*

*Tutora*

To my parents, Mokhtar and Fatemeh

# Resumen

La evaluación precisa de los parámetros de fractura es crucial para estimar el comportamiento de los componentes mecánicos en condiciones de servicio. Las distintas técnicas experimentales son de gran utilidad para mejorar las predicciones y los análisis de integridad estructural en los materiales. El factor de intensidad de tensiones (SIF por sus siglas en inglés) es un parámetro comúnmente usado para estudiar la propagación de grietas de fatiga en órganos que trabajan en régimen eminentemente lineal elástico. Por esta razón, existen numerosos grupos de investigación dedicados al desarrollo de métodos experimentales, numéricos y analíticos para mejorar las estimaciones del SIF para distintas condiciones de carga y distintas geometrías. Correlación de imágenes (DIC por sus siglas en inglés) es una herramienta relativamente simple y de gran versatilidad que permite medir campos completos de desplazamientos o deformaciones en objetos sometidos a cargas. La combinación de datos obtenidos experimentalmente con soluciones analíticas como los modelos de Westergaard, Muskhilishvili o Williams, permite la estimación de los valores del SIF en muy diversos casos. Sin embargo, aspectos como la selección más idónea de parámetros experimentales o las limitaciones de esta técnica siguen generando muchas dudas en la comunidad científica. Este trabajo se centra principalmente en tres aspectos: la optimización de los parámetros experimentales de DIC para la evaluación del SIF, la medición continua del SIF mediante DIC y el estudio del comportamiento en condiciones de carga complejas (carga biaxial) con y sin la presencia de cierre de grieta. A tal efecto se ha empleado un método multi-puntos sobredeterminado que aúna la elegancia y simplicidad de los modelos elásticos con la extracción de información real del comportamiento del material en su superficie. En este caso hemos optado por el modelo elástico basado en el desarrollo en series de Williams y la medida experimental de datos en torno al vértice de la grieta se ha realizado mediante DIC. En la etapa de optimización se examinan diferentes parámetros, como el número de términos en la serie de Williams, el tamaño del campo de visión y la ubicación óptima del área de interés. El efecto de estos parámetros en la evaluación de SIF se examina y optimiza con el objetivo de mejorar la precisión en los valores del SIF, así como mejorar la estabilidad de la metodología. Con los parámetros obtenidos se observa una gran estabilidad para la evaluación continua del SIF tanto para cargas estáticas como para cargas cíclicas. Se ha estudiado también un caso de mayor complejidad pero a su vez mayor utilidad desde el punto de vista industrial como es la

aplicación de cargas biaxiales. Los resultados mostraron una buena concordancia entre las soluciones experimentales y las analíticas. Por último, en semejantes condiciones, se ha podido detectar la presencia de fenómenos de cierre de grieta en fatiga, demostrando de este modo la utilidad de estas investigaciones en condiciones de cargas variables.

# Abstract

Accurate evaluation of the fracture parameters is crucial for estimating the behaviour of the mechanical components in service condition. Experimental observations are extremely useful to provide accurate and reliable information for modern structural integrity analysis. The stress intensity factor (SIF) is a key parameter for understanding the fatigue crack propagation behaviour of structures prone to linear elastic failure. The SIF has been widely studied and a number of experimental, numerical and analytical methods have been developed and continue being developed to improve the estimation of the SIF for different loading conditions and component geometries. Digital Image Correlation (DIC) is a simple and versatile method for full-field quantification and can be used to measure experimentally the displacement data from a surface of a component being strained. By combining the experimentally evaluated displacement data with analytical solutions such as Westergard's, Muskhilishvili's and Williams' series, one is able to evaluate the SIF in cracked components. However, the selection of the experimental parameters and the limitations of the approach (e.g. the maximum permitted plasticity at the crack tip) are still a controversial concept. This work concentrates on three main topics: optimization the experimental DIC parameters for SIF evaluation, continuous measurement of SIF by DIC and evaluation of crack tip field under complex loading conditions (biaxial loading) with and without the presence of overloads. A multipoint over-deterministic method is employed to combine an elastic model based on Williams' solution for displacement distribution around the crack tip with the experimentally full field measurement of displacement at the crack tip by DIC. Different parameters such as number of terms in Williams' series, size of the field of view and the best location of the area of interest are examined in the optimisation stage. The effect of these parameters on the SIF evaluation are then tested for stable and accurate SIF estimation. The method showed a great stability for continuous evaluation of SIF under static and cyclic loads. It also successfully applied on cylindrical samples under biaxial loading and the results showed good agreement between analytical and experimental evaluation of SIF. Finally, the methodology was also employed successfully to detect crack closure effects.

# Acknowledgements

I would like to express my sincere gratitude to my supervisor Dr Pablo Lopez-Crespo for all scientific and personal supports during my PhD studies. My sincere thanks to Professor Belen Moreno for her invaluable advices in different parts of this scientific endeavour. I would also like to thank Dr Mohammad Zanganeh, from NASA Johnson Space Centre, USA, for the industrial support, Dr Kristin Hockauf from Chemnitz University of Technology, Germany and Dr Mahmoud Mostafavi from the University of Bristol, UK, for hosting me during the scientific visits that I conducted in their labs. Financial support from Junta de Andalucía through Proyectos de Excelencia grant reference TEP-3244, the University of Malaga and Campus de Excelencia Internacional del Mar (CEIMAR) through Lineas Emergentes program and for providing PhD scholarship and Ministerio de Economia y Competitividad through grant reference MAT2016-76951-C2-2-P is greatly acknowledged. Last but not least, I highly appreciate the continuous support, encourage and understanding of my family, friends and colleagues during the last four years.

# Contents

# List of Figures

# List of Tables

# 1. Introduction

In modern designs, for the sake of structural integrity, accurate and reliable estimation of the fatigue strength of the structural materials is essential. It is well recognized that materials and structures contain cracks and flaws. Therefore, Fracture mechanic approaches should be used for structural design and materials selections [1]. Although a number of parameters at a continuum level have been examined to correlate the crack propagation of flawed component, the most widely used fracture mechanics design parameter is the stress intensity factor (SIF). The SIF can completely characterizes the crack tip fields (stress, strain and displacement) in an ideally elastic material [1]. Apart from the conventional standard test methods for evaluating the SIF, it has been shown that crack-tip fields (strain, stress and displacement field) include essential information for accurate estimation of fracture parameters [2]. A number of different techniques are able to provide both surface and bulk information. Surface techniques include photo-elasticity [3], thermo-elasticity [4], Moiré interferometry [5] and digital image correlation (DIC) [6]. Bulk techniques include neutron diffraction [7]and X-ray diffraction [8]. Significant development in optical methodologies for evaluation of mechanical parameters from crack tip fields, has opened new doors toward engineers to have a more accurate estimation of fracture parameters of engineering component in service condition. Among full-field measurement techniques, DIC is widely used due to several advantageous rather other methods. DIC is technically easy to implement, no sophisticated sample preparation is needed, and it is basically a scale-free method. In other words, it can measure on the scale ranging from a few meters [9] to micro-meters [10,11]. By fitting the experimental extracted full field displacement data with available analytical solutions such as Williams' solution for crack tip fields, an experimental stress intensity factor can be determined. It should take into consideration that there are several factors which can affect the accuracy and reliability of the estimated SIF. The first section of this study is allocated to optimization the experimental DIC parameters for evaluating the SIF with high accuracy.

In the next section of the thesis, DIC is used as a robust non-destructive technique for structural health monitoring. One of the main advantages of using DIC as an NDT method, is the capability of the method to be combined with analytical solutions for monitoring the fracture parameters. That is to say, while conventional NDT methods such as infrared and thermal testing, acoustic emission, eddy current and ultrasonic have been successfully employed to monitor the defects size, DIC can be used to monitor the changes in fracture parameters (such as SIF) without the knowledge of the crack length or applied load. This is a great advantage studying complex geometries when there is no available analytical solution and numerical solution is extremely time consuming. Therefore, the hybrid method developed in the earlier sections is employed for continuous measurement of stress intensity factor of a crack under cyclic loading.

To examine the capability of DIC for more complicated loading condition, crack tip field of a sample under biaxial loading is studied in the final stage of this research. Cracks in structures are generally subjected to mixed mode loading condition, while, for the sake of simplicity, most of works tend to focus more on the simpler but less realistic case of uniaxial loading [2]. Therefore, there are many uncertainties related to the load sequence effect that is now well-known and is not normally incorporated into the crack growth models. DIC is employed as versatile full-field optical technique in combination with analytical methodology to study overloads in fatigue cracks under biaxial loading (tension-torsion).

# 2. Literature review

## 2.1. Fatigue of materials

Since the first half of nineteenth century when the first research on fatigue of materials was published [2], a huge number of researches have been conducted to determine the different types and mechanisms of fatigue of material. Nowadays, it is well-known that the majority of the failure of engineering components (50%-90%) is due to fatigue fracture [2,12]. One of the most common definition for the fatigue phenomenon in materials is determined by ASTM [13] as follows:

“The process of progressive localized permanent structural change occurring in a material subjected to conditions that produce fluctuating stresses and strains at some point or points and that may culminate in cracks or complete fracture after a sufficient number of fluctuations”.

As it can be seen from the abovementioned definition of the fatigue process, it is a localized process. That is to say, the fatigue damage occurs at local areas that experience high stress or strain. Another important keyword in the fatigue process definition is the word crack. In many safety critical parts in industry it is normally assumed that small crack-like defects (e.g. impurity, porosity, etc.) exists prior to initial use of the component. Keeping in mind that fatigue is a localized process and there is a crack which always lead to the final failure of the component, the crack tip fields seem to provide invaluable information for predicting the fatigue crack growth behaviour. To this end, Fracture Mechanics can be used as a tool to study the fatigue process. Linear Elastic Fracture Mechanics (LEFM) is one of the most common methods for analysing the fatigue process of materials provided that materials conditions during the loading are predominantly linear elastic. [1,12].

Irwin extended the Griffith's theory of brittle fracture to metals with small plastic deformation at the crack tip. To quantify the crack tip driving force, he employed the Stress Intensity Factor (SIF). The SIF is known as one of the most important fracture parameters for characterising the crack behaviour of the engineering components. Since 1957 when Irwin [14] formulised the SIF a considerable work have been done to improve our understanding on its importance in crack growth behaviour under static and cyclic loading [1,15]. Finite element method had been employed widely during last decades for detailed analysis of the crack tip fields (stress, strain, displacement) to evaluate the SIF and phenomenon such as crack closure

[16,17]. In addition, some mathematical models have been introduced describing the crack tip field. Westergaard [18] came up with a stress function describing the elastic stress distribution ahead of a crack. Williams then expanded his solution to take into account the yielding effect at the crack tip [19]. The stress field in a linear elastic cracked body subjected to external forces can be expressed as follows [1]:

$$\sigma_{ij} = \left(\frac{k}{\sqrt{r}}\right) f_{ij}(\theta) + \sum_{m=0}^{\infty} A_m r^{\frac{m}{2}} g_{ij}^{(m)}(\theta) \tag{1}$$

where $\sigma_{ij}$ is the stress tensor, r and θ represent polar coordinate system (Fig. 2), k is a constant, and $f_{ij}$ is a dimensionless function of θ in the first term. $A_m$ is the amplitude and $g_{ij}$ is a dimensionless function of the θ for the mth term. Since the leading term in the solution is proportional with $1/\sqrt{r}$ , it approaches to infinity when r → 0, while higher order terms remains finite or approach zero. That is, the stress near the crack tip is a function of $1/\sqrt{r}$. In Eq. 1, k can be replaced by SIF, K, where $K = k\sqrt{2\pi}$. For the sake of simplicity, the higher order terms are often ignored. However, it is essential to consider higher order terms to describe crack tip stress state accurately. For example, Larsson et al. [20] has shown that considering second non-singular term in Willimas' series expansion can improve the evaluation of stress state ahead of a crack tip in plane strain conditions. Effect of considering higher order terms on the accuracy of the SIF estimation is examined in section 2.1.

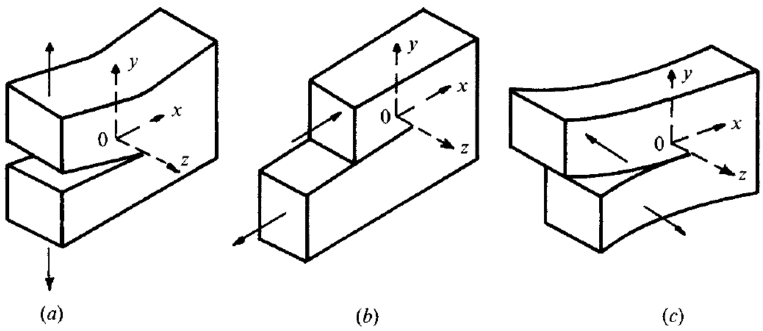


Figure 1. different modes of loading, a) Mode I (Tensile opening), b) Mode II (in-plane sliding), and c) Mode III (Anti-plane shear) [2].

Fig. 1, shows three types of loading that can be applied to a crack including tensile opening (mode I), in-plane sliding (mode II), and out of plane shear (mode III). Fig. 2, illustrates the stress distribution ahead of a through-thickness sharp crack in linear elastic isotropic body subjected to mode I loading [12].

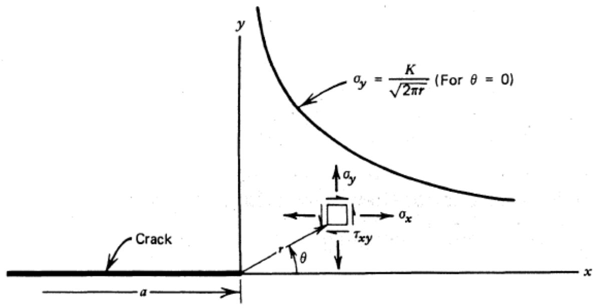


Figure 2. Definition of coordinate axis ahead of a sharp crack tip in linear elastic isotropic body subjected to mode I of loading [12].

The displacement field near the crack tip can also be described as follows [21]:

$$\begin{aligned} u &= \sum_{n=1}^{\infty} \frac{r^{\frac{n}{2}}}{2\mu} a_n \left\{ \left[ \kappa + \frac{n}{2} + (-1)^n \right] cos\frac{n\theta}{2} - \frac{n}{2} cos\frac{(n-4)\theta}{2} \right\} \\ v &= \sum_{n=1}^{\infty} \frac{r^{\frac{n}{2}}}{2\mu} a_n \left\{ \left[ \kappa - \frac{n}{2} - (-1)^n \right] sin\frac{n\theta}{2} + \frac{n}{2} sin\frac{(n-4)\theta}{2} \right\} \end{aligned} \tag{2}$$

where u and v are the horizontal and vertical displacement respectively. μ is the shear modus and $\kappa = (3 - \nu)/(1 + \nu)$ for plane stress and $\kappa = 3 - 4\nu$ for plane strain condition, $\upsilon$ is the Poisson's ratio, r and θ are radial and phase distance from the crack, a and b are constant. It can be seen from Eq.2 that by using a reverse solution, one is able to quantify the SIF if the state of crack tip field is known. For example, if by using an experimental method such as DIC, the state of the displacement field around the crack tip is determined, an experimental evaluation of SIF can be achieved.

Recently, Christopher et al. [22] introduced a new model for fatigue crack growth by including the K, T-stress , interfacial shear stresses, and a “retarding stress”. They claim that their model can identify the influence of stresses arising from plastic deformation [23] related to crack growth. All of the proposed models have been validated by experimental full-field data. Different techniques have been developed to obtain a full-field measurement of the crack tip field, experimentally, such as Moiré interferometry [5], photo-elasticity [3], thermo-elasticity [4], and DIC [6]. In section 3.3, DIC is introduced as a robust method for extracting the experimental full-field displacement data and its application for evaluating the widely used fracture parameters such as SIF is discussed.

## 2.2. Fatigue crack closure

The phenomenon in which the fatigue crack remains closed even after applying far-field tensile load, was observed and rationalised by Elber in 1970 [2]. This behaviour was attributed to elastic constraint of the material plasticly stretched along the crack flanks by growing the crack. Plasticity-induced crack closure is the term coined for this type of the crack closure [2,24,25]. Residual plastic stretch at the crack wake is not the only source of crack closure [26]. Oxide induced crack closure, microscopic crack closure, viscous fluid-induced crack closure and transformation induced crack closure are the other types of crack closure. Elber's finding suggests that fatigue crack growth rate is not depend on only the crack tip condition but also depends on the state if the materials at the crack flanks behind the crack tip [27]. Therefore, for predicting the fatigue crack growth, the load history, length of the crack and stress state are playing important roles. Fig. 3, shows how the plastic wake develops for fatigue cracks with different crack length propagating under constant amplitude of tensile stresses .The effect of crack closure can lead a deviation from Paris' Law, which can be considered in the models by introducing $\Delta K_{eff} = K_{max}-K_{op}$, where $K_{op}$ is the SIF when the crack is open fully [2,25]. A number of different methods have been developed for evaluating the $K_{op}$. In general, they can be divided in two main groups: direct methods such as optical and scanning electron microscopy observations, replica, etc, and indirect methods, in which the compliance changes during the loading cycles are measured, like back face strain and crack mouth opening displacement (CMOD) [28]. The load-displacement/strain data are then used to determine the opening load ($P_{op}$). Some of the most common methods are as follows:

- Deviation point from the linearity of the upper part of the load-displacement curve
- 1% offset slope method
- Deviation point from the linearity of the upper part of the load-differential displacement curve
- The intersection point between two tangent lines, fitted to the upper and lower linear part of the load-displacement curve

The advantages and disadvantages of each method is discussed in details by Stoychev and Kujawski [28].

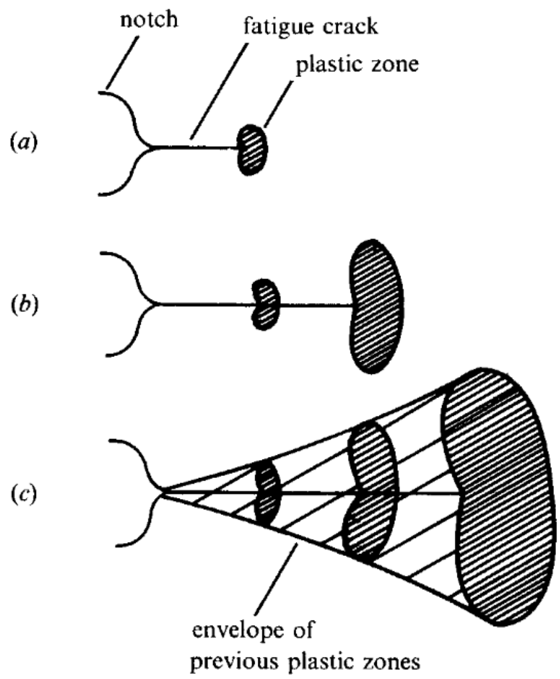


Figure 3. evolution of plastic zone at crack wake by propagating a fatigue crack [2].

## 2.3. Digital Image Correlation

Since 1980s in which a group of researchers at the University of South Carolina [29] developed the DIC method for obtaining the full-field in-plain deformation of an object directly, a growing number of researches has been done to modify the method and its parameters. DIC is a straight forward, low cost and simple method to measure experimentally surface deformation data with few advantages compared to other full-field techniques such as Moiré interferometry, photo-elasticity and thermo-elasticity. A schematic diagram of a typical two-dimensional DIC is illustrated in Fig. 4.

In brief, DIC compromises of three sequences. First step is sample preparation which includes providing a grey scale random pattern called “speckle” on the surface of the sample. Fig.4 shows an example of such speckle pattern.

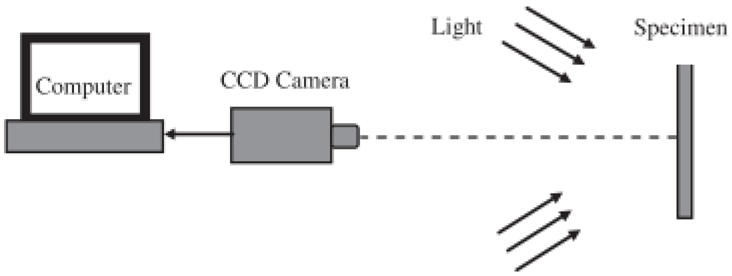


Figure 4. Schematic diagram of typical 2D DIC equipment [21]

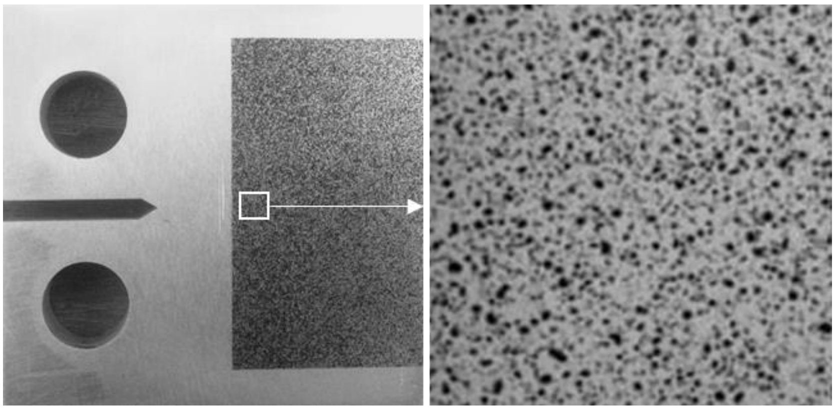

Figure 5. An example of a speckle pattern applied with spray paint on a CT sample.

This pattern can be achieved simply by spray painting the sample with white and black colours to obtain a random pattern of high contrast markers (Fig.5). Next is taking digital images before and after loading from the surface of the specimen. Each image is made of pixels with distinct grey scale intensity. Finally, DIC uses correlation algorithm to track the markers on the pattern by comparing the first image (reference image), when no load is applying to the sample, with the deformed image taken during the loading. Since the intensity of a pixel in a digital image is not unique, in the correlation method, the image is divided to smaller windows called subset which is always made of an odd number of pixels. The pattern inside the subset is then correlated with the same subset in the reference image to calculate the displacement in the centre of the subset, point P. A Taylor expansion about the point P can be used to find the displacement of P from ($x_0$,$y_0$) to ($x_1$,$y_1$), point $P^*$ as follows :

$$x_1 = x_0 + u_0 + \frac{du}{dx}\Delta x + \frac{du}{dy}\Delta y + \frac{1}{2}\frac{d^2u}{dx^2}\Delta x^2 + \frac{1}{2}\frac{d^2u}{dy^2}\Delta y^2 + \frac{d^2u}{dxdy}\Delta x\Delta y \tag{3}$$

$$y_1 = y_0 + v_0 + \frac{dv}{dx}\Delta x + \frac{dv}{dy}\Delta y + \frac{1}{2}\frac{d^2v}{dx^2}\Delta x^2 + \frac{1}{2}\frac{d^2v}{dy^2}\Delta y^2 + \frac{d^2v}{dxdy}\Delta x\Delta y \tag{4}$$

where $u_0$ and $v_0$ are the horizontal and vertical displacement of point P, respectively, $\Delta x = x_1 - x_0$ and $\Delta y = y_1 - y_0$.

Higher order terms in Eqs. 3, and 4 are used to consider the subset rotation and distortion as shown in Fig. 6. The correlation between two subsets can be established in several methods which have their own pros and cons. For example, the correlation between the two subsets (before and after deformation) can be done by minimizing a correlation factor, C:

$$C = \frac{\sum_s [G(x_0, y_0) - H(x_1, y_1]^2}{\sum_s G^2(\, x_0, y_0)} \tag{5}$$

where G and H are the grey scale light intensities corresponding to all points in the subset, S. This process performs for all subsets in the image. An overlap between neighbour subsets is set to have a sub-pixel accuracy. In this manner, a full field displacement of the area of interest (AOI) can be obtained.

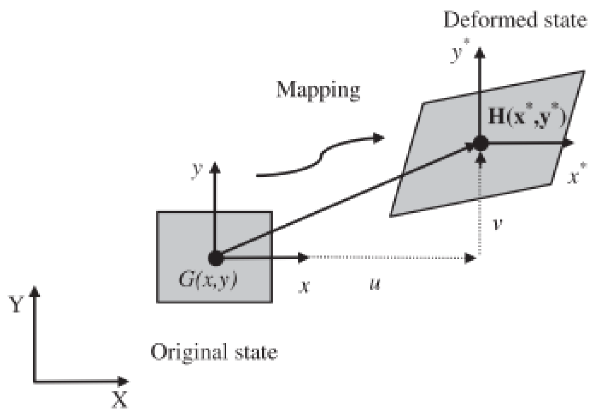


Figure 6. concept of DIC [21]

The details of the method and algorithms are comprehensively described by Sutton et al. [16].

## 2.4. Multi parameters fracture mechanics

Based on classical fracture mechanics theories, a single parameter like $K_I$ or J can characterise the stresses or strains near the crack tip under small scale yielding condition where the size of plastic zone is negligible comparing the crack length and size of the body [1,30].

However, in the presence of excessive plasticity, single-parameter fracture mechanics is not valid anymore and fracture toughness becomes dependent on size and geometry of the sample. Higher order terms in Williams' infinite power series become more and more important at the presence of considerable crack tip plasticity. For example, second term in the Williams' series, known as T-stress, remains finite at the crack tip and it is independent of the distance from crack tip. It has been shown that T-stress has a considerable effect on the state of stresses and strains near the crack tip, as a result on the shape of plastic zone at the crack tip [1]. A number of studies have been conducted to evaluate the effect of higher order term on stress or strain state ahead of a crack tip. Utilising an over-deterministic least square method for evaluating mixed mode stress field parameters by the technique of photoelasticity, Ramesh et al. [3] showed the importance of using multi-parameter stress equations for solving real life problems where displacement data are collecting from a large area. They used the fringe order minimisation error as their convergence criteria. The method was tested in three different geometries and for those data, a minimum of 6 parameters were required to obtain a convergence error less than 0.1 in fringe order (N) in modes I and II.

Yoneyama et al. [31], suggested determining SIF by adopting the convergent values (considering more than 7 terms). A nonlinear least square method was used in their research for estimating SIF from displacement data provided by DIC from a FOV of $6 \times 5$ mm$^2$. Abovementioned studies show the importance of considering higher order terms in determination of the state the crack tip fields. It is also true when the experimental displacement field is used for evaluation of K ahead of a crack, especially when data are collecting from larger area. Selecting a suitable number of terms for evaluation go SIF from experimental data is one of the concerns of this study.

### 2.5. DIC parameters affecting the estimation of K

Experimentally, DIC measurement accuracy can be affected by several factors, such as subpixel optimization algorithm, subset size, image quality, etc. [32]. It is evident that the more accurate displacement data, the more reliable estimation of SIFs. While the random error in any measurement is the inherent part of each measurement, systematic error is predictable and is typically constant and proportional to the true value [33]. Systematic errors in DIC as a result of intensity interpolation, overmatched and under-matched subset shape function has been explored by Schreier et al. [34,35] and Yu et al. [36]. A thorough study on the errors caused by different bit depths of the image, image saturation in respect with subset size, speckle pattern and subset shape function on synthetic images has been conducted by Fazzini et al. [37]. It was shown that decreasing the encoding of the images and overexpose of the speckle deteriorate the measurements by a factor of 2 and 10 respectively. Pan [38] proposed a reliability-guided DIC method which is applicable to images with shadows, discontinuous areas, and deformation discontinuities. In optic literature, the size of the DIC image is studied through the field of view (FOV) and is defined as the angular extent for a given scene imaged by a camera [16]. Since the FOV determines the number and position of data points for a constant subset size, the FOV must be taken into consideration as key parameter for SIF evaluation from DIC data. A considerable discrepancy has been observed in the literature in evaluation of SIF using DIC method due to selecting different experimental or analytical parameters. For example, Vasco-Olmo et al. [39], evaluated the fatigue crack shielding by analysing displacement field data obtained by 2D DIC and utilizing four different models. They reported that the CJP model showed an extraordinary potential for the evaluation of the crack-tip shielding during fatigue crack growth. A finite element analysis of the stress field ahead of a cracked plate has been conducted by Berto and Lazzarin [40,41]. They were able to obtain good estimations of the stress field in a very small area ahead of the crack-tip (r = 0.01 mm) by using KI, KII and T-stress in Williams' solution. In addition, they were also able to describe the stress field in larger areas by considering the first 7 terms in the series. Dehnavi et al. [42]estimated the SIF of a polycarbonate plate by DIC method (subset of 21 × 21 pixels) considering 4 terms of Williams' series taking a similar approach to Berto and Lazzarin.

The differences between all works above mentioned suggest that there exists a number of parameters that can influence the SIF estimations. These include the magnification factor, the FOV, the subset size, the dimensions of the AOI, the portion of crack included in the AOI, the masking of the crack-tip plastic zone and the number of terms considered in the analytical solution. Table 1, summarises the parameters that have been used in some of the most relevant works that estimated SIF from DIC.

Table 1, shows a clear discrepancy in the parameter selection for different works. Authors provided little or no justification for employing different parameters than previous published works. Therefore, in the first attempt, the influence of the different parameters involved in estimating the SIF with DIC technique is studied in a structured way.

Table 1. Parameters used in previous works for estimating the SIF with DIC

| Author | FOV ($mm^2$) | Crack portion inside AOI (λ) | Subset size (pixel) | Excluding plastic zone | No. of higher order terms |
|---|---|---|---|---|---|
| Peters et al. [43] | 8 | crack included | not-mentioned | not mentioned | convergence value |
| McNeill et al. [6] | 12.7 × 12.7 | 65% | not mentioned | No | up to 48 terms |
| Yoneyama et al. [31] | 6 × 5 | 50% | not mentioned | No | up to 10 terms |
| Hamam et al. [44] and Roux et al. [45] | 2 × 2 | 65% and 45% | 12 | Yes | sub/super singular terms |
| Yusof et al. [46] | ~ 12 | 50% | 12 | Yes | Muskhilishvili's app. |
| Lopez-Crespo et al. [47] | 18 × 24 | 50% | 32 | Yes | Muskhilishvili's app. |
| Yates et al. [21] | 22 × 16 | 30% | not mentioned | No | up to 15 terms |
| Dehnavi et al. [42] | not-mentioned | 30% | 21 | Yes | 4 terms |

## 2.6. Continuous measurement of SIF under cyclic loading by DIC

In the second part of this study, after optimizing the DIC parameters for evaluation of SIF, the capability of this technique is examined for continuous measurement of the SIF on a sample under cyclic loading. In this manner, DIC perceived as a non-destructive testing (NDT) method for structural health monitoring. The accuracy for structural health monitoring has been vastly improved over the last few decades thanks to the development and improvement of a wide range of techniques for monitoring the crack (damage) initiation and growth in engineering structures. Among these, NDT techniques have been extremely useful for crack monitoring. Infrared and thermal testing [48], acoustic emission [49], eddy current [50,51] and ultrasonic [52,53] are among the most popular NDT techniques for monitoring the defect size. In addition, some efforts were aimed at improving the accuracy of these techniques by combining two or more of these techniques. For example, DIC has been coupled with acoustic emission technique to determine the critical stage of deformation mechanism at the onset of the plasticity of AZ31 Mg alloy [54]. Nevertheless, most of these methods have some disadvantages that make them difficult to be adapted for industrial environments such as being very expensive and limited application to a narrow range of materials and type of defects to be detected. For example, in ultrasonic method the accuracy is highly dependent on the operator skills and it is not suitable for detecting short cracks [55]. The application of eddy current method is also limited to electrically conductive materials and interpretation of complex signals requires a highly skilled operator [56]. Due to the nature of the signal source, acoustic emission method is not perfectly reproducible and it is not capable of detecting elastic deformation [57].

While the previously described methods are used to determine the crack geometry and length, accurate damage assessment of engineering structures subjected to changing loads often requires fracture parameters of the component to be evaluated. To this end, full field techniques such as DIC [6] have been developed to characterise crack tip fields in terms of strain, stress and displacement. As it was mentioned in the previous section, SIF is a key parameter for fatigue life prediction of engineering components prone to linear elastic failure. The prominent advantage of using the crack tip fields for evaluating SIF is that no previous knowledge of crack length, applied force or specimen geometry is needed. This makes it very suitable for characterisation of in-service engineering components [58]. DIC has been employed [47] to study the effect of crack closure and crack tip plasticity in the evaluation of SIF for specimens under different mixed-mode loads (I+II). Very promising results were obtained in early studies while estimating the SIF with DIC on C-specimens and three-point-bend specimens [6]. Improvement in digital photography allowed higher resolution images that improved the accuracy in estimating the SIF both under pure mode I and a range of mixed-mode conditions [31]. Edge-finding routines for locating the crack tip were subsequently incorporated to the program to automate the evaluation of SIF with DIC displacement data [59]. The crack-tip location was also evaluated from displacement fields with a number of numerical procedures, including reflective Newton method, Nelder-Mead Simplex method, genetic algorithm and Pattern Search method [60]. DIC also allowed other forms of crack evaluation through different parameters. For example, T-stress and crack tip opening angle were evaluated on double cantilever specimens made of 7010 T7651 aluminium alloy [21]. Elastic plastic crack assessment was achieved with different methodologies. The J-integral was estimated from a combination of DIC and finite element method displacements by applying the path and domain integral methods on annealed and unannealed pure aluminium A1050 [61]. crack opening displacement (COD) measurements obtained with high magnification DIC were used to evaluate crack growth and closure mechanisms for different thicknesses on 6082 T6 aluminium alloy [62]. The plastic zone ahead of the crack [63] as a way to control the rate of crack growth was assessed with DIC on specimens with artificial cracks [64] and on specimens with real fatigue cracks [65]. To examine the capability of the proposed hybrid method, in the second part of this study, for the first time, a DIC methodology is used for continuous monitoring of the effective SIF under a range of different cyclic levels [66].

## 2.7. Capturing complex load history by DIC

While fracture problems can be simplified by considering mode I of loading, cracks in structural materials are generally under mixed-mode loading condition [2]. Therefore, estimation of the fracture parameters based on mixed-mode loading condition will be more representative of the material fracture behaviour under the actual working condition. Different optical methods have been used for obtaining full-field information required for mixed-mode loading analysis previously. Sanford and Dally [67] have determined the mixed-mode SIFs by utilising isochromatic fringes near the crack-tip. They have reported that employing an over-deterministic approach on the data points provided by the full filed fringe patterns led to a highly accurate SIF estimation. Displacement fields derived by DIC technique have been utilised by Yoneyama et al. [31] to evaluate the mixed-mode SIFs of a polymer (polymethyl-methacrylate). While they used a non-linear least square method for their solutions, Réthoré et al. [68] have developed a method based on the Lagrangian conservation law for mixed-mode SIFs estimations. A good agreement between analytical displacement fields generated based on the Muskhilishvili's complex function approach and the experimentally measured displacement fields (obtained by DIC) has been also reported by Lopez-Crespo et al [69]. The combined effect of OL and biaxial loading has been studied by potential drop technique [70].

Full-field optical techniques are very advantageous compared to other more traditional techniques. They are very versatile and can be used to study a wide range of aspects related to the OL, including evaluation of the plastic region, changes in the stress field due to the OL or experimental estimation of fracture mechanics parameters. Nevertheless, as it is described previously, they have been mostly applied to the uniaxial problem. In reality, most mechanical components are subjected to complex loading conditions with varying magnitude and direction. Therefore, it is desirable to apply full-field optical techniques to more complex loading conditions. In the last part of this work, a comprehensive optical and analytical methodology is used to study overloads [71] in fatigue cracks under biaxial loading. Most experimental information is extracted from full-field DIC data. Specimens with and without overloads are compared in terms of crack growth rate, COD and SIF [72].

# 3. Methodology

The experimental part of the work is explained in detail in ANNEXES I-III. Hereafter, only a summary of each experiment is presented. In general, all experiments were included taking images of a sample under cyclic loading following the post processing of the images for extracting the displacement field near the crack tip using the commercial software VIC-2D. The displacement data were then analysed using the routine used by Yates et al [21] to calculate an experimental SIF. The displacement data near the crack wake were also used for measuring the COD which were consequently used for measuring the opening load and effective SIF. Crack tip location were identified directly from the images at maximum load in each cycle using high magnification lenses.

## 3.1. Optimizing DIC parameters for SIF measurement

The uniaxial cyclic loading was applied on a CT specimen which were extracted and machined in T-L direction (crack propagation along rolling direction) from a 2024-T351 aluminium alloy plate according to ASTM E-647 [73]. Fig. 7, illustrates the specimen geometry and dimensions. The mechanical properties of the material are summarised in Table 2. The sample surface was scratched with abrasive SiC sand paper to obtain a random grey intensity distribution required for DIC technique. Cyclic loading was applied then with a 100kN Instron servo-hydraulic testing machine. The sample for parametrical study was pre-cracked under mode I load at a frequency of 10 Hz, a load ratio (R) of 0.1 and a stress intensity range ($\Delta K_I$) of 8 MPa√m so that the crack length was 20.30 mm (a/W = 0.40). Displacements were then measured under R = 0.3 and $\Delta K_I$ = 11 MPa√m. Small scale yielding conditions were met in all tests.

Table 2. Mechanical properties of 2024-T351 Aluminum alloy

| Young modulus, GPa | Yield Stress, MPa | UTS, MPa | Elongation at break, % | Brinell Hardness |
|---|---|---|---|---|
| 73 | 325 | 470 | 20 | 137 |

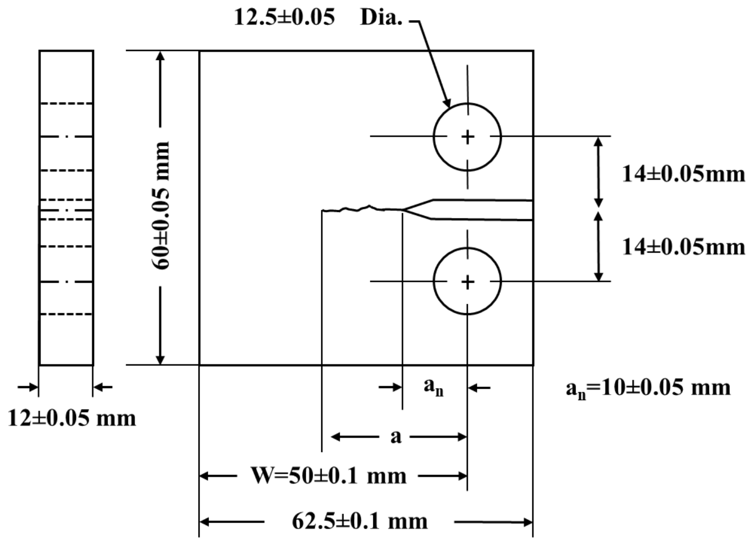


Figure 7. Geometry of the CT specimen in accordance with ASTM standard [73].

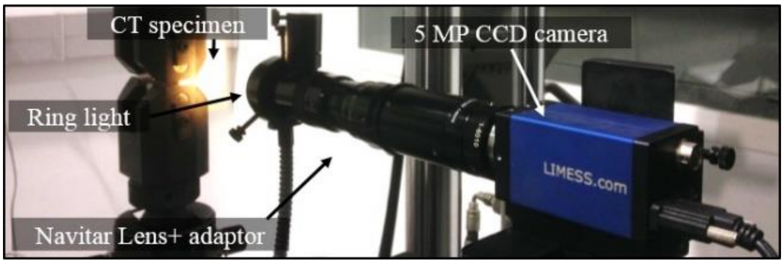


Figure 8. Imaging configuration for DIC.

An 8-bit 2452×2052 pixels CCD camera with the maximum frame rate at full resolution of 12 was used for taking images. Fields of view between 0.98×0.82 $mm^2$ and 13.5×11.3 $mm^2$ were imaged with a combination of a macro Navitar lens and an adaptor tube (see Fig. 8). In order to acquire a sufficient number of images (38 images per cycle), the loading rate was reduced to 0.1 Hz while capturing the images. Vic-Snap software [74] has been utilised for capturing the images and the corresponding applied load on the specimen for each image. Step size (the distance between two consecutive displacement vectors) was set to 1/4 of the subset size in order to achieve independent and non-repetitive data. A high-order interpolation scheme of optimized 8-tap spline was used to achieve sub-pixel accuracy. The correlation criterion was set to the zero-normalized sum of squared differences which is insensitive to offset and scale in lighting [16].

DIC test was done in different subset sizes ranging from 13 to 199 pixels for two different magnifications of 0.75× and 0.35×. The obtained displacement data was then fitted into Williams' series [19]:

$$Mode\ I \begin{cases} u_I = \sum_{n=1}^{\infty} \frac{r^{\frac{n}{2}}}{2\mu} a_n \left\{ \left[ \kappa + \frac{n}{2} + (-1)^n \right] cos \frac{n\theta}{2} - \frac{n}{2} cos \frac{(n-4)\theta}{2} \right\} \\ v_I = \sum_{n=1}^{\infty} \frac{r^{\frac{n}{2}}}{2\mu} a_n \left\{ \left[ \kappa - \frac{n}{2} - (-1)^n \right] sin \frac{n\theta}{2} + \frac{n}{2} sin \frac{(n-4)\theta}{2} \right\} \end{cases} \tag{6}$$

$$Mode\ II \begin{cases} u_{II} = -\sum_{n=1}^{\infty} \frac{r^{\frac{n}{2}}}{2\mu} b_n \left\{ \left[ \kappa + \frac{n}{2} + (-1)^n \right] sin \frac{n\theta}{2} - \frac{n}{2} sin \frac{(n-4)\theta}{2} \right\} \\ v_{II} = \sum_{n=1}^{\infty} \frac{r^{\frac{n}{2}}}{2\mu} b_n \left\{ \left[ \kappa - \frac{n}{2} + (-1)^n \right] cos \frac{n\theta}{2} + \frac{n}{2} \cos \frac{(n-4)\theta}{2} \right\} \end{cases} \tag{7}$$

where $u_I$ and $v_I$ are horizontal and vertical displacements in mode I and mode II, $\mu$ is the shear modulus and $\kappa = (3 - \nu)/(1 + \nu)$ for plane stress and $\kappa = 3 - 4\nu$ for plane strain condition, $\nu$ is the Poisson's ratio, $r$ and $\theta$ are radial and phase distance from the crack, $a_n$ is constant. Displacement field can be written in a matrix form by defining $f_{n,m}(r,\theta)$, $g_{n,m}(r,\theta)$, $h_{n,m}(r,\theta)$, and $l_{n,m}(r,\theta)$ as follows:

$$\begin{Bmatrix} u_1 \\ \vdots \\ u_m \\ v_1 \\ \vdots \\ v_m \end{Bmatrix} = \begin{bmatrix} f_{1,1} \cdots f_{n,1} & g_{1,1} \cdots g_{n,1} \\ \vdots & \vdots \\ f_{1,m} \cdots f_{n,m} & g_{1,m} \cdots g_{n,m} \\ h_{1,1} \cdots h_{n,1} & l_{1,1} \cdots l_{n,1} \\ \vdots & \vdots \\ h_{1,m} \cdots h_{n,m} & l_{1,m} \cdots l_{n,m} \end{bmatrix} \begin{Bmatrix} a_1 \\ \vdots \\ a_n \\ b_1 \\ \vdots \\ b_m \end{Bmatrix} \tag{8}$$

$$\begin{aligned} f_{n,m} &= \frac{r_m^{\frac{n}{2}}}{2\mu} \left\{ \left[ \kappa + \frac{n}{2} + (-1)^n \right] \cos \frac{n\theta_m}{2} - \frac{n}{2}\ cos \frac{(n-4)\theta_m}{2} \right\} \\ g_{n,m} &= \frac{-r_m^{\frac{n}{2}}}{2\mu} \left\{ \left[ \kappa + \frac{n}{2} - (-1)^n \right] \sin \frac{n\theta_m}{2} - \frac{n}{2}\ sin \frac{(n-4)\theta_m}{2} \right\} \\ h_{n,m} &= \frac{r_m^{\frac{n}{2}}}{2\mu} \left\{ \left[ \kappa - \frac{n}{2} - (-1)^n \right] \sin \frac{n\theta_m}{2} + \frac{n}{2}\ sin \frac{(n-4)\theta_m}{2} \right\} \\ l_{n,m} &= \frac{r_m^{\frac{n}{2}}}{2\mu} \left\{ \left[ \kappa - \frac{n}{2} + (-1)^n \right] \cos \frac{n\theta_m}{2} + \frac{n}{2}\ cos \frac{(n-4)\theta_m}{2} \right\} \end{aligned} \tag{9}$$

Eqs. 6 and 7 can be written in terms of the SIF and T-stress as follows [21]:

$$u = \frac{K_I}{2\mu}\sqrt{\frac{r}{2\pi}} cos\frac{\theta}{2}\left(\kappa - 1 + 2\,sin^2\frac{\theta}{2}\right) + \frac{K_{II}}{2\mu}\sqrt{\frac{r}{2\pi}} sin\frac{\theta}{2}\left(\kappa + 1 + 2\,cos^2\frac{\theta}{2}\right) + \frac{T}{8\mu} r(\kappa + 1)\,cos\,\theta \quad (10)$$

$$v = \frac{K_I}{2\mu}\sqrt{\frac{r}{2\pi}} sin\frac{\theta}{2}\left(\kappa + 1 - 2\,cos^2\frac{\theta}{2}\right) - \frac{K_{II}}{2\mu}\sqrt{\frac{r}{2\pi}} cos\frac{\theta}{2}\left(\kappa - 1 - 2\,cos^2\frac{\theta}{2}\right) + \frac{T}{8\mu} r(\kappa - 3)\,sin\,\theta \quad (11)$$

It can be shown that

$$K_I = a_1\sqrt{2\pi}\ , \quad K_{II} = -b_1\sqrt{2\pi}\ , \quad T = 4a_2$$

where $K_I$ and $K_{II}$ are the mode I and II of the SIF, respectively, and T represents T-stress. The effects of adding non-singular terms [75] (up to 10 terms) in Williams' solution was also explored.

The results were then validated by comparison with nominal SIF solution ($K_{I\ nom}$) [76]. Since nominal values do not include any closure effect, care was taken to generate results with as little influence as possible from closure-related mechanisms. To this end, $\Delta K_I$ and load ratio were higher during the cycles used for evaluating the SIF than during the pre-cracking process. [77].

The accuracy of experimental results was then examined through the δ parameter defined as follows:

$$\delta = \left|\frac{K_{I\,\mathrm{exp}} - K_{I\,\mathrm{nom}}}{K_{I\,\mathrm{nom}}}\right| \times 100 \quad (12)$$

where $K_{I\ exp}$ is evaluated with equation (1) and $K_{I\ nom}$ is computed from [76]. Low δ indicates more accurate estimations of $K_I$.

In order to evaluate the effect of the AOI position, λ is defined as:

$$\lambda = \frac{a_{in}}{L} \times 100 \quad (13)$$

where $a_{in}$ is the length of a part of the crack inside AOI and L represents the longitude length of the AOI.

To study the effect of the size of the AOI on the estimation of SIFs, six different AOIs in a constant FOV were analysed (Fig. 9). Minimum required data points in an AOI of $1 \times 1$ mm$^2$ for an estimation error less than 10% (δ) is also examined.

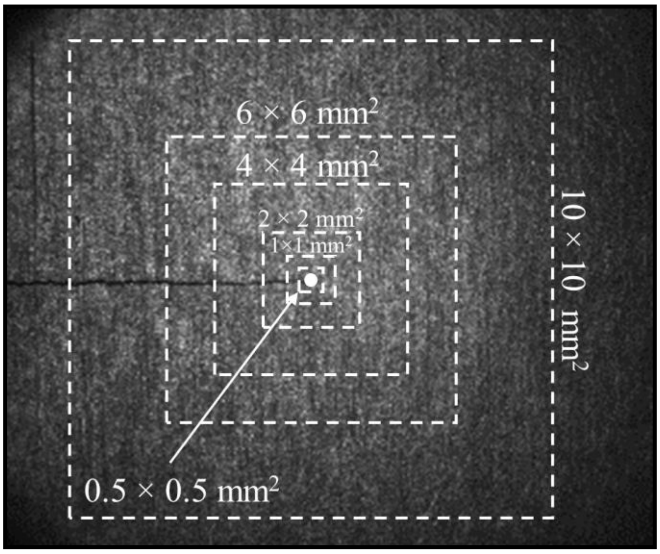


Figure 9.The difference between FOV and AOI. The FOV is the size of the whole image. Six different AOIs are defined within the FOV when λ = 50%.SIF monitoring:

## 3.2. SIF monitoring by DIC

The experiment of this part is similar to the previous part, except for the loading sequences in which the cyclic loads were applied in a ramp wave form with load ratio of 0.3 with five different applied nominal $\Delta K_I$ of 10, 15, 20, 25 and 30 MPa√m. At the end of cyclic loads, the load was increased constantly until the sudden fracture of the sample occurs under load control. Fig. 10, shows the schematic of the loading sequences.

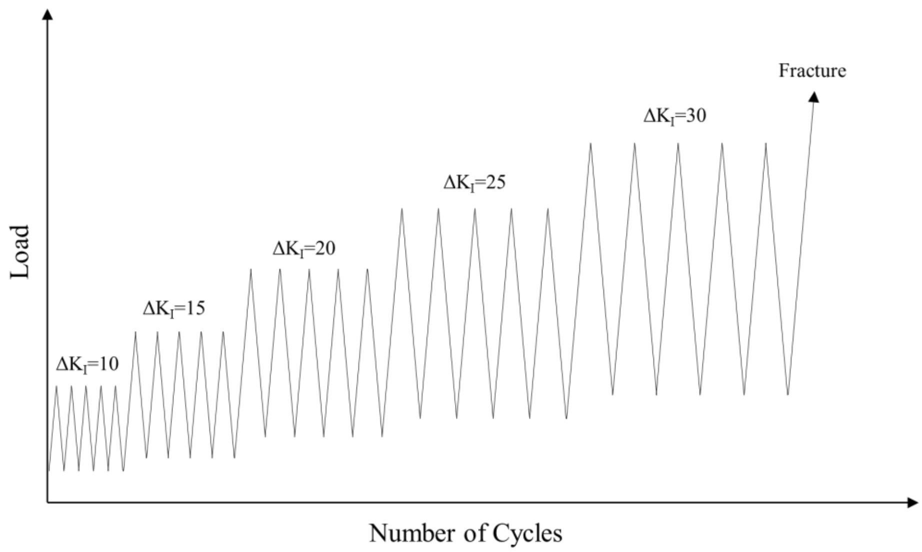


Figure 10. Schematic of loading sequences.

## 3.3. Biaxial experiment

In the third part of this work, crack propagation in a low carbon steel (St-52-3N) was studied by using DIC. Fig. 11, illustrates the microstructure of the material obtained by optical microscope which shows the ferrite and pearlite bands [78]. The mechanical properties of the alloy are given in Table 3. A schematic of the geometry is shown in Fig. 12.

Table 3. Monotonic properties of St-52-3N steel.

| | |
|---|---|
| Yield stress, $\sigma_y$ | 386 MPa |
| Ultimate tensile stress, $\sigma_u$ | 639 MPa |
| Young's modulus, E | 206 GPa |
| Shear Modulus | 78 GPa |

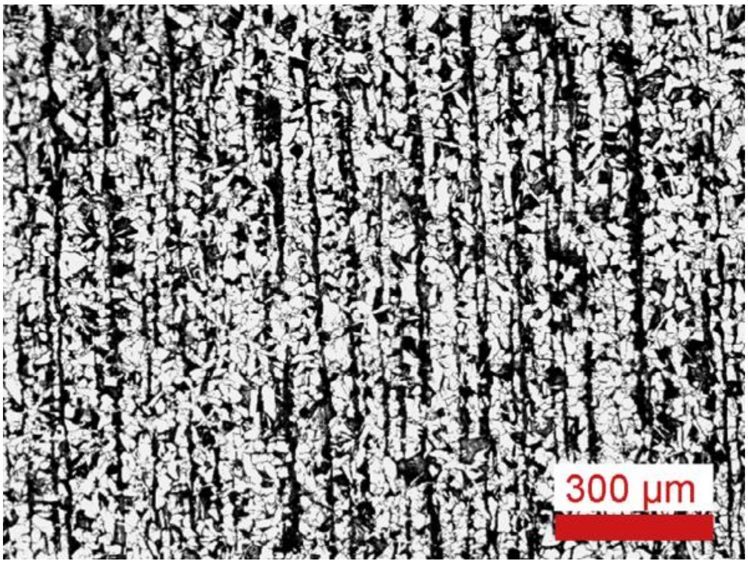


Figure 11. The microstructure of St52-3N steel. Black and white vertical bands are showing the pearlite and ferrite bands, respectively[78].

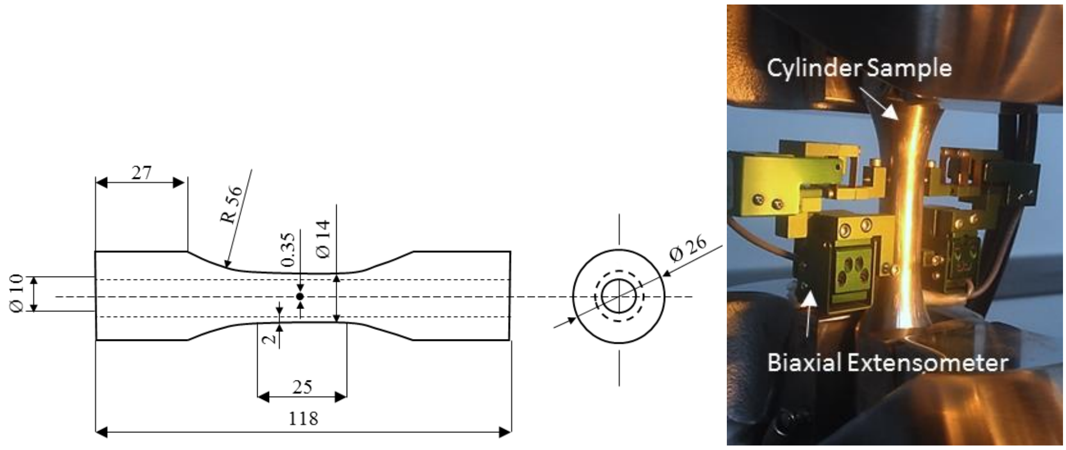


Figure 12. The geometry of the hollow cylinder specimen with a central hole. All dimensions are in mm.

An MTS 809 servo-hydraulic loading rig coupled by a biaxial extensometer Epsilon 3550 was used to apply biaxial loads under stress control mode in a similar way to previous works [79,80]. In-phase cyclic sinus signal with axial load ratio of 0.1 ($R_a$ = 0.1) and torsional load ratio of -1 ($R_t$ = -1) was applied in air at room temperature. A hole with a diameter of about 0.35 mm was drilled in the outer surface of the specimen in order to enforce the crack to nucleate inside the FOV (Fig. 12).

In order to study the effect of the overload (OL) on the crack propagation behaviour, single OL cycle ($\Delta\sigma_{OL}$, $\Delta\tau_{OL}$) was applied on specimens on the half of the final crack length with the axial and torsional load ratio of 0.1 and -1, respectively. Tests were performed under two different baseline loads. Single OL cycles of 40% and 100% were applied on S2 and S4 samples respectively. The secant method recommended in ASTM standard [73] has been employed to examine the rate of the fatigue crack growth. Table 4 shows the loading condition for samples with and without OL.

Table 4. Axial and shear stress values for specimens with and without OL cycle.

| Specimen | Crack length at OL (μm) | $\Delta\sigma$ (MPa) | $\Delta\tau$ (MPa) | $\Delta\sigma_{OL}$ (MPa) | $\Delta\tau_{OL}$ (MPa) |
|---|---|---|---|---|---|
| S1 | - | 216 | 277 | - | - |
| S2 | 669 | 216 | 277 | 302.4 | 388 |
| S3 | - | 162 | 230 | - | - |
| S4 | 689 | 162 | 230 | 324 | 460 |

In addition, to evaluate the closure level, near tip COD was measured by DIC [62,81]. Fig 13 shows the positions of the virtual extensometer and crack initiation angle for S2 sample as an example.

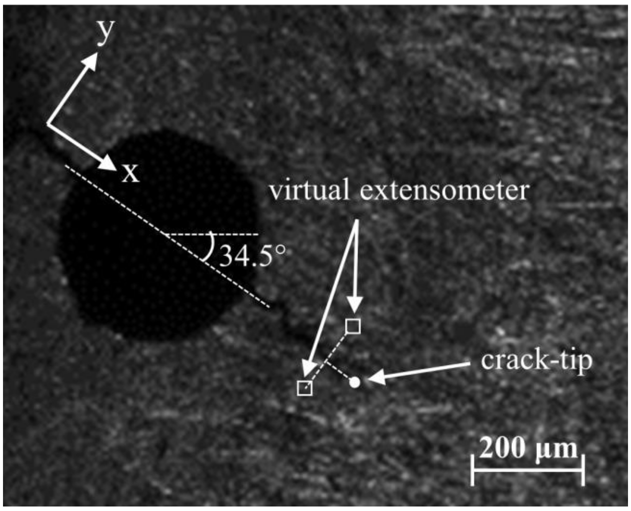


Figure 13. The position of virtual extensometers for COD examination. The white bold mark shows the crack-tip position.

The effect of single OL was studied by observing the evolution of the crack length versus the number of cycles. Fig. 14 shows how applying a single OL cycle can affect the crack growth behaviour for two different baseline loads. Fig. 14.a, shows that high loads produced lives of 58000 and 66000 cycles for the specimens with no OL (S1) and with OL (S2), respectively. Fig. 14.b, shows that low loads produced lives of 136000 and 138000 cycles for the specimens with no OL (S3) and with OL (S4), respectively. The crack growth rate is plotted as a function of crack length in Fig. 15. The overall higher da/dN values in Fig. 15.a than in Fig.15.b indicate that growth rates observed in high load tests are on average 8 times faster than rates in low load tests.

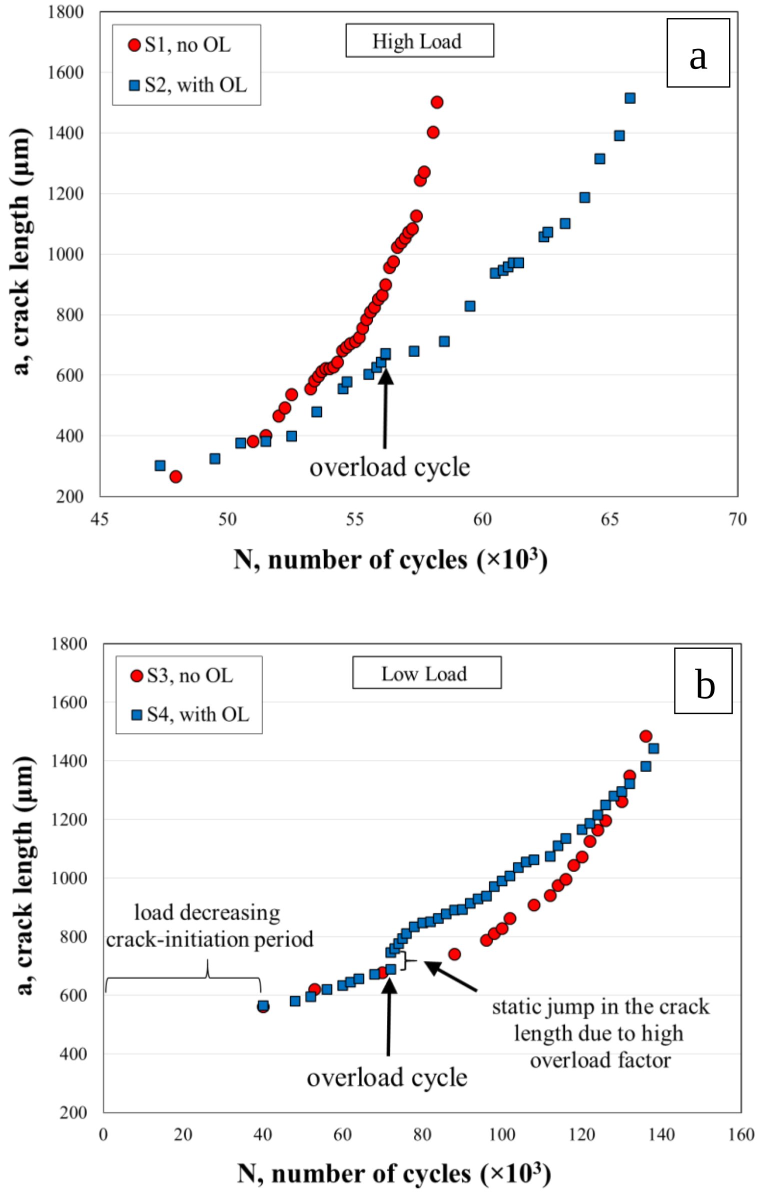


Figure 14.. Evolution of crack length versus number of cycles for samples with and without OL cycle, a) samples S1 and S2 under higher cyclic loads, b) samples S3 and S4 under lower cyclic loads.

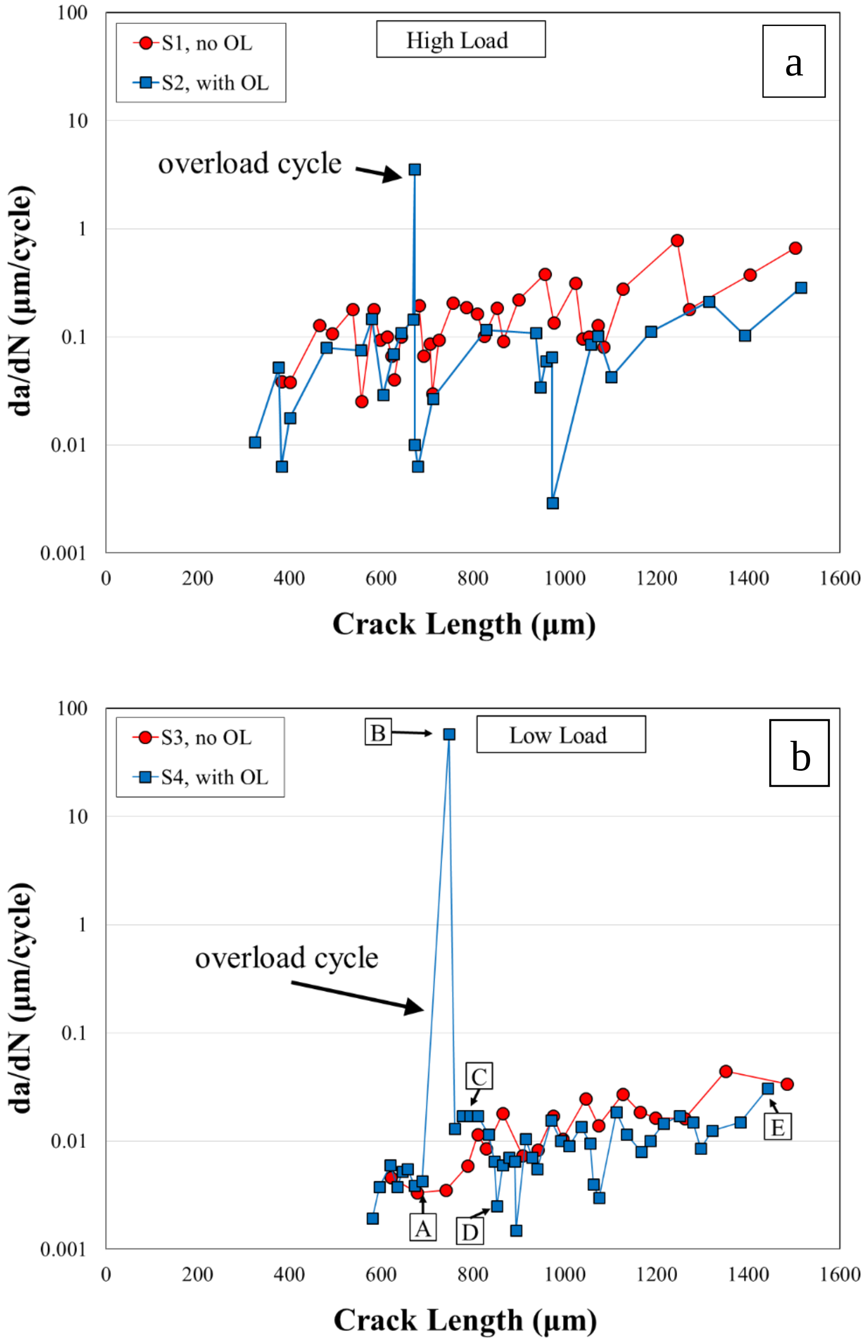


Figure 15. Crack growth rate as a function of the crack length for high (a) and low (b) baseline cyclic load.

The displacement field were extracted by DIC with the similar parameters as for previous experiment. By taking to account the size of the AOI (0.4 ×0.4 mm$^2$), two terms in the Williams' solution were used as suggested in [82].

In order to extract the vertical and the horizontal displacements with respect the axial loading axis, captured images have been rotated so that the crack appears horizontal in all images. Fig. 16, illustrates the vertical displacement contour for an AOI around a crack with a length of 0.689 mm (sample S2). The images were rotated 37° clockwise so that the crack line was horizontal [59]. Displacement data points inside an area of 0.4×0.4 $mm^2$ were extracted and fitted to Williams' solution in order to calculate SIFs.

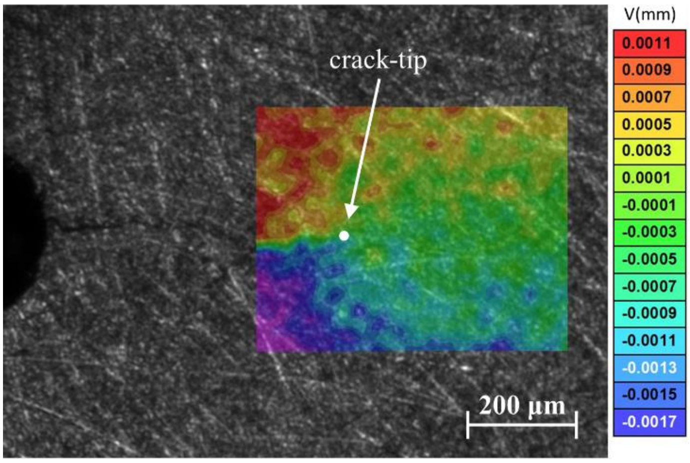


Figure 16. The position of the AOI for deriving the displacement field ahead of a crack with the length of 0.669 mm after 53500 cycles (sample S2). The image has been rotated, so that the crack line becomes horizontal.

The COD was also evaluated from the DIC data. A post processing routine was developed to measure the COD with a virtual extensometer as follows:

$$COD(x) = v_{bot} - v_{top} \tag{14}$$

where v is the vertical displacement and x is the distance of the extensometer behind the crack-tip (here x = 60 μm). The subscripts "top" and "bot" refer to the position of the virtual extensometer points relative to the crack line. The compliance based algorithm proposed by Skorupa et al. [83] has been utilised to study the fatigue crack closure in this paper. This method has been used by other authors for characterising fatigue crack closure using local compliance measurements [84].

# 4. Results and discussion

## 4.1. Optimizing DIC parameters for SIF measurement

In the first part of the experiments, the experimental parameters of DIC method for evaluation of the SIF were examined. It was observed that by increasing the subset size from 13 to 200 pixels (FOV = 6 × 6 mm$^2$), the E (standard Deviation Confidence Interval) decreased while the error of SIF estimation ($\delta$) increased steadily. Increasing $\delta$ as a result of enlarging the subset size is probably due to the low resolution in the displacement field in the crack-tip region, where large gradients occur.

It was also observed that omitting or considering the crack tip plastic zone in the post-processing step does not have a considerable effect on the estimation of SIF. This behaviour can be explained by noting that, unlike with stress field, there is no singularity at the crack-tip for displacement field [85].

To study the effect of the area where displacement data are collecting relative to the crack tip position, the $\lambda$ parameter was introduced in section 2. The results of estimating the SIF for different $\lambda$ parameters and different FOVs are summarised in Fig. 17. The curves corresponding to different FOVs show a minimum in $\delta$ for $\lambda$ parameter of 25%. That is, for all FOVs, the best results are obtained when the crack-tip is included in the AOI and crack extends over one fourth of the FOV.

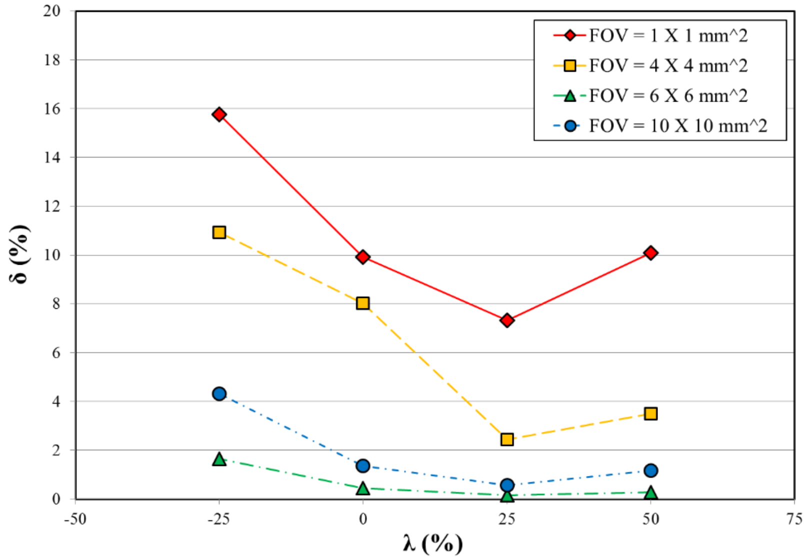


Figure 17. The behaviour of δ as a function of λ for different FOVs. Nine terms in Williams' expansion were used in all cases.

The next parameter that will be studied is the size of the FOV. It was observed that beyond FOV larger than 4 mm, more terms of Williams expansion are required to obtain good estimations. This behaviour is logical since higher order terms are required for describing accurately large crack-tip fields.

The effect of selecting different sizes of AOI in a large FOV was also investigated and it was observed that using a small AOI (even one-tenth of the FOV) will result in the same accuracy as using small FOV by utilising high magnification lenses. One of the advantages of using small AOI is the fewer number of data points required to be analysed.

This observation suggests that the system of equations solved to evaluate the SIF is excessively and unnecessarily over-determined. The degree of over-determination in the multi-point over-deterministic method can be studied through the parameter φ, defined as:

$$\varphi = \frac{\text{number of data points}}{\text{number of terms in series}} \tag{15}$$

Fig. 18 shows the accuracy of SIF estimation for different values of φ.

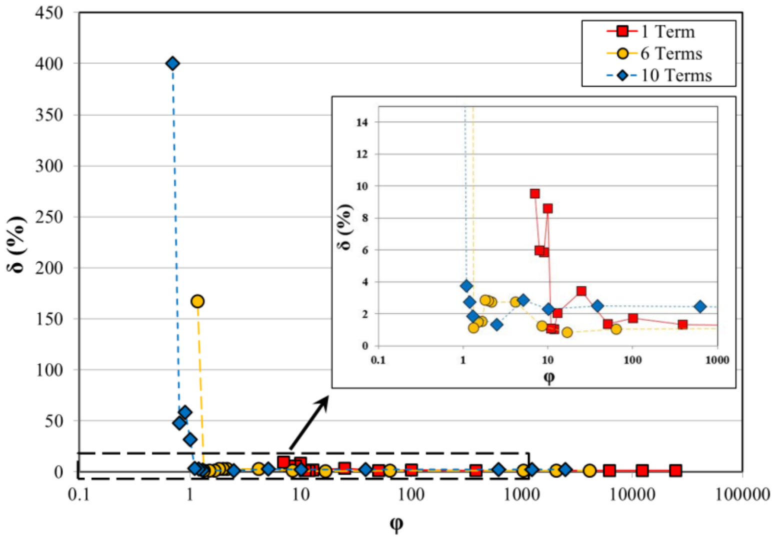


Figure 18. Effect of reducing data points in an AOI of 4 × 4 mm2 where λ = 25%. φ is defined as the number of data points used in the analysis divided by the number of terms in the series. Note the logarithmic scale in φ scale.

It can be seen the value of δ remains stable as long as φ > 15. Fig. 18 also shows that decreasing φ from 1.1 to 0.7 (or reducing the data points from 11 to 7) made a drastic increase in δ from 3.74% to 400% for calculations based on 10 terms. Very similar trends were also observed for other FOVs. This analysis suggests that in the optimum condition (λ = 25%, FOV > 4 × 4 mm2), reliable SIF estimations (δ < 4%) can be obtained as long as φ > 15.

## 4.2. SIF monitoring by DIC

In this part of the experiment, the displacement field ahead of a fatigue crack was monitored continuously by DIC method. Five terms in Williams' expansion were used to describe the crack tip field because no further improvement in the fitting of experimental to analytical displacement data observed by considering more than five terms.

In order to evaluate the ability of the proposed method to be used for in-service applications, continuous monitoring of the SIF is studied. It was observed that by increasing the applying load amplitude, the experimental ΔK always overestimates the nominal values ($\Delta K_{nom}$). The difference becomes more significant for higher loads. This behaviour can be attributed to the development of the plastically deformed zone at the crack tip. To compensate the effect of plasticity at the nominally evaluated SIF, Irwin's approach [86] was used. To this end, the crack tip was located at the centre of the plastic zone. In other words, the crack length was computed as the sum of crack length (a) with the half of the plastic zone ($r_y$):

$$a_{corr} = a + r_y \tag{16}$$

where

$$r_y = \frac{1}{2\pi}(\frac{K_I}{\sigma_{ys}})^2 \tag{17}$$

Accordingly, the nominal SIF was recalculated by replacing the crack length with the corrected crack length ($a_{corr}$) [87,88]. Fig. 19, shows how crack length correction can significantly improve the accuracy of the nominal SIF evaluation for higher loads, while it has a negligible effect at low ΔK. For example, for ΔK = 30 MPa√m the value of δ is reduced by 24.6%, 23.6% and 23.2% for AOIs of 10×10, 15×15 and 20×20 mm$^2$, respectively. The plasticity correction has reduced the value of δ at AOI = 20 × 20 mm$^2$ by 7.9%, 14.9% and 23.2% for applied ΔK of 20, 25 and 30 MPa√m, respectively. The higher value of δ at ΔK=10 MPa√m rather ΔK=15 MPa√m can be attributed to the poorer noise to signal ratio at lower applied loads.

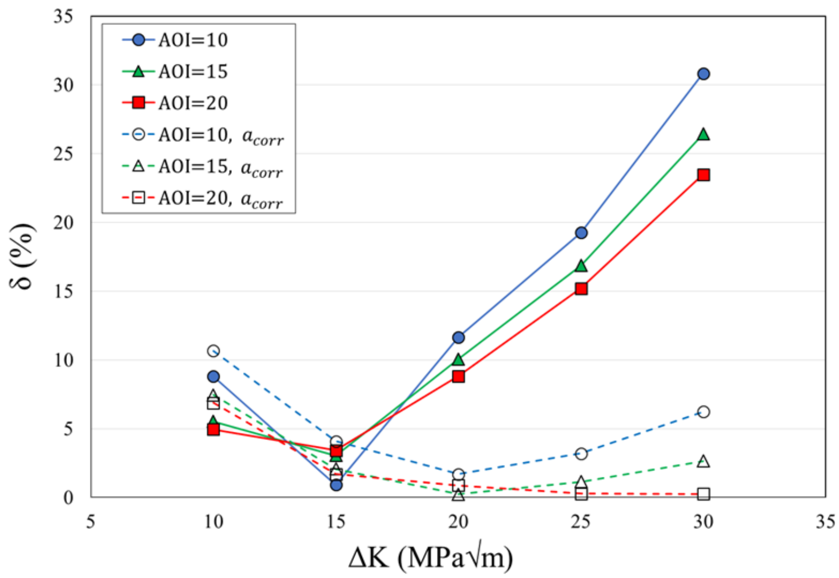


Figure 19. Evolution of δ by increasing $\Delta K_{nom}$ for different sizes of AOI in mm.

Fig. 20, shows the evolution of SIFs as a function of the applied load during the last loading segment, leading to the fracture of the sample. It can be observed that by increasing the load, the difference between the experimental and nominal SIF becomes more significant. The graph in Fig. 20 shows a very good fit between $\Delta K_{exp}$ and $\Delta K_{corr}$ up to the $\Delta K \approx 42$ MPa√m where there is a linear relation between SIF and load range ($\Delta P$). Thereafter, $\Delta K_{exp}$ surges upward while $\Delta K_{nom}$ keeps increasing linearly. Sudden fracture happened just after the last measurement point (top-right photograph in Fig. 20). Considering the load ratio of 0.3, at the deviation point, the $K_{max}$ is about 55 MPa√m ($\Delta K \approx 42$ MPa√m). It is interesting that this value is in good agreement with the estimated $K_c$ by Newman et al. [89] for a sample with similar geometry and thickness. This suggests that the point at which $\Delta K$ deviates from the linear behaviour can be used to estimate the critical SIF for this thickness. The higher value for measured critical SIF rather the fracture toughness of this material can be attributed to thinner thickness of the sample in comparison with standard sample for fracture toughness test [90].

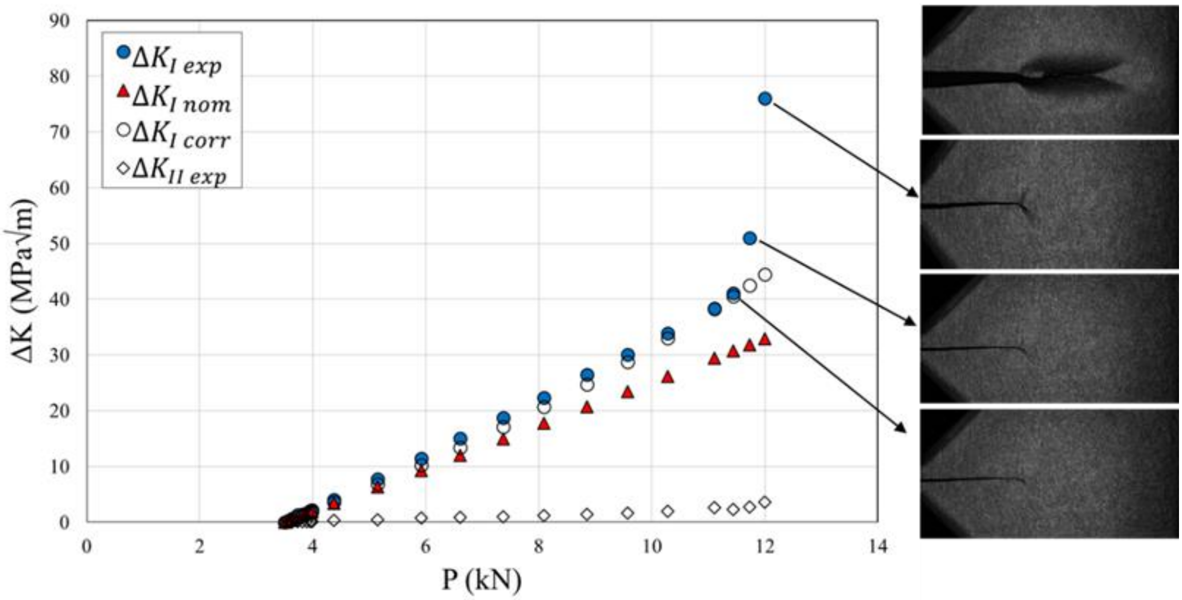


Figure 20. Continuous evaluation of ΔK as a function of applied load at the last loading segment, leading to sudden fracture of the sample.

## 4.3. Biaxial experiment

The capability of the proposed hybrid method for studying the crack state under complex loading condition was evaluated by studying a crack under tension-torsion cyclic loads which experienced an OL cycle.

The evolution of COD during a complete cycle (loading and unloading) at 60 μm behind the crack-tip for different crack lengths in all samples is shown in Fig. 21. For the specimens not subjected to OL, the maximum COD in a cycle increases steadily with the crack length (Figs. 21.a and c). There is a more drastic increment as the crack grows in the COD for high baseline load (Fig. 21.a) than for the low baseline load (Fig. 21.c), as one would expect.

The effect of applying an OL cycle on COD behaviour of samples can be seen in Fig. 21b and d. It can be seen that 40% OL in sample S2, produced a reduction in the maximum COD by the end of the test of 64% while 100 % OL cycle in fample S4 produced only 38% reduction in COD.

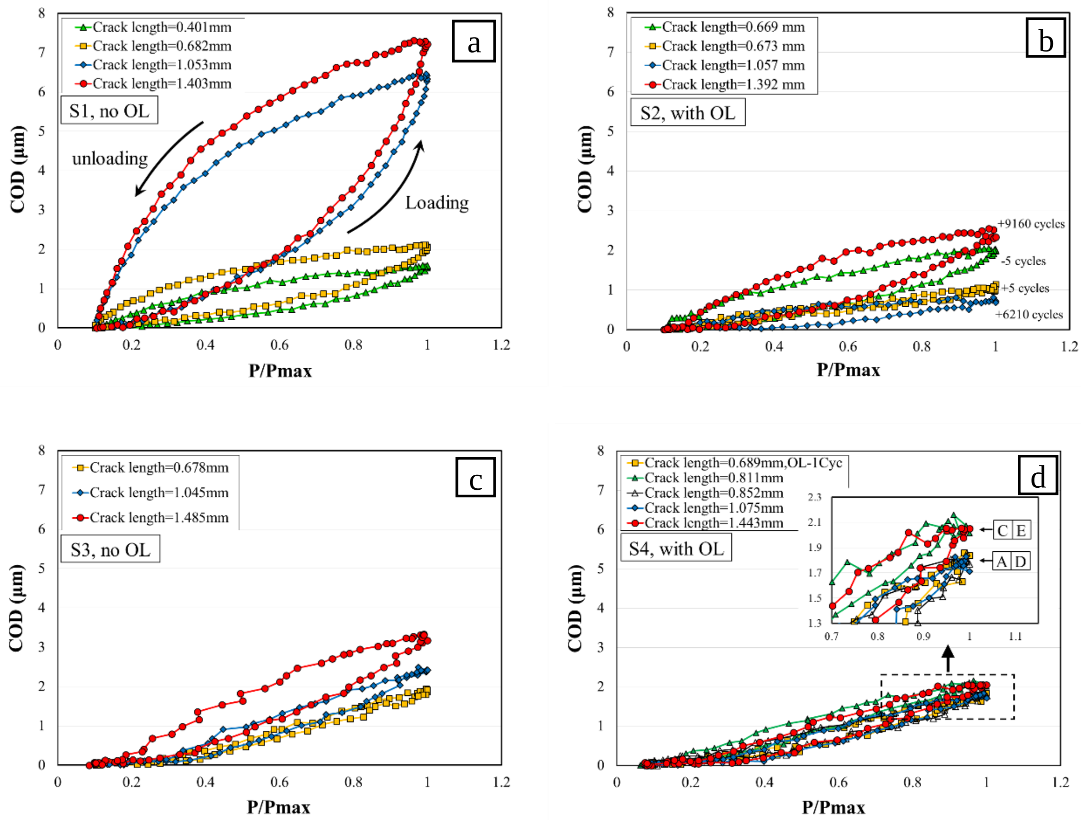


Figure 21. COD behaviour during loading and unloading cycle for different crack lengths of specimens. The number of cycles before and after OL where OL cycle was considered as 0 cycles, are shown in the graph b.

A summary of the opening load estimated following the procedure described in previous section is shown in Table 5. It can be seen that $P_{op}$ for S1 is 19% of the $P_{max}$, whereas $P_{op}$ for S2 sample, which has experienced an OL cycle, is 27% of the $P_{max}$. Regarding samples S3 and S4 which were tested under a lower baseline load, the OL cycle only increased $P_{op}$ slightly at the longest crack length. The $P_{op}$ increment induced by the OL is larger for low loads than for high loads (Table 5). This agrees well with the change that the OL produces in the growth rate (Fig. 14). The difference between the OL and the non-OL curves in crack growth rate is larger for low loads (Fig. 15.a) than for high loads (Fig. 15.b). Thus, crack growth rate data correlate satisfactorily with opening loads.

Table 5. Crack opening loads in a complete cycle.

| Sample | $P_{op}/P_{max}$ |
|---|---|
| S1 | 0.19 |
| S2 | 0.27 |
| S3 | 0.29 |
| S4 | 0.31 |

Table 6 shows the evaluated SIFs and corresponding $COD_{max}$ for two different crack lengths on each sample. It can be seen that $\Delta K_I$ and $\Delta K_{II}$ increase as the crack grows from 0.682 mm to 1.053 mm for sample S1 and from 0.675 mm to 1.045 mm for sample S3. Figs. 21.b and 21.d show that applying an OL reduces the COD values, as long as the crack is within the retardation stage. The small differences in the trend of $\Delta K_I$ and $\Delta K_{II}$ values are probably due to the crack changing its orientation through the experiment [78] as a consequence of crack-tip plasticity [91,92], loading direction and microstructure.

Table 6. Summary of the SIFs estimated for different samples and different crack lengths

| Specimen | Crack length (mm) | $COD_{max}$ (μm) | $\Delta K_I$ (MPa√m) | $\Delta K_{II}$ (MPa√m) |
|---|---|---|---|---|
| S1 | 0.682 | 2.1 | 13.2 | 24.5 |
| | 1.053 | 6.3 | 36.8 | 40.0 |
| S2 | 0.669 | 2.0 | 13.1 | 20.4 |
| | 1.057 | 0.7 | 15.6 | 25.3 |
| S3 | 0.678 | 1.9 | 11.8 | 0.2 |
| | 1.045 | 2.4 | 19.7 | 0.3 |
| S4 | 0.689 | 1.9 | 11.9 | 1.6 |
| | 1.075 | 1.8 | 14.0 | 3.7 |

# 5. Conclusions

In this work, the efficacy of a proposed hybrid method for evaluation of SIF was examined by performing different experiments. The proposed method is based on multi-parameter fracture mechanics where full-field experimental displacement data are captured. The experimental information is measured in the region surrounding the tip of a fatigue crack and then fitted to an analytical displacement field (Williams' series). Finally, the SIFs were estimated using a multipoint over deterministic method. In the first experiment, the effect of some experimental variables on $K_I$ estimation using DIC was examined based on an elastic mode I. It was shown that the accuracy of $K_I$ can be affected not only by the well-known variables such as subset size in DIC and considered number of Williams' series but also by the size and position of AOI. Experimental results indicate the significant effect of the position of the AOI for accurate estimation of SIF with DIC technique. It was shown that including a part of the crack length inside the AOI (crack extending to one-fourth of the AOI) provides the best estimations for all FOVs. Finally, it was also shown that reliable estimations of the $K_I$ can be achieved as long as the number of displacement vectors fitted to the model is 15 times larger than the number of terms in the series.

In a similar manner, the evolution of SIF was monitored by DIC method in a separate experiment. The results showed that the Irwin's approach that modifies the crack length to account for crack tip plasticity improves noticeably the SIF estimations. Continuous measurement of the SIF at the final loading stage to fracture of the sample showed a deviation from the linear relation between the load and the experimental SIF. Based on a previous work, this deviation might be related to the critical SIF for the thickness studied. Since either the experimental method or corrected theoretical method are based on LEFM, the validity of the results in this range should be assessed with a parameter like J-integral. Nevertheless, further research is currently in progress to better understand the physics behind such deviation.

The capability of the proposed method for capturing the SIF of a crack under more complex loading condition was also assessed. In addition, the effect of applying OL cycle on the behaviour of a crack under cyclic biaxial loading is studied with DIC technique. It is observed that applying 100% OL on a sample under low cyclic loads, delayed the appearance of the retardation stage. COD examinations shows the classical sequences of OL, including acceleration and retardation. The hybrid method was also used for studying the biaxial fatigue cracks. This allowed the mixed-mode SIF ($\Delta K_I$ and $\Delta K_{II}$) to be estimated on samples under different load levels, with and without applying OL. Results showed that a slower increment in $\Delta K_I$ as the crack grows for the OL case, compared to the non-OL case.

The results of three experiments proved the reliability and capability of the hybrid method for evaluation of SIFs not only for simple uniaxial conditions, but also for more complex biaxial loading conditions. The suggested recommendations for selecting the experimental DIC parameters can be used by researchers and engineers for improving the accuracy and stability of SIF measurement using DIC technique. The SIF monitoring experiment showed the capability of the method for in-service application, when evolution of the SIF needs to be measured continuously.

# References

[1] T.L. Anderson, Fracture Mechanics, Fundamentals and Applications, 4th ed., CRC Press, Boca Raton, FL, USA., 2017.

[2] S. Suresh, Fatigue of Materials, 2nd ed., Cambridge University Press, New York, 1998.

[3] K. Ramesh, S. Gupta, A.A. Kelkar, Evaluation of stress field parameters in fracture mechanics by photoelasticity - revisited, Eng. Fract. Mech. 56 (1997) 25-41 and 43-45.

[4] F.A. Díaz, J.R. Yates, E.A. Patterson, Some improvements in the analysis of fatigue cracks using thermoelasticity, Int. J. Fatigue. 26 (2004) 365–376. doi:10.1016/j.ijfatigue.2003.08.018.

[5] D. Nowell, R.J.H. Paynter, P.F.P. De Matos, Optical methods for measurement of fatigue crack closure: moiré interferometry and digital image correlation, Fatigue Fract. Eng. Mater. Struct. 33 (2010) 778–790. doi:10.1111/j.1460-2695.2010.01447.x.

[6] S.R. McNeill, W.H. Peters, M.A. Sutton, Estimation of stress intensity factor by digital image correlation, Eng. Fract. Mech. 28 (1987) 101–112. doi:10.1016/0013-7944(87)90124-X.

[7] J. Smith, M.N. Bassim, C.D. Liu, T.M. Holden, Mesurement of crack tip strains using neutron difraction, Eng. Fract. Mech. 52 (1995) 843–851.

[8] P. Lopez-Crespo, P.J. Withers, F. Yusof, H. Dai, a. Steuwer, J.F. Kelleher, T. Buslaps, Overload effects on fatigue crack-tip fields under plane stress conditions: surface and bulk analysis, Fatigue Fract. Eng. Mater. Struct. 36 (2013) 75–84. doi:10.1111/j.1460-2695.2012.01670.x.

[9] S. Yoneyama, A. Kitagawa, S. Iwata, K. Tani, H. Kikuta, Bridge deflection measurement using digital image correlation, Exp. Tech. 31 (2007) 34–40. doi:10.1111/j.1747-1567.2007.00132.x.

[10] M.A. Sutton, N. Li, D.C. Joy, A.P. Reynolds, X. Li, Scanning electron microscopy for quantitative small and large deformation measurements Part I: SEM imaging at magnifications from 200 to 10,000, Exp. Mech. 47 (2007) 775–787. doi:10.1007/s11340-007-9042-z.

[11] J.D. Carroll, W. Abuzaid, J. Lambros, H. Sehitoglu, High resolution digital image

correlation measurements of strain accumulation in fatigue crack growth, Int. J. Fatigue. 57 (2013) 140–150. doi:10.1016/j.ijfatigue.2012.06.010.

[12] R. Stephens, A. Fatemi, R.R. Stephens, H. Fuchs, Metal Fatigue in Engineering, 2nd ed., John Wily & Sons, Inc, New York, 2001.

[13] ASTM E1823-13 Standard Terminology Relating to Fatigue and Fracture Testing, West Conshohocken, PA, 2013. doi:10.1520/E1823-13.2.

[14] G.R. Irwin, Analysis of stresses and strains near the end of a crack traversing a plate, J. Appl. Mech. ASME. E24 (1957) 351–369.

[15] P.P. Paris, F.F. Erdogan, A critical analysis of crack propagation laws, ASME. J. Basic Eng. 85 (1963) 528–533. doi:doi:10.1115/1.3656900.

[16] M.A. Sutton, J.-J. Orteu, H.W. Schreier, Image Correlation for Shape, Motion and Deformation Measurements, Springer US, New York, 2009. doi:10.1007/978-0-387-78747-3.

[17] P.F.P. de Matos, D. Nowell, Numerical simulation of plasticity-induced fatigue crack closure with emphasis on the crack growth scheme: 2D and 3D analyses, Eng. Fract. Mech. 75 (2008) 2087–2114. doi:10.1016/j.engfracmech.2007.10.017.

[18] H.M. Westergaard, Bearing pressures and cracks, J. Appl. Mech. 61 (1939) A49–A53.

[19] M.L. Williams, On the stress distribution at the base of a stationary crack, J. Appl. Mech. 24 (1957) 109–114. doi:10.1115/1.3640470.

[20] B.S.G. Larsson, A.J. Carlsson, Influence of non-singular stress terms and specimen geometry on small-scale yielding at crack tips in elastic-plastic materials, J. Mech. Phys. Solids. 21 (1973) 263–277.

[21] J.R. Yates, M. Zanganeh, Y.H. Tai, Quantifying crack tip displacement fields with DIC, Eng. Fract. Mech. 77 (2010) 2063–2076. doi:10.1016/j.engfracmech.2010.03.025.

[22] C.J. Christopher, M.N. James, E.A. Patterson, K.F. Tee, Towards a new model of crack tip stress fields, Int J Fract. 148 (2007) 361–371. doi:10.1007/s10704-008-9209-3.

[23] P. Lopez-Crespo, D. Camas, F.V. Antunes, J.R. Yates, A study of the evolution of crack tip plasticity along a crack front, Theor. Appl. Fract. Mech. 98 (2018) 59–66. doi:10.1016/J.TAFMEC.2018.09.012.

[24] R.O. Ritchie, Mechanisms of fatigue crack propagation in metals, ceramics and

composites: Role of crack tip shielding, Mater. Sci. Eng. A. 103 (1988) 15–28. doi:10.1016/0025-5416(88)90547-2.

[25] M.A. Sutton, W. Zhao, S.R. McNeill, J.D. Helm, R.S. Piascik, W.T. Riddell, Local crack closure measurements: development of a measurement system using computer vision and a far-field microscope, in: R.C. McClung, J.C. Newman (Eds.), Adv. Fatigue Crack Clos. Meas. Anal. Second Vol. ASTM STP 1343, American Society for Testing and Materials, West Conshohocken,PA, 1999: pp. 145–156.

[26] C.A. Simpson, S. Kozuki, P. Lopez-Crespo, M. Mostafavi, T. Connolley, P.J. Withers, Quantifying fatigue overload retardation mechanisms by energy dispersive X-ray diffraction, J. Mech. Phys. Solids. 124 (2018) 392–410. doi:10.1016/j.jmps.2018.10.020.

[27] A.S. Chernyatin, P. Lopez-Crespo, B. Moreno, Y.G. Matvienko, Multi-approach study of crack-tip mechanics on aluminium 2024 alloy, Theor. Appl. Fract. Mech. 98 (2018) 38–47. doi:10.1016/J.TAFMEC.2018.09.007.

[28] S. Stoychev, D. Kujawski, Methods for crack opening load and crack tip shielding determination: A review, Fatigue Fract. Eng. Mater. Struct. 26 (2003) 1053–1067. doi:10.1046/j.1460-2695.2003.00691.x.

[29] M.A. Sutton, W.J. Wolters, W.H. Peters, W.F. Ranson, S.R. McNeill, Determination of displacements using an improved digital correlation method, Image Vis. Comput. 1 (1983) 133–139. doi:10.1016/0262-8856(83)90064-1.

[30] M.R. Ayatollahi, H. Safari, Evaluation of crack tip constraint using photoelasticity, Int. J. Press. Vessel. Pip. 80 (2003) 665–670. doi:10.1016/S0308-0161(03)00076-0.

[31] S. Yoneyama, T. Ogawa, Y. Kobayashi, Evaluating mixed-mode stress intensity factors from full-field displacement fields obtained by optical methods, Eng. Fract. Mech. 74 (2007) 1399–1412. doi:10.1016/j.engfracmech.2006.08.004.

[32] B. Pan, K. Qian, H. Xie, A. Asundi, Two-dimensional digital image correlation for in-plane displacement and strain measurement: a review, Meas. Sci. Technol. 20 (2009) 062001 (17pp). doi:10.1088/0957-0233/20/6/062001.

[33] J.R. Taylor, An introduction to error analysis: the study of uncertainties in physical measurements, 2nd ed., California, 1982. doi:10.1119/1.13309.

[34] H.W. Schreier, J.R. Braasch, M.A. Sutton, Systematic errors in digital image correlation

caused by intensity interpolation, Opt. Eng. 39 (2000) 2915–2921.

[35] H.W. Schreier, M.A. Sutton, Systematic errors in digital image correlation due to undermatched subset shape functions, Exp. Mech. 42 (2002) 303–310. doi:10.1177/001448502321548391.

[36] L. Yu, B. Pan, The errors in digital image correlation due to overmatched shape functions, Meas. Sci. Technol. 26 (2015) 045202. doi:10.1088/0957-0233/26/4/045202.

[37] M. Fazzini, S. Mistou, O. Dalverny, L. Robert, Study of image characteristics on digital image correlation error assessment, Opt. Lasers Eng. 48 (2010) 335–339. doi:10.1016/j.optlaseng.2009.10.012.

[38] B. Pan, Reliability-guided digital image correlation for image deformation measurement, Appl. Opt. 48 (2009) 1535–1542. doi:10.1364/AO.48.001535.

[39] J.M. Vasco-Olmo, F.A. Díaz, E.A. Patterson, Experimental evaluation of shielding effect on growing fatigue cracks under overloads using ESPI, Int. J. Fatigue. 83 (2016) 117–126. doi:10.1016/j.ijfatigue.2015.10.003.

[40] F. Berto, P. Lazzarin, On higher order terms in the crack tip stress field, Int. J. Fract. 161 (2010) 221–226. doi:10.1007/s10704-010-9443-3.

[41] F. Berto, P. Lazzarin, Multiparametric full-field representations of the in-plane stress fields ahead of cracked components under mixed mode loading, Int. J. Fatigue. 46 (2013) 16–26. doi:10.1016/j.ijfatigue.2011.12.004.

[42] M.Y. Dehnavi, S. Khaleghian, A. Emami, M. Tehrani, N. Soltani, Utilizing digital image correlation to determine stress intensity factors, Polym. Test. 37 (2014) 28–35. doi:10.1016/j.polymertesting.2014.04.005.

[43] W.H. Peters, W.F. Ranson, J.F. Kalthoff, S.R. Winkler, A study of dynamic near-crack-tip fracture parameters by digital image analysis, J. Phys. Colloq. 46 (1985) C5-631-C5-638. doi:10.1051/jphyscol:1985581.

[44] R. Hamam, F. Hild, S. Roux, Stress intensity factor gauging by digital image correlation: Application in cyclic fatigue, Strain. 43 (2007) 181–192. doi:10.1111/j.1475-1305.2007.00345.x.

[45] S. Roux, J. Réthoré, F. Hild, Recent progress in digital image correlation: from measurement to mechanical identification, J. Phys. Conf. Ser. 135 (2008) 012002.

doi:10.1088/1742-6596/135/1/012002.

[46] F. Yusof, P.J. Withers, Real-time acquisition of fatigue crack images for monitoring crack-tip stress intensity variations within fatigue cycles, J. Strain Anal. Eng. Des. 44 (2008) 149–158. doi:10.1243/03093247JSA440.

[47] P. Lopez-Crespo, A. Shterenlikht, J.R. Yates, E.A. Patterson, P.J. Withers, Some experimental observations on crack closure and crack-tip plasticity, Fatigue Fract. Eng. Mater. Struct. 32 (2009) 418–429. doi:10.1111/j.1460-2695.2009.01345.x.

[48] D. Wagner, N. Ranc, C. Bathias, P.C. Paris, Fatigue crack initiation detection by an infrared thermography method, Fatigue Fract. Eng. Mater. Struct. 33 (2009) 12–21. doi:10.1111/j.1460-2695.2009.01410.x.

[49] A. Maslouhi, Fatigue crack growth monitoring in aluminum using acoustic emission and acousto-ultrasonic methods, Struct. Control Heal. Monit. 18 (2011) 790–806. doi:10.1002/stc.478.

[50] V. Zilberstein, D. Grundy, V. Weiss, N. Goldfine, E. Abramovici, J. Newman, T. Yentzer, Early detection and monitoring of fatigue in high strength steels with MWM-Arrays, Int. J. Fatigue. 27 (2005) 1644–1652. doi:10.1016/j.ijfatigue.2005.07.028.

[51] R. Hamia, C. Cordier, C. Dolabdjian, Eddy-current non-destructive testing system for the determination of crack orientation, NDT&E Int. 61 (2014) 24–28. doi:10.1016/j.ndteint.2013.09.005.

[52] H. Nakazawa, K. Hirano, Ultrasonic monitoring techniques of crack growth and fracture mechanics evaluation of materials, Jpn. J. Appl. Phys. 23 (1984) 12–16.

[53] ASTM E1685-13, Standard practice for measuring the change in length of fasteners using the ultrasonic pulse-echo technique, in: ASTM International, West Conshohocken, PA, 2013. doi:https://doi.org/10.1520/E1685.

[54] J. Cuadra, P.A. Vanniamparambil, K. Hazeli, I. Bartoli, A. Kontsos, A hybrid optico-acoustic NDE approach for deformation and damage monitoring, in: J. Kag, D. Jablonski, D. Dudzinski (Eds.), Eval. Exist. New Sens. Technol. Fatigue, Fract. Mech. Testing, STP 1584, ASTM International, West Conshohocken,PA, 2015: pp. 135–146. doi:10.1520/STP158420140051.

[55] V.N. Whittaker, A review of non-destructive measurement of flaw size, Non-Destructive Test. 5 (1972) 92–100. doi:10.1016/0029-1021(72)90101-6.

[56] P. Gao, C. Wang, Y. Li, Z. Cong, Electromagnetic and eddy current NDT in weld inspection: A review, Insight Non-Destructive Test. Cond. Monit. 43 (2015) 337–345. doi:10.1784/insi.2015.57.6.337.

[57] C.B. Scruby, An introduction to acoustic emission, J. Phys. E. 20 (1987) 946–953. doi:10.1088/0022-3735/20/8/001.

[58] Y. Du, F. Díaz, R. Burguete, E.A. Patterson, Evaluation using digital image correlation of stress intensity factors in an aerospace panel, Exp. Mech. 51 (2011) 45–57. doi:10.1007/s11340-010-9335-5.

[59] P. Lopez-Crespo, A. Shterenlikht, E.A. Patterson, J.R. Yates, P.J. Withers, The stress intensity of mixed mode cracks determined by digital image correlation, J. Strain Anal. Eng. Des. 43 (2008) 769–780. doi:10.1243/03093247JSA419.

[60] M. Zanganeh, P. Lopez-Crespo, Y.H. Tai, J.R. Yates, Locating the crack tip using displacement field data: a comparative study, Strain. 49 (2013) 102–115. doi:10.1111/str.12017.

[61] S. Yoneyama, S. Arikawa, S. Kusayanagi, K. Hazumi, Evaluating J-integral from displacement fields measured by digital image correlation, Strain. 50 (2014) 147–160. doi:10.1111/str.12074.

[62] P.F.P. de Matos, D. Nowell, Experimental and numerical investigation of thickness effects in plasticity-induced fatigue crack closure, Int. J. Fatigue. 31 (2009) 1795–1804. doi:10.1016/j.ijfatigue.2008.12.003.

[63] D. Camas, P. Lopez-Crespo, A. Gonzalez-Herrera, B. Moreno, Numerical and experimental study of the plastic zone in cracked specimens, Eng. Fract. Mech. (2017). doi:10.1016/j.engfracmech.2017.02.016.

[64] F. V. Díaz, G.H. Kaufmann, A.F. Armas, G.E. Galizzi, Optical measurement of the plastic zone size in a notched metal specimen subjected to low-cycle fatigue, Opt. Lasers Eng. 35 (2001) 325–333. doi:10.1016/S0143-8166(01)00030-6.

[65] J.M. Vasco-Olmo, M.N. James, C.J. Christopher, E.A. Patterson, F.A. Díaz, Assessment of crack tip plastic zone size and shape and its influence on crack tip shielding, Fatigue Fract. Eng. Mater. Struct. 39 (2016) 969–981. doi:10.1111/ffe.12436.

[66] M. Mokhtarishirazabad, P. Lopez-Crespo, M. Zanganeh, Stress intensity factor monitoring under cyclic loading by digital image correlation, Fatigue Fract. Eng. Mater.

Struct. (2018). doi:10.1111/ffe.12825.

[67] R.J. Sanford, J.W. Dally, A general method for determining mixed-mode stress intensity factors from isochromatic fringe patterns, Eng. Fract. Mech. 11 (1979) 621–633. doi:10.1016/0013-7944(79)90123-1.

[68] J. Réthoré, a. Gravouil, F. Morestin, a. Combescure, Estimation of mixed-mode stress intensity factors using digital image correlation and an interaction integral, Int. J. Fract. 132 (2005) 65–79. doi:10.1007/s10704-004-8141-4.

[69] P. López-Crespo, R.L. Burguete, E.A. Patterson, A. Shterenlikht, P.J. Withers, J.R. Yates, Study of a crack at a fastener hole by digital image correlation, Exp. Mech. 49 (2009) 551–559. doi:10.1007/s11340-008-9161-1.

[70] M. Sander, H. Richard, Experimental and numerical investigations on the influence of the loading direction on the fatigue crack growth, Int. J. Fatigue. 28 (2006) 583–591. doi:10.1016/j.ijfatigue.2005.05.012.

[71] P. Lopez-Crespo, M. Mostafavi, A. Steuwer, J.F. Kelleher, T. Buslaps, P.J. Withers, Characterisation of overloads in fatigue by 2D strain mapping at the surface and in the bulk, Fatigue Fract. Eng. Mater. Struct. 39 (2016) 1040–1048. doi:10.1111/ffe.12463.

[72] M. Mokhtarishirazabad, P. Lopez-Crespo, B. Moreno, A. Lopez-Moreno, M. Zanganeh, Optical and analytical investigation of overloads in biaxial fatigue cracks, Int. J. Fatigue. 100 (2017) 583–590. doi:10.1016/j.ijfatigue.2016.12.035.

[73] ASTM E647-15e1 Standard Test Method for Measurement of Fatigue Crack Growth Rates, ASTM International, West Conshohocken, PA, 2015. doi:10.1520/E0647-15E01.2.

[74] Vic-2D software. Correlated Solutions Incorporated (C.S.Inc) <http://www.correlatedsolutions.com>, (n.d.).

[75] S. Seitl, L. Malíková, V. Růžička, B. Moreno, P. Lopez-Crespo, Williams' expansion-based approximation of the displacement field in an Al 2024 compact tension specimen reconstructed from optical measurements, Fatigue Fract. Eng. Mater. Struct. 41 (2018) 2187–2196. doi:10.1111/ffe.12842.

[76] Y. Murakami, Stress Intensity Factors Handbook, Oxford: Pergamon Press, 1987.

[77] S. Beretta, S. Rabbolini, A.D. Bello, Multi-scale crack closure measurement with digital

image correlation on Haynes 230, Frat. Ed Integrità Strutt. 33 (2015) 174–182. doi:10.3221/IGF-ESIS.33.22.

[78] P. Lopez-Crespo, B. Moreno, A. Lopez-Moreno, J. Zapatero, Study of crack orientation and fatigue life prediction in biaxial fatigue with critical plane models, Eng. Fract. Mech. 136 (2015) 115–130. doi:10.1016/j.engfracmech.2015.01.020.

[79] P. Lopez-Crespo, A. Garcia-Gonzalez, B. Moreno, A. Lopez-Moreno, J. Zapatero, Some observations on short fatigue cracks under biaxial fatigue, Theor. Appl. Fract. Mech. 80 (2015) 96–103. doi:10.1016/j.tafmec.2015.05.004.

[80] P. Lopez-Crespo, B. Moreno, A. Lopez-Moreno, J. Zapatero, Characterisation of crack-tip fields in biaxial fatigue based on high-magnification image correlation and electro-spray technique, Int. J. Fatigue. 71 (2015) 17–25. doi:10.1016/j.ijfatigue.2014.02.016.

[81] F. Yusof, P. Lopez-Crespo, P.J. Withers, Effect of overload on crack closure in thick and thin specimens via digital image correlation, Int. J. Fatigue. 56 (2013) 17–24. doi:10.1016/j.ijfatigue.2013.07.002.

[82] M. Mokhtarishirazabad, P. Lopez-Crespo, B. Moreno, A. Lopez-Moreno, M. Zanganeh, Evaluation of crack-tip fields from DIC data: A parametric study, Int. J. Fatigue. 89 (2016) 11–19. doi:10.1016/j.ijfatigue.2016.03.006.

[83] M. Skorupa, S. Beretta, M. Carboni, T. Machniewicz, An algorithm for evaluating crack closure from local compliance measurements, Fatigue Fract. Eng. Mater. Struct. 25 (2002) 261–273. doi:10.1046/j.1460-2695.2002.00444.x.

[84] J.M. Vasco-Olmo, F.A. Díaz, Experimental evaluation of the effect of overloads on fatigue crack growth by analysing crack tip displacement fields, Eng. Fract. Mech. 166 (2016) 82–96. doi:10.1016/j.engfracmech.2016.08.026.

[85] H.L. Ewalds, R.J.H. Wanhill, Fracture Mechanics, Arnold, London, 1984.

[86] G.R. Irwin, Plastic zone near a crack and fracture toughness, in: Sagamore Ordnance Mater. Conf., Syracuse University, 1961.

[87] R.H. Heyer, D.E. McCabe, Crack growth resistance in plane-stress fracture testing, Eng. Fract. Mech. 4 (1972) 413–430. doi:10.1016/0013-7944(72)90054-9.

[88] G.R. Irwin, Linear fracture mechanics, fracture transition, and fracture control, Eng. Fract. Mech. 1 (1968) 241–257. doi:10.1016/0013-7944(68)90001-5.

[89] J.C. Newman, Jr., An evaluation of fracture analysis methods, in: J.C. Newman, Jr., F.J. Loss (Eds.), ASTM STP 896, American Society for Testing and Materials, Philadelphia, 1985: pp. 5–96.

[90] ASTM E1820-18 Standard Test Method for Measurement of Fracture Toughness, West Conshohocken, PA, 2018. doi:10.1520/E1820-15A.

[91] P. Lopez-Crespo, S. Pommier, Numerical Analysis of Crack Tip Plasticity and History Effects under Mixed Mode Conditions, J. Solid Mech. Mater. Eng. 2 (2008) 1567–1576. doi:10.1299/jmmp.2.1567.

[92] S. Pommier, P. Lopez-Crespo, P.Y. Decreuse, A multi-scale approach to condense the cyclic elastic-plastic behaviour of the crack tip region into an extended constitutive model, Fatigue Fract. Eng. Mater. Struct. 32 (2009) 899–915. doi:10.1111/j.1460-2695.2009.01392.x.

# Appendix I:

Published Paper #1

**Title:** Evaluation of crack-tip fields from DIC data: A parametric study

**Authors:** M. Mokhtarishirazabad[1], P. Lopez-Crespo[1], B. Moreno[1], A. Lopez-Moreno[2], M. Zanganeh[3]

[1]Department of Civil and Materials Engineering, University of Malaga, C/Dr Ortiz Ramos s/n, 29071, Malaga, Spain

[2]Department of Materials Science and Metallurgy Engineering, University of Jaen, Campus Las Lagunillas, 23071, Jaen, Spain

[3]Jacobs Technology, NASA Johnson Space Center, Houston TX, USA

**Journal:** International Journal of Fatigue, Volume 89, August 2016, Pages 11-19

Impact Factor: 3.132 , Q1 in JCR

International Journal of Fatigue 89 (2016) 11–19

Contents lists available at ScienceDirect

International Journal of Fatigue

journal homepage: www.elsevier.com/locate/ijfatigue

# Evaluation of crack-tip fields from DIC data: A parametric study

M. Mokhtarishirazabad [a], P. Lopez-Crespo [a,*], B. Moreno [a], A. Lopez-Moreno [b], M. Zanganeh [c]

[a] Department of Civil and Materials Engineering, University of Malaga, C/Dr Ortiz Ramos s/n, 29071 Malaga, Spain
[b] Department of Materials Science and Metallurgy Engineering, University of Jaen, Campus Las Lagunillas, 23071 Jaen, Spain
[c] Jacobs Technology, NASA Johnson Space Center, Houston, TX, USA

ARTICLE INFO

*Article history:*
Received 17 November 2015
Received in revised form 27 February 2016
Accepted 1 March 2016
Available online 7 March 2016

*Keywords:*
Linear elastic fracture mechanics
Digital image correlation
Stress intensity factor
K-dominance
Crack-tip displacement field

ABSTRACT

In the past two decades, crack-tip mechanics has been studied increasingly using full-field techniques. Within these techniques, Digital Image Correlation (DIC) has been most widely used due to its many advantages, to extract important crack-tip information, including Stress Intensity Factor (SIF), crack opening displacement, J-integral, T-stress, closure level, plastic zone size, etc. However, little information is given in the literature about the experimental setup that provides best estimations for the different parameters. The current work aims at understanding how the experimental conditions used in DIC influence the crack-tip information extracted experimentally. The influence of parameters such as magnification factor, the position of the images with respect the crack-tip and size of the subset used in the correlation is studied. The influence is studied in terms of SIF by using Williams' model. In this regard, cyclic loading on a fatigue crack in a compact tension (CT) specimen, made of aluminium 2024-T351 alloy, has been applied and the surface deformation around the crack-tip has been examined. The comparison between nominal and experimental values of $K_I$ showed that the effect of subset size on the measured $K_I$ is negligible compared to the effect of the field of view and the position of the area of interest.


## 1. Introduction

In recent years, there has been a steady increase in the use of full-field techniques to study crack-tip mechanics. Within these techniques, Digital Image Correlation (DIC) has been most widely used due to its many advantages, to extract important crack-tip information, including Stress Intensity Factor (SIF) [1], Crack Opening Displacement (COD) [2], J-integral [3,4], T-stress [5–7], closure level [8–10], plastic zone size [11,12], etc. Due to its industrial relevance, a great effort has been put into improving and refining the methodology to extract the SIF from full-field DIC data [1,6,13–17]. Experimentally, DIC measurement accuracy can be affected by several factors, such as subpixel optimization algorithm, subset size and image quality [18]. It is evident that the more accurate displacement data, the more reliable estimation of SIFs. While the random error in any measurement is the inherent part of each measurement, systematic error is predictable and is typically constant and proportional to the true value [19]. Systematic errors in DIC as a result of intensity interpolation, overmatched and under-matched subset shape function has been explored by Schreier et al. [20,21] and Yu and Pan [22]. A thorough study on the errors caused by different bit depths of the image, image saturation in respect with subset size, speckle pattern and subset shape function on synthetic images has been conducted by Fazzini et al. [23]. It was shown that decreasing the encoding of the images and overexpose of the speckle deteriorate the measurements by a factor of 2 and 10 respectively. Pan [24] proposed a reliability-guided DIC method which is applicable to images with shadows, discontinuous areas, and deformation discontinuities.

Crack-tip field information (stress, strain, displacement) can be expressed in a series form [1]. Multi-point over-deterministic method [25] allows one to estimate the SIF by fitting analytical solutions such as Westergard's [26] Williams' [27], Muskhilishvili's [28] or Christopher, James and Patterson (CJP) model [29] series to the experimental data. This methodology has developed over the years since the first attempt in 1980's [1,5,15,16]. Early works that used DIC to estimate the SIF used the least square error analysis to estimate $K_I$ for the dynamically impacted three-point specimen made from Araldite B [30]. Displacement data were adapted from an area of 8 $mm^2$, including crack-tip and region near the opening crack surface. Higher order terms were included in their estimation until reach to the convergence value of $K_I$. Utilising an over-deterministic least square method for evaluating mixed mode stress field parameters by the technique of photoelasticity, Ramesh et al. [31] showed the importance of using multi-parameter stress

* Corresponding author.
*E-mail address:* plopezcrespo@uma.es (P. Lopez-Crespo).

http://dx.doi.org/10.1016/j.ijfatigue.2016.03.006
0142-1123/

**Nomenclature**

| | | | |
|---|---|---|---|
| $a$ | crack length | $r$ | radial distance from the crack-tip |
| $a_0$, $b_0$ | rigid body translation | $R_0$ | rigid body rotation |
| $a_{in}$ | length of a part of the crack inside the area of interest | $R$ | load ratio (=$P_{min}/P_{max}$) |
| $a_n$, $b_n$ | coefficients in Williams' expansion | $T$ | T-stress, a constant stress parallel to the crack |
| AOI | area of interest using for analysing data points inside a particular region inside the field of view | $u$, $v$ | horizontal and vertical displacement fields |
| COD | crack opening displacement | $\delta$ | error function (see Eq. (6)) |
| DIC | digital image correlation | $\varphi$ | degree of over-determination in the multi-point over-deterministic method (see by Eq. (9)) |
| FOV | field of view | $\lambda$ | the position of the crack-tip within the AOI (see Eq. (7)) |
| $K_I$ | stress intensity factor in mode I | $\theta$ | phase distance from the crack-tip |
| $K_{I\ exp}$ | experimental stress intensity factor evaluated by Williams' solution (see Eq. (1)) | $\kappa$ | $\kappa = (3-v)/(1+v)$ for plan stress and $\kappa = 3-4v$ for plan strain condition |
| $K_{I\ nom}$ | nominal stress intensity factor in mode I | $\mu$ | shear modulus |
| $L$ | longitude length of the area of interest | $v$ | Poisson's ratio |
| $P_{max}$, $P_{min}$ | maximum and minimum applied load in the fatigue test | $\sigma_y$ | yield strength |

equations for solving real life problems where displacement data are collecting from a large area. They used the fringe order minimisation error as their convergence criteria. The method was tested in three different geometries and for those data, a minimum of 6 parameters were required to obtain a convergence error less than 0.1 in fringe order (N) in modes I and II. The effect of adding up to 48 higher order terms for estimating the SIF was also studied on a 3-point bend specimen made of plexiglass with the field of view (FOV) of 12.7 × 12.7 mm$^2$ [1]. Using least square fitting, the authors reported an error of less than 10% in their estimation of $K_I$ and also no significant improvement by considering higher order terms. This seems to be true for small FOV. Yoneyama et al. [32] suggested determining SIF by adopting the convergent values (considering more than 7 terms). A nonlinear least square method was used for estimating SIF from displacement data provided by DIC from a FOV of 6 × 5 mm$^2$. Vasco-Olmo et al. [9] evaluated the fatigue crack shielding by analysing displacement field data obtained by 2D DIC and utilising four different models. They reported that the CJP model showed an extraordinary potential for the evaluation of the crack-tip shielding during fatigue crack growth. A finite element analysis of the stress field ahead of a cracked plate has been conducted by Berto and Lazzarin [33,34]. They were able to obtain good estimations of the stress field in a very small area ahead of the crack-tip ($r$ = 0.01 mm) by using $K_I$, $K_{II}$ and T-stress in Williams' solution. In addition, they were also able to describe the stress field in larger areas by considering the first 7 terms in the series. Dehnavi et al. [35] estimated the SIF of a polycarbonate plate by DIC method (subset of 21 × 21 pixels) considering 4 terms of Williams' series taking a similar approach to Berto and Lazzarin.

The differences between all works above mentioned suggest that there exists a number of parameters that can influence the SIF estimations. These include the magnification factor, the FOV, the subset size, the dimensions of the area of interest (AOI), the portion of crack included in the AOI, the masking of the crack-tip plastic zone and the number of terms considered in the analytical solution. Table 1 summarises the parameters that have been used in some of the most relevant works that estimated SIF from DIC.

Table 1 shows a clear discrepancy in the parameter selection for different works. Authors provided little or no justification for employing different parameters than previous published works. Therefore, the main objective of the current work is to study in a structured way, the influence of the different parameters involved in estimating the SIF with DIC technique.

## 2. Materials and methods

Experiments were conducted on a CT specimen which was extracted and machined in $T$–$L$ direction (crack propagation along rolling direction) from a 2024-T351 aluminium alloy plate according to ASTM E-647 [39]. Fig. 1 illustrates the specimen geometry and dimensions. The mechanical properties of the material are summarised in Table 2. The sample surface was scratched with abrasive SiC sand papers grades 240, 380 and 800 to obtain a random grey intensity distribution required for DIC technique. Good results have been obtained previously with this surface preparation [5,10,38,40,41]. Cyclic loading was applied then with a 100 kN Instron servo-hydraulic testing machine. The specimen was pre-cracking under mode I load for 120,000 cycles at a frequency of 10 Hz, a load ratio ($R$) of 0.1 and a stress intensity range ($\Delta K_I$) of 8 MPa$\sqrt{m}$ so that the crack length was 20.30 mm ($a/W$ = 0.40). Displacements were then measured under $R$ = 0.3 and

**Table 1**
Parameters used in previous works for estimating the SIF with DIC.

| Author | FOV (mm$^2$) | Crack portion inside AOI ($\lambda$) | Subset size (pixel) | Excluding plastic zone | No. of higher order terms |
|---|---|---|---|---|---|
| Peters et al. [30] | 8 | Crack included | Not-mentioned | Not mentioned | Convergence value |
| McNeill et al. [1] | 12.7 × 12.7 | 65% | Not mentioned | No | Up to 48 terms |
| Yoneyama et al. [32] | 6 × 5 | 50% | Not mentioned | No | Up to 10 terms |
| Hamam et al. [12] and Roux et al. [36] | 2 × 2 | 65% and 45% | 12 | Yes | Sub/super singular terms |
| Yusof et al. [37] | ∼12 | 50% | 12 | Yes | Muskhilishvili's app. |
| Lopez-Crespo et al. [38] | 18 × 24 | 50% | 32 | Yes | Muskhilishvili's app. |
| Yates et al. [5] | 22 × 16 | 30% | Not mentioned | No | Up to 15 terms |
| Dehnavi et al. [35] | Not-mentioned | 30% | 21 | Yes | 4 terms |

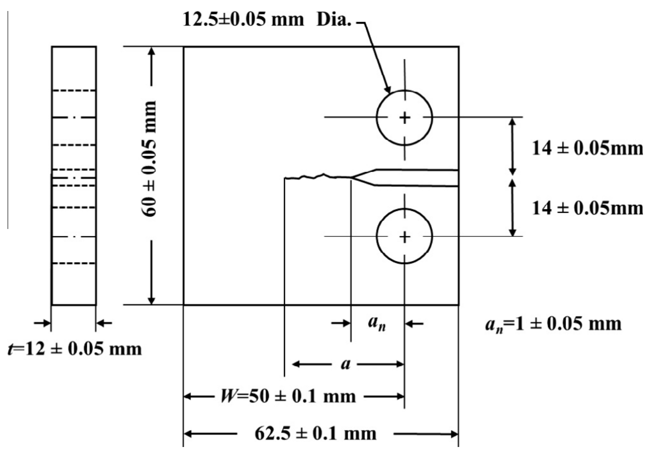


**Fig. 1.** Geometry of the CT specimen in accordance with ASTM standard [39].

**Table 2**
Mechanical properties of 2024-T351 aluminium alloy.

| Young modulus | Yield stress | UTS | Elongation at break | Brinell hardness |
|---|---|---|---|---|
| 73 GPa | 325 MPa | 470 MPa | 20% | 137 |

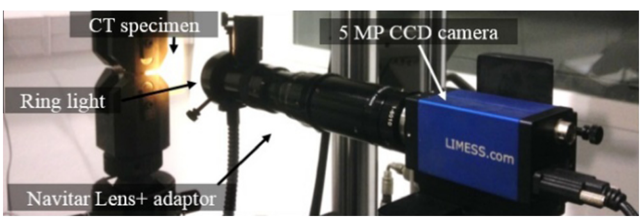


**Fig. 2.** Imaging configuration for DIC.

$\Delta K_I$ = 11 MPa$\sqrt{m}$. Small scale yielding conditions were met in all tests.

An 8-bit 2452 × 2052 pixels CCD camera with the maximum frame rate at full resolution of 12 was used for taking images. Fields of view between 0.98 × 0.82 mm$^2$ and 13.5 × 11.3 mm$^2$ were imaged with a combination of a macro Navitar lens and an adaptor tube (see Fig. 2). The resulting magnifications ranged from 0.35× to 9× (resolution ranging from 10 to 0.4 micron per pixel). Increasing the magnification results in smaller FOV. A fibre optic ring light (see Fig. 2) was used to achieve uniform illumination on the surface of the specimen. In addition, a Questar 3-axis stage was used to mount and adjust the camera position precisely. All AOIs used in this work were squared. In order to acquire a sufficient number of images (38 images per cycle), the loading rate was reduced to 0.1 Hz while capturing the images. Vic-Snap software [42] has been utilised for capturing the images and the corresponding applied load on the specimen for each image. Images were taken in six different magnifications. Subsequently, the images were processed with Vic-2D software [42] to obtain the displacement fields. Each image was compared to the initial reference image at the $P_{min}$. Step size (the distance between two consecutive displacement vectors) was set to 1/4 of the subset size in order to achieve independent and non-repetitive data. A high-order interpolation scheme of optimized 8-tap spline was used to achieve sub-pixel accuracy. The correlation criterion was set to the zero-normalized sum of squared differences which is insensitive to offset and scale in lighting [43]. Using the covariance matrix of the correlation equation, a statistical confidence region has been calculated in pixel for each match [43]. This confidence interval is a measurement of the quality of matching the points in subsets [43]. Illumination, surface finish, magnification, subset size and step were set so that, the standard deviation confidence interval ($E$) was lower than $2 \times 10^{-2}$ pixel (i.e. 2% of a pixel) in all analyses reported here.

In order to determine the effect of subset size on the accuracy of the displacement field measurement, DIC was done in different subset sizes ranging from 13 to 199 pixels for two different magnifications of 0.75× and 0.35×. The crack-tip position was determined optically from high magnification images at $P_{max}$. The obtained displacement data was then fitted into Williams' series [27]:

$$\text{Mode I}\begin{cases} u_I = \sum_{n=1}^{\infty} \frac{r^{\frac{n}{2}}}{2\mu} a_n \left\{ \left[\kappa + \frac{n}{2} + (-1)^n\right] \cos\frac{n\theta}{2} - \frac{n}{2}\cos\frac{(n-4)\theta}{2} \right\} \\ v_I = \sum_{n=1}^{\infty} \frac{r^{\frac{n}{2}}}{2\mu} a_n \left\{ \left[\kappa - \frac{n}{2} - (-1)^n\right] \sin\frac{n\theta}{2} + \frac{n}{2}\sin\frac{(n-4)\theta}{2} \right\} \end{cases} \quad (1)$$

and

$$\text{Mode II}\begin{cases} u_{II} = -\sum_{n=1}^{\infty} \frac{r^{\frac{n}{2}}}{2\mu} b_n \left\{ \left[\kappa + \frac{n}{2} - (-1)^n\right] \sin\frac{n\theta}{2} - \frac{n}{2}\sin\frac{(n-4)\theta}{2} \right\} \\ v_{II} = \sum_{n=1}^{\infty} \frac{r^{\frac{n}{2}}}{2\mu} b_n \left\{ \left[\kappa - \frac{n}{2} + (-1)^n\right] \cos\frac{n\theta}{2} + \frac{n}{2}\cos\frac{(n-4)\theta}{2} \right\} \end{cases} \quad (2)$$

where $u$ and $v$ are horizontal and vertical displacements, $\mu$ is the shear modulus and $\kappa = (3 - v)/(1 + v)$ for plane stress and for plane strain condition, $v$ is the Poisson's ratio, $r$ and $\theta$ are radial and phase distance from the crack, $a_n$ is constant.

Eq. (1) can be written in terms of the stress intensity factor and T-stress as follows [5]:

$$u = \frac{K_I}{2\mu}\sqrt{\frac{r}{2\pi}}\cos\frac{\theta}{2}\left(\kappa - 1 + 2\sin^2\frac{\theta}{2}\right) + \frac{K_{II}}{2\mu}\sqrt{\frac{r}{2\pi}}\sin\frac{\theta}{2}\left(\kappa + 1 + 2\cos^2\frac{\theta}{2}\right) + \frac{T}{8\mu}r(\kappa+1)\cos\theta + a_0 - Rr\sin(\theta) \quad (3)$$

$$v = \frac{K_I}{2\mu}\sqrt{\frac{r}{2\pi}}\sin\frac{\theta}{2}\left(\kappa + 1 - 2\cos^2\frac{\theta}{2}\right) + \frac{K_{II}}{2\mu}\sqrt{\frac{r}{2\pi}}\cos\frac{\theta}{2}\left(\kappa - 1 - 2\cos^2\frac{\theta}{2}\right) + \frac{T}{8\mu}r(\kappa-3)\sin\theta + b_0 + Rr\cos(\theta) \quad (4)$$

where $a_0$ and $b_0$ accounts for the rigid body translation and $R_0$ is used to compensate for the rigid body rotation. It can be shown that

$$K_I = a_1\sqrt{2\pi}, \quad K_{II} = -b_1\sqrt{2\pi}, \quad T = 4a_2 \quad (5)$$

where $K_I$ and $K_{II}$ are the mode I and II of stress intensity factor, respectively and $T$ represents T-stress. Since CT can only be loaded nominally to pure mode I loads, the results and the discussion will focus on $K_I$. The effects of adding non-singular terms (up to 10 terms) in Williams' solution was also explored. Fig. 3 shows an example of the vertical displacement contour for a FOV of 6 × 6 mm$^2$ as well as the quality of fitting the experimental data and the regression results by considering one, two and nine terms in Williams' series. Fig. 3 illustrates the improvement in the fitting when increasing the number of terms in the series.

The results were then validated by comparison with nominal SIF solution ($K_{I\ nom}$) [44]. Since nominal values do not include any closure effect, care was taken to generate results with as little influence as possible from closure-related mechanisms. To this end, $\Delta K_I$ and load ratio were higher during the cycles used for evaluating the SIF than during the pre-cracking process. [45]. Following [46], COD was evaluated at several distances behind the crack-tip, from 50 to 400 μm. Fig. 4 shows the compliance curve (load versus COD) measured 120 μm behind the crack-tip, in a similar way to [45]. The very low deviation from linearity of the curve in Fig. 4

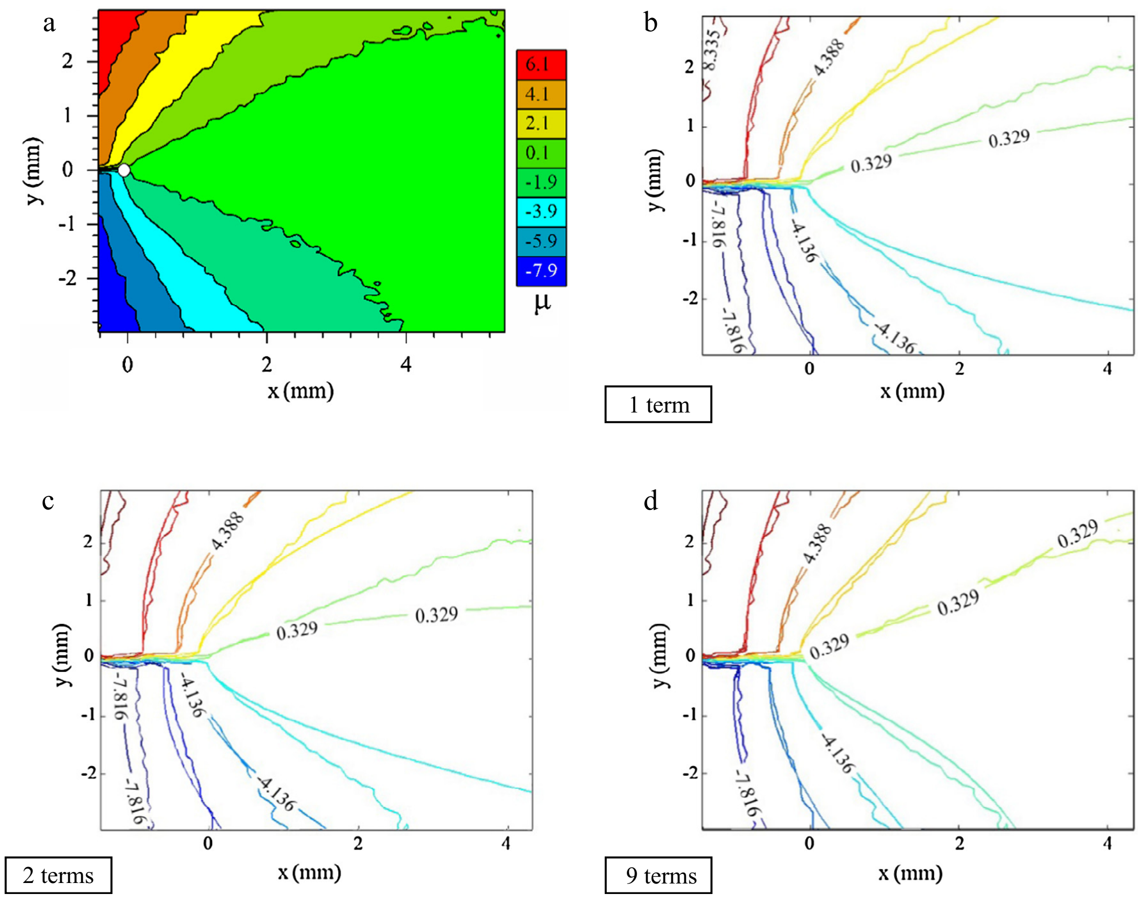


**Fig. 3.** The vertical displacement contour for a FOV of 6 × 6 mm$^2$ at the maximum load (a) and the quality of the fitting the experimental data and regression results by considering one (b), two (c) and nine (d) terms in Williams' series.

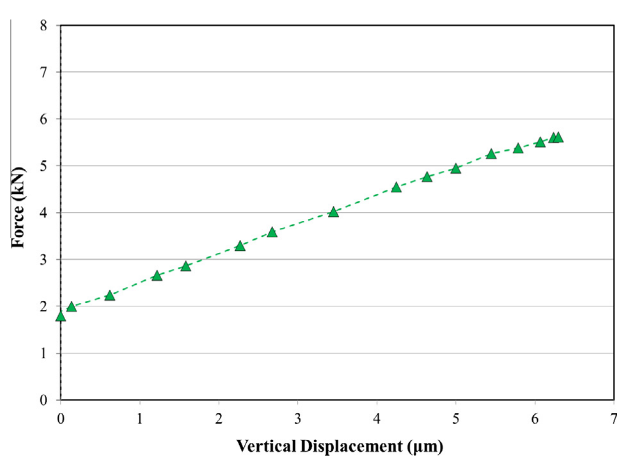


**Fig. 4.** Measured COD for the sample.

indicates that closure mechanisms had little or no effect. Similar behaviour was observed in the whole experiment.

The accuracy of experimental results was then examined through the $\delta$ parameter defined as follows:

$$\delta = \left|\frac{K_{\mathrm{I\ exp}} - K_{\mathrm{I\ nom}}}{K_{\mathrm{I\ nom}}}\right| \times 100 \tag{6}$$

where $K_{\mathrm{I\ exp}}$ is evaluated with Eq. (1) and $K_{\mathrm{I\ nom}}$ is computed from [44]. Low $\delta$ indicates more accurate estimations of $K_{\mathrm{I}}$.

In order to evaluate the effect of the AOI position, $\lambda$ is defined as:

$$\lambda = \frac{a_{\mathrm{in}}}{L} \times 100 \tag{7}$$

where $a_{\mathrm{in}}$ is the length of a part of the crack inside AOI and $L$ represents the longitude length of the AOI. For this experiment, four values of $\lambda$ are selected, including 50%, 25%, 0%, and −25%. Negative values of $\lambda$ represent an AOI locating ahead of the crack-tip and not including the crack-tip, that is collecting data only ahead of the crack-tip, in a similar way to [9]. Fig. 5a and b shows two schematics of how $\lambda$ values of −25% and 50% could be achieved.

To study the effect of the size of the AOI on the estimation of SIFs, six different AOIs in a constant FOV were analysed (Fig. 6). Minimum required data points in an AOI of 1 × 1 mm$^2$ for an estimation error less than 10% ($\delta$) is also examined. It should be mentioned that variables such as FOV and plastic zone size are interrelated. In other words, by decreasing the FOV in order to study its effect on the estimation accuracy of the $K_{\mathrm{I}}$, the size of the plastic zone in proportion to the FOV will be reversibly increased simultaneously. In this way, a larger portion of the data points will be located inside the plastic zone. Load related effects such as different $\Delta K$ and $K_{\max}$ values are not studied in this work not because their effect is negligible but because they lie beyond the scope of the current work.

## 3. Results and discussion

### 3.1. Effect of subset size

The first parameter that was studied was the subset size used in DIC technique. While small subset sizes are required to study

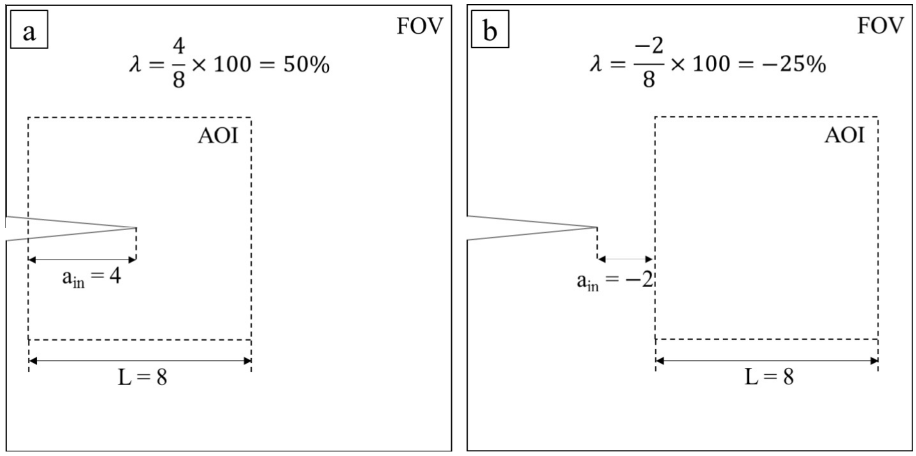


**Fig. 5.** Schematics of AOI position ($\lambda$ parameter) with respect to the crack-tip. (a) shows the case where the crack-tip is located in the centre of the AOI ($\lambda$ = 50%). (b) shows an example where all the DIC information is collected ahead of the crack-tip ($\lambda$ = −25%).

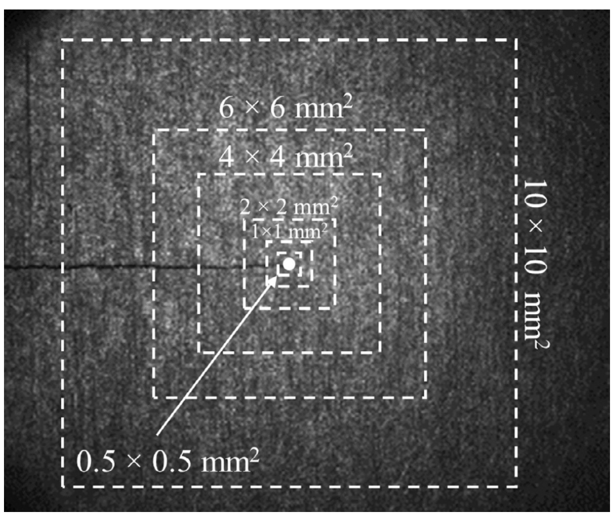


**Fig. 6.** The difference between FOV and AOI. The FOV is the size of the whole image. Six different AOIs are defined within the FOV when $\lambda$ = 50%.

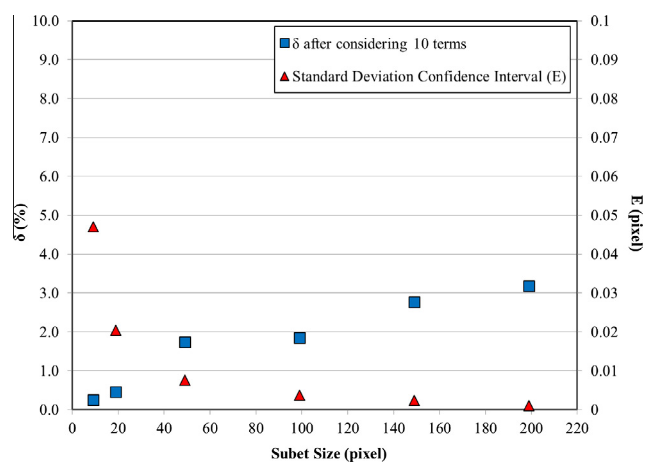


**Fig. 7.** Evolution of SIF accuracy ($\delta$) and standard deviation confidence interval ($E$) with the subset size in the magnification of 0.75× (FOV of 6 × 6 mm$^2$).

heterogeneous displacement fields [21], too small subsets can increase the random errors of the technique [47]. Consequently, the subset size must be defined carefully [48]. Fig. 7 shows the evolution of the standard deviation confidence interval ($E$) and $\delta$ with increasing the subset size. It can be seen that $E$ decreased as the subset size increased. This is in agreement with the reverse power law relation between $E$ and the subset size observed by Hild et al. [15]. The largest drop in E was observed by increasing the subset size from 13 to 49 pixels. For subset sizes greater than 49 pixels (229 μm), a slight decrease in $E$ was also observed.

Fig. 7 also shows that $\delta$ increases steadily from 0.25% to 3.18% by increasing the subset size from 13 to 199 pixels. Increasing $\delta$ as a result of enlarging the subset size is probably due to the low resolution in the displacement field in the crack-tip region, where large gradients occur. It was also observed that for the studied range of subset sizes, quite good results were obtained both in terms of SIF accuracy ($\delta$) and the quality of the correlation of the DIC technique ($E$). That is, a combination of a 5 mega-pixel camera and scratched surface with sand paper make it possible to use a wide range of subset sizes. The physical length of each pixel in high-resolution cameras is small enough to get sufficient number of data points even if large subset sizes are used. Scratching the surface with different grades of sandpaper provided sufficient intensity gradients in each subset, even for the smallest one, 13 × 13 pixels, for which the confidence interval is still acceptable (less than 5%). Subset sizes ranging from 13 to 199 pixels (61 to 935 μm), in the FOV of 6 × 6 mm$^2$ produced satisfactory results in terms of accurate estimation of SIF.

### 3.2. Effect of the plastic zone

The existence of a stress singularity at the crack-tip can be described by an elastic stress field solution [27]. Since the analytical models employed are based on LEFM, no points are normally collected within the plastic zone [16,40]. The size of the cyclic plastic zone can be determined as follows [49]:

$$r = \frac{1}{\pi}\left(\frac{\Delta K_I}{2\sigma_y}\right)^2 \quad (8)$$

For the current experiment the size of the monotonic and cyclic plastic zone were 346 μm and 88 μm respectively. Fig. 8 shows the effect of excluding monotonic and cyclic plastic zone on the results of estimating the SIF for different FOVs, employing 9 terms of Williams' series and $\lambda$ = 25%. It can be seen provided the FOV is larger than 1 × 1 mm$^2$, removing the plastic zone area has a negligible effect on the SIF estimation. The interesting point is that excluding monotonic or cyclic plastic zone has worsened the evaluation

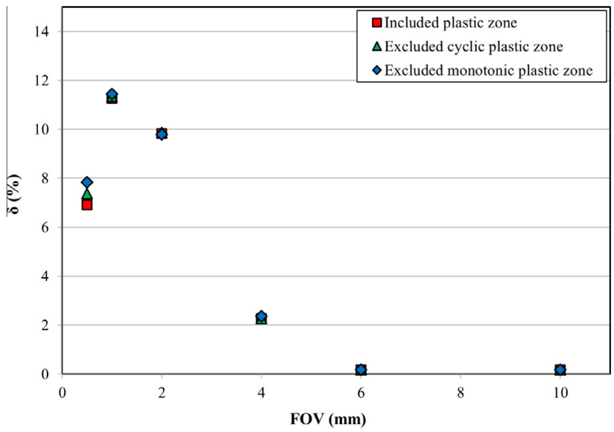


**Fig. 8.** Effect of including and excluding the monotonic and cyclic plastic zone in the algorithm for estimating the SIF for different FOVs.

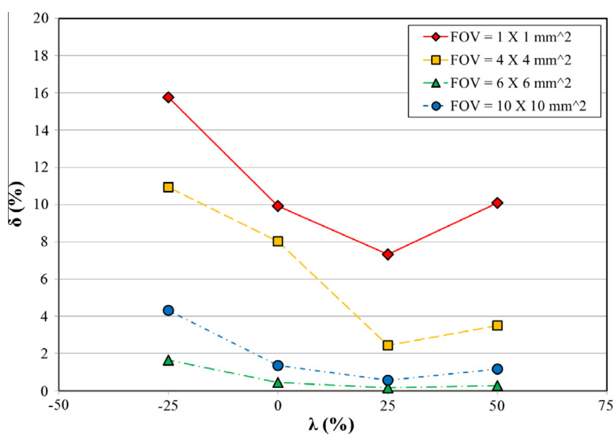


**Fig. 9.** The behaviour of $\delta$ as a function of $\lambda$ for different FOVs. Nine terms in Williams' expansion were used in all cases.

accuracy of $K_I$. This behaviour can be explained by noting that, unlike with stress field, there is no singularity at the crack-tip for displacement field [50]. Accordingly, good fitting can be obtained at the immediate vicinity of the crack-tip with displacement fields (Fig. 3b). In fact removing plastic zone not only has not improved the estimation of $K_I$ but it has also worsened the estimation as a result of removing a number of data points near the crack-tip. This effect is more significant in the smallest FOV, where monotonic plastic zone includes almost 40% of data points. It is worth noting that the size of the plastic zone is smaller than the subset size (41 × 41 pixels) for FOVs larger than 4 × 4 mm$^2$. Similar results were also obtained previously when estimating the SIF with the Von-Mises approach [10] and Williams' approach [5].

### 3.3. Effect of area of interest (AOI) position

The current section aims at studying the influence of the crack-tip position within the AOI. Most authors use displacement data from the region ahead of the crack-tip (see Table 1). Nevertheless, the best signal to noise ratio and largest gradients take place behind the crack-tip (i.e. in the crack flanks). The AOI position is studied here through the $\lambda$ parameter defined in Section 2. The results of estimating the SIF for different $\lambda$ parameters and different FOVs are summarised in Fig. 9. The curves corresponding to different FOVs show a minimum in $\delta$ for $\lambda$ parameter of 25%. That is, for all FOVs, the best results are obtained when the crack-tip is included in the AOI and crack extends over one fourth of the FOV. Fig. 9 also shows that the gap between different values of $\lambda$ parameter is larger for smaller FOVs. In other words, the AOI position has a large influence for high magnification DIC. The results suggest that AOI position is more important for FOV smaller than 4 × 4 mm$^2$. Fig. 10 investigates the combined effect of different number of terms in the series and different AOI positions for the FOV of 4 × 4 mm$^2$. Fig. 10a shows the results in terms of the error in estimating the SIF (in %) and Fig. 10b shows the $K_I$ estimated from the experimental DIC data.

Fig. 10a shows that the best predictions are obtained for $\lambda$ = 25% for all FOVs studied. Overall, $\lambda$ = −25% seems to produce the worst SIF predictions, thus indicating that the crack-tip should be at least partially contained within the AOI. Fig. 10a also shows that for more than 6 number of terms used in the series, $\lambda$ = 25% and $\lambda$ = 50% yield similar results, both of them being quite accurate (less than 4% error in SIF estimation). Fig. 10b shows that collecting displacement data only from the area ahead of the crack-tip, $\lambda$ = 0% or −25%, results in an underestimation of $K_I$ when the first two terms are considered.

### 3.4. Effect of field of view (FOV)

The next parameter that will be studied is the size of the FOV. Fig. 11 illustrates the influence of the size of the FOV on $\delta$ for different number of terms when $\lambda$ was set to 25% and 0%.

Fig. 11 highlights the relation between the FOV, the position of the crack-tip within the AOI ($\lambda$) and the number of terms for SIF estimation. It can be seen from Fig. 11a that good estimation of the $K$ can be obtained for FOV between 4 and 10 mm, by taking into account up to 10 terms in Williams' series. Fig. 11b shows a better estimation for 1–3 terms on small FOV (up to 2 mm). Beyond FOV larger than 4 mm, more terms are required to obtain good estimations. Comparison between Fig. 11a and b suggests that including a part of the crack in the fitting process improves the SIF estimations. Fig. 11b indicates that unless part of the crack is imaged, large scattering is observed when considering few or more terms. The predictions obtained with $\lambda$ = 0% and one term of the series (Fig. 11b) were satisfactory (less than 4%) for small FOV. This is probably due to having all the data from within the K-dominated zone. This is in agreement with previous literature that points out that sub-singular terms in the Williams' series representation (K and T-stress) are sufficient to determine the field quantity of interest [50]. In addition, enlarging FOV from 2 × 2 mm$^2$ to 4 × 4 mm$^2$ has resulted in considerable increase in the error of $K_I$ estimation by only using the first term. This behaviour is logical since higher order terms are required for describing accurately large crack-tip fields. Fig. 11b suggests that the boundary of K-dominance zone is at a distance of 2–4 mm from the crack-tip. It should be mentioned that according to small scale yielding condition, process zone should be confined well inside the region of K dominance [49].

Using FOVs larger than 4 × 4 mm$^2$ did not have a significant effect on $K_I$ estimation as long as higher order terms are considered. Considering higher order terms is essential for high accuracy estimation in larger FOVs where $K$ is no longer dominant [5]. It can be seen that by selecting the optimum parameters (FOV = 6 × 6 mm$^2$, $\lambda$ = 25%, subset = 41 × 41 pixels) the maximum value of $\delta$ is 0.15%.

Another interesting question that an experimentalist may encounter with is the possibility of using a small AOI in a large FOV for $K_I$ estimation. Such an arrangement would enable one to use a lens with low magnification (e.g. 0.35×, i.e. 10 μm/pixel), for studying small AOIs. Fig. 12 compares using different AOIs in the largest FOV and using different AOIs with magnifications adjusted to each AOI.

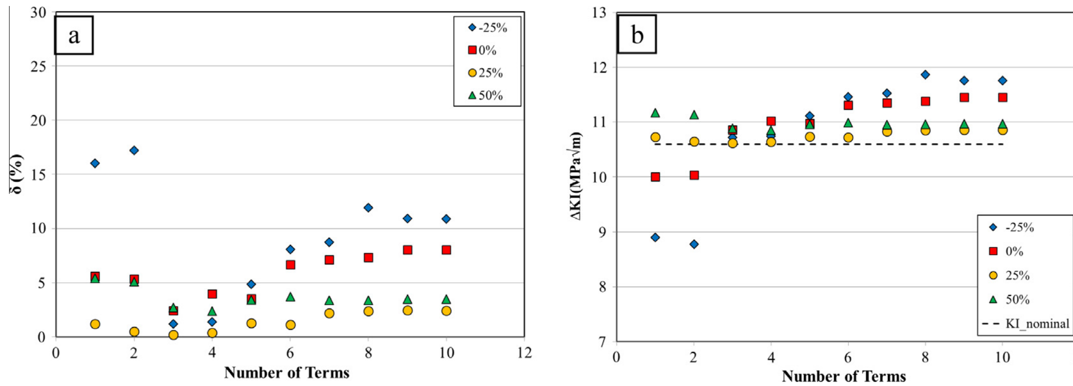


**Fig. 10.** Effect of considering higher order terms on $\delta$ (a) and the absolute value (b) of the estimated $K_I$ for different positions of AOI in the FOV of $4 \times 4\ \text{mm}^2$.

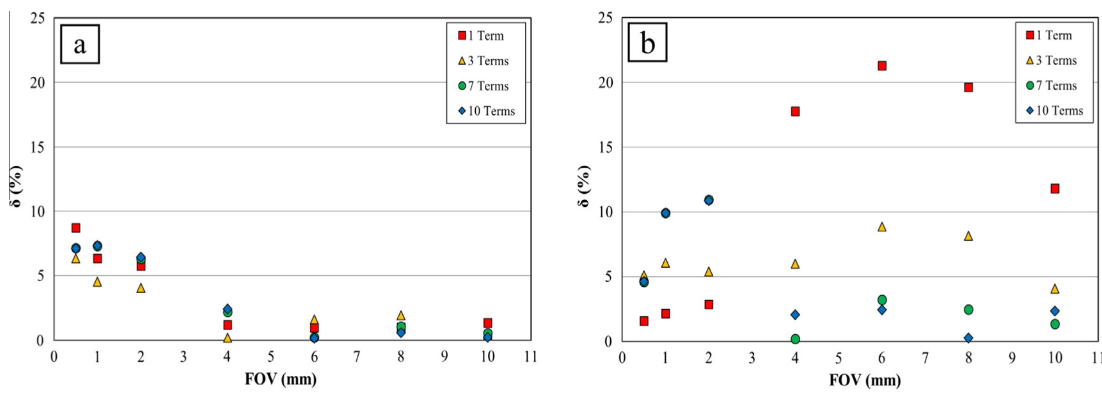


**Fig. 11.** The accuracy of $K_I$ estimation ($\delta$) as a function of FOV for different number of terms. $\lambda$ is equal to 25% (a) and 0% (b).

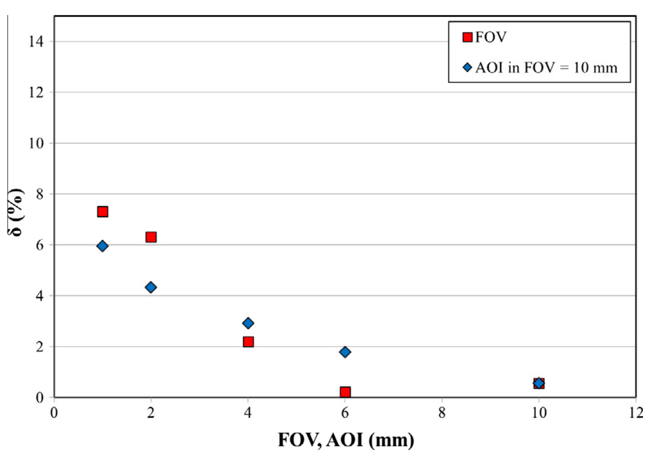


**Fig. 12.** $K_I$ estimation accuracy with respect to the different size of AOIs in the FOV equal to $10 \times 10\ \text{mm}^2$ and corresponding FOVs by considering 9 terms in Williams' series.

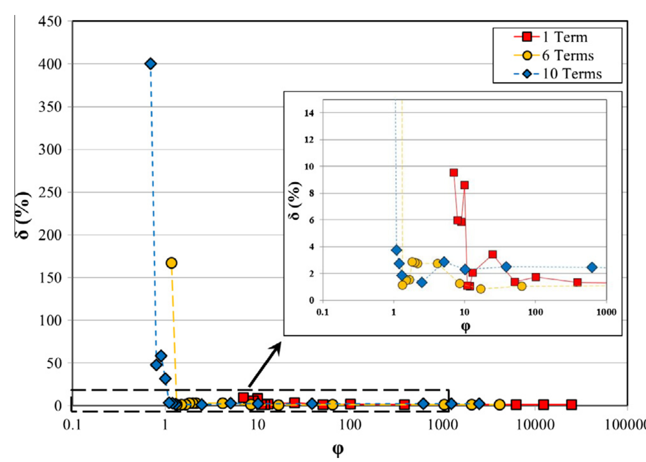


**Fig. 13.** Effect of reducing data points in an AOI of $4 \times 4\ \text{mm}^2$ where $\lambda = 25\%$. $\varphi$ is defined as the number of data points used in the analysis divided by the number of terms in the series. Note the logarithmic scale in $\varphi$ scale.

Fig. 12 shows that using a small AOI (even one-tenth of the FOV) will result in the same accuracy as using small FOV by utilising high magnification lenses. One of the advantages of using small AOI is the fewer number of data points required to be analysed. For example, the number of data points in the FOV of $1 \times 1\ \text{mm}^2$ with the subset size of $41 \times 41$ pixels is equal to 24,364. For the corresponding AIO (size of $1 \times 1\ \text{mm}^2$) in the FOV of $10 \times 10\ \text{mm}^2$, just 64 data points are needed to be analysed.

This observation suggests that the system of equations solved to evaluate the SIF is excessively and unnecessarily over-determined. The degree of over-determination in the multi-point over-deterministic method can be studied through the parameter $\varphi$, defined as:

$$\varphi = \frac{\text{number of data points}}{\text{number of terms in series}} \tag{9}$$

Fig. 13 shows the accuracy of SIF estimation for different values of $\varphi$. The horizontal axis is shown in logarithmic scale. Data are collected from the FOV of $4 \times 4\ \text{mm}^2$. It can be seen the value of $\delta$ remains stable as long as $\varphi > 15$. Fig. 13 also shows that decreasing $\varphi$ from 1.1 to 0.7 (or reducing the data points from 11 to 7) made a drastic increase in $\delta$ from 3.74% to 400% for calculations based on 10 terms. Very similar trends were also observed for other FOVs. $\varphi = 0.7$ is not strictly a multi-point over-deterministic method since the system is under-deterministic. Nevertheless, the results for $\varphi = 0.7$ are included for the sake of making the current analysis more comprehensive. The same trend is also observed for 6 number of terms. For the first term, however, since the over-deterministic condition is still satisfied even by seven data points, $\delta$ did not change significantly (less than 10%). Consequently, this analysis suggests that in the optimum condition ($\lambda = 25\%$, FOV > $4 \times 4\ \mathrm{mm}^2$), reliable SIF estimations ($\delta < 4\%$) can be obtained as long as $\varphi > 15$. By further increasing $\varphi$ parameter beyond 15, the effect of experimental noise and the effect of the microstructure can be reduced. Increasing $\varphi$ well beyond 15 can easily be done using current digital cameras. However, depending on the DIC algorithm in use, the computational cost of analysing 1000 times more data points will also increase.

## 4. Conclusions

A multi-parameter fracture mechanics study on the effect of some experimental variables on $K_I$ estimation using DIC was conducted based on an elastic model. It was shown that the accuracy of $K_I$ can be affected not only by the well-known variables such as subset size in DIC and considered number of Williams' series but also by the size and position of AOI. When using scratches at the surface, good estimations can be obtained with subset sizes between 13 and 199. The absence of singularity in the displacement data at the crack tip region led to a reasonable fitting in the experimental data and the regression results even quite close to the crack-tip. Therefore, excluding the plastic zone (monotonic or cyclic) is not recommended as long as FOV is smaller than $1 \times 1\ \mathrm{mm}^2$. Experimental results indicate the significant effect of the position of the AOI for accurate estimation of SIF with DIC technique. It was shown that including a part of the crack length inside the AOI (crack extending to one-fourth of the AOI) provides the best estimations for all FOVs. Accurate predictions can be obtained imaging FOVs between $4 \times 4\ \mathrm{mm}^2$ and $10 \times 10\ \mathrm{mm}^2$, $\lambda = 25\%$ and using 1 to 10 terms in Williams' expansion. Worse estimations were obtained for FOVs smaller than $4 \times 4\ \mathrm{mm}^2$. Finally, it was also shown that reliable estimations of the $K_I$ can be achieved as long as the number of displacement vectors fitted to the model is 15 times larger than the number of terms in the series. Increasing the number of displacement vectors beyond 15 can be useful to reduce noise effects, thus improving the quality of the estimation.

## Acknowledgements

Financial support of Junta de Andalucía through Proyectos de Excelencia grant reference TEP-3244 and the University of Malaga through Campus de Excelencia Internacional del Mar (CEIMAR) is greatly acknowledged.

## References

[1] McNeill SR, Peters WH, Sutton MA. Estimation of stress intensity factor by digital image correlation. Eng Fract Mech 1987;28:101–12. http://dx.doi.org/10.1016/0013-7944(87)90124-X.
[2] Sutton MA, Zhao W, McNeill SR, Helm JD, Piascik RS, Riddell WT. Local crack closure measurements: development of a measurement system using computer vision and a far-field microscope. In: McClung RC, Newman JC, editors. Adv Fatigue Crack Clos Meas Anal, 2. West Conshohocken, PA: ASTM STP 1343; 1999. p. 145–56.
[3] Yoneyama S, Arikawa S, Kusayanagi S, Hazumi K. Evaluating J-integral from displacement fields measured by digital image correlation. Strain 2014;50:147–60. http://dx.doi.org/10.1111/str.12074.
[4] Becker TH, Mostafavi M, Tait RB, Marrow TJ. An approach to calculate the J-integral by digital image correlation displacement field measurement. Fatigue Fract Eng Mater Struct 2012;35:971–84. http://dx.doi.org/10.1111/j.1460-2695.2012.01685.x.
[5] Yates JR, Zanganeh M, Tai YH. Quantifying crack tip displacement fields with DIC. Eng Fract Mech 2010;77:2063–76. http://dx.doi.org/10.1016/j.engfracmech.2010.03.025.
[6] Roux S, Hild F. Stress intensity factor measurements from digital image correlation: post-processing and integrated approaches. Int J Fract 2006;140:141–57. http://dx.doi.org/10.1007/s10704-006-6631-2.
[7] Zanganeh M, Tomlinson RA, Yates JR. T-stress determination using digital image correlation. In: XIth congrees expo exp appl mech Orlando, Florida, USA.
[8] Leser WP, Carolina N, Carolina N, Newman JA, Johnston WM. Fatigue crack closure analysis using digital image correlation. NASA/TM-2010-216695; 2010.
[9] Vasco-Olmo JM, Díaz FA, García-Collado A, Dorado-Vicente R. Experimental evaluation of crack shielding during fatigue crack growth using digital image correlation. Fatigue Fract Eng Mater Struct 2015;38:223–37. http://dx.doi.org/10.1111/ffe.12136.
[10] Carroll J, Efstathiou C, Lambros J, Sehitoglu H, Hauber B, Spottswood RC S. Investigation of fatigue crack closure using multiscale image correlation experiments. Eng Fract Mech 2009;76:2384–98.
[11] Díaz FV, Kaufmann GH, Armas AF, Galizzi GE. Optical measurement of the plastic zone size in a notched metal specimen subjected to low-cycle fatigue. Opt Lasers Eng 2001;35:325–33. http://dx.doi.org/10.1016/S0143-8166(01)00030-6.
[12] Hamam R, Hild F, Roux S. Stress intensity factor gauging by digital image correlation: application in cyclic fatigue. Strain 2007;43:181–92. http://dx.doi.org/10.1111/j.1475-1305.2007.00345.x.
[13] Roux-Langlois C, Gravouil A, Baietto M-C, Réthoré J, Mathieu F, Hild F, et al. DIC identification and X-FEM simulation of fatigue crack growth based on the Williams' series. Int J Solids Struct 2014;53:38–47. http://dx.doi.org/10.1016/j.ijsolstr.2014.10.026.
[14] Lopez-Crespo P, Shterenlikht A, Patterson EA, Yates JR, Withers PJ. The stress intensity of mixed mode cracks determined by digital image correlation. J Strain Anal Eng Des 2008;43:769–80. http://dx.doi.org/10.1243/03093247JSA419.
[15] Hild F, Roux S. Digital image correlation: from displacement measurement to identification of elastic properties – a review. Strain 2006;42:69–80. http://dx.doi.org/10.1111/j.1475-1305.2006.00258.x.
[16] Hamam R, Hild F, Roux S. Stress intensity factor gauging by digital image correlation: application in cyclic fatigue. Strain 2007;43:181–92. http://dx.doi.org/10.1111/j.1475-1305.2007.00345.x.
[17] Roux S, Réthoré J, Hild F. Digital image correlation and fracture: an advanced technique for estimating stress intensity factors of 2D and 3D cracks. J Phys D Appl Phys 2009;42:214004. http://dx.doi.org/10.1088/0022-3727/42/21/214004.
[18] Pan B, Qian K, Xie H, Asundi A. Two-dimensional digital image correlation for in-plane displacement and strain measurement: a review. Meas Sci Technol 2009;20:062001. http://dx.doi.org/10.1088/0957-0233/20/6/062001 (17pp).
[19] Taylor JR. An introduction to error analysis: the study of uncertainties in physical measurements, vol. 51, 2nd ed. Sausalito, California; 1983. http://dx.doi.org/10.1119/1.13309.
[20] Schreier HW, Braasch JR, Sutton MA. Systematic errors in digital image correlation caused by intensity interpolation. Opt Eng 2000;39:2915–21.
[21] Schreier HW, Sutton MA. Systematic errors in digital image correlation due to undermatched subset shape functions. Exp Mech 2002;42:303–10. http://dx.doi.org/10.1177/0014485023215483910.
[22] Yu L, Pan B. The errors in digital image correlation due to overmatched shape functions. Meas Sci Technol 2015;26:045202. http://dx.doi.org/10.1088/0957-0233/26/4/045202.
[23] Fazzini M, Mistou S, Dalverny O, Robert L. Study of image characteristics on digital image correlation error assessment. Opt Lasers Eng 2010;48:335–9. http://dx.doi.org/10.1016/j.optlaseng.2009.10.012.
[24] Pan B. Reliability-guided digital image correlation for image deformation measurement. Appl Opt 2009;48:1535–42. http://dx.doi.org/10.1364/AO.48.001535.
[25] Sanford RJ, Dally JW. A general method for determining mixed-mode stress intensity factors from isochromatic fringe patterns. Eng Fract Mech 1979;11:621–33. http://dx.doi.org/10.1016/0013-7944(79)90123-1.
[26] Westergaard HM. Bearing pressures and cracks. J Appl Mech 1939;61:A49–53.
[27] Williams ML. On the stress distribution at the base of a stationary crack. J Appl Mech 1957;24:109–14. http://dx.doi.org/10.1115/1.3640470.
[28] Díaz FA, Yates JR, Patterson EA. Some improvements in the analysis of fatigue cracks using thermoelasticity. Int J Fatigue 2004;26:365–76. http://dx.doi.org/10.1016/j.ijfatigue.2003.08.018.
[29] Christopher CJ, James MN, Patterson EA, Tee KF. Towards a new model of crack tip stress fields. Int J Fract 2007;148:361–71. http://dx.doi.org/10.1007/s10704-008-9209-3.
[30] Peters WH, Ranson WF, Kalthoff JF, Winkler SR. A study of dynamic near-crack-tip fracture parameters by digital image analysis. J Phys Colloq 1985;46. http://dx.doi.org/10.1051/jphyscol:1985581. C5-631–C5-638.
[31] Ramesh K, Gupta S, Kelkar AA. Evaluation of stress field parameters in fracture mechanics by photoelasticity – revisited. Eng Fract Mech 1997;56:25–41. 43–5.

[32] Yoneyama S, Ogawa T, Kobayashi Y. Evaluating mixed-mode stress intensity factors from full-field displacement fields obtained by optical methods. Eng Fract Mech 2007;74:1399–412. http://dx.doi.org/10.1016/j.engfracmech.2006.08.004.

[33] Berto F, Lazzarin P. On higher order terms in the crack tip stress field. Int J Fract 2010;161:221–6. http://dx.doi.org/10.1007/s10704-010-9443-3.

[34] Berto F, Lazzarin P. Multiparametric full-field representations of the in-plane stress fields ahead of cracked components under mixed mode loading. Int J Fatigue 2013;46:16–26. http://dx.doi.org/10.1016/j.ijfatigue.2011.12.004.

[35] Dehnavi MY, Khaleghian S, Emami A, Tehrani M, Soltani N. Utilizing digital image correlation to determine stress intensity factors. Polym Test 2014;37:28–35. http://dx.doi.org/10.1016/j.polymertesting.2014.04.005.

[36] Roux S, Réthoré J, Hild F. Recent progress in digital image correlation: from measurement to mechanical identification. J Phys: Conf Ser 2008;135:012002. http://dx.doi.org/10.1088/1742-6596/135/1/012002.

[37] Yusof F, Withers PJ. Real-time acquisition of fatigue crack images for monitoring crack-tip stress intensity variations within fatigue cycles. J Strain Anal Eng Des 2008;44:149–58. http://dx.doi.org/10.1243/03093247JSA440.

[38] Lopez-Crespo P, Shterenlikht A, Yates JR, Patterson EA, Withers PJ. Some experimental observations on crack closure and crack-tip plasticity. Fatigue Fract Eng Mater Struct 2009;32:418–29. http://dx.doi.org/10.1111/j.1460-2695.2009.01345.x.

[39] ASTM E647-00. Standard test method for measurement of fatigue crack growth rates. Am Soc Test Mater Annu B Stand 1999.

[40] López-Crespo P, Burguete RL, Patterson EA, Shterenlikht A, Withers PJ, Yates JR. Study of a crack at a fastener hole by digital image correlation. Exp Mech 2009;49:551–9. http://dx.doi.org/10.1007/s11340-008-9161-1.

[41] Zanganeh M, Lopez-Crespo P, Tai YH, Yates JR. Locating the crack tip using displacement field data: a comparative study. Strain 2013;49:102–15. http://dx.doi.org/10.1111/str.12017.

[42] Vic-2D software. Correlated Solutions Incorporated (C.S.Inc) <http://www.correlatedsolutions.com>.

[43] Sutton MA, Orteu J-J, Schreier HW. Image correlation for shape, motion and deformation measurements. New York: Springer; 2009. http://dx.doi.org/10.1007/978-0-387-78747-3.

[44] Murakami Y. Stress intensity factors handbook. Oxford: Pergamon Press; 1987.

[45] Beretta S, Rabbolini S, Bello AD. Multi-scale crack closure measurement with digital image correlation on Haynes 230. Frat Ed Integrità Strutt 2015;33:174–82. http://dx.doi.org/10.3221/IGF-ESIS.33.22.

[46] Yusof F, Lopez-Crespo P, Withers PJ. Effect of overload on crack closure in thick and thin specimens via digital image correlation. Int J Fatigue 2013;56:17–24. http://dx.doi.org/10.1016/j.ijfatigue.2013.07.002.

[47] Pan B, Xie H, Wang Z, Qian K, Wang Z. Study on subset size selection in digital image correlation for speckle patterns. Opt Express 2008;16:7037–48. http://dx.doi.org/10.1364/OE.16.007037.

[48] Triconnet K, Derrien K, Hild F, Baptiste D. Parameter choice for optimized digital image correlation. Opt Lasers Eng 2009;47:728–37. http://dx.doi.org/10.1016/j.optlaseng.2008.10.015.

[49] Suresh S. Fatigue of materials. 2nd ed. New York: Cambridge University Press; 1998.

[50] Ewalds HL, Wanhill RJH. Fracture mechanics. London: Arnold; 1984.

# Appendix II

Published Paper #2

**Title:** Stress intensity factor monitoring under cyclic loading by digital image correlation

**Authors:** M. Mokhtarishirazabad[1], P. Lopez-Crespo[1], M. Zanganeh[2]

[1]Department of Civil and Materials Engineering, University of Malaga, C/Dr Ortiz Ramos s/n, 29071, Malaga, Spain

[2]Jacobs Technology, NASA Johnson Space Center, Houston TX, USA

**Journal:** Fatigue & Fracture of Engineering Materials & Structures, Volume 41, Issue 10, 2018, Pages 2162-2171

Impact Factor: 2.533, Q1 in JCR

Received: 17 October 2017 | Revised: 26 March 2018 | Accepted: 29 March 2018
DOI: 10.1111/ffe.12825

SPECIAL ISSUE - CHARACTERISATION OF CRACK TIP FIELDS 4

WILEY

# Stress intensity factor monitoring under cyclic loading by digital image correlation

M. Mokhtarishirazabad[1] | P. Lopez-Crespo[1] | M. Zanganeh[2]

[1] Department of Civil and Materials Engineering, University of Malaga, C/Dr Ortiz Ramos s/n, 29071 Malaga, Spain

[2] Jacobs Technology, NASA Johnson Space Center, Houston, TX, USA

**Correspondence**
P. Lopez-Crespo, Department of Civil and Materials Engineering, University of Malaga, C/Dr Ortiz Ramos s/n, 29071 Malaga, Spain.
Email: plopezcrespo@uma.es

**Funding information**
University of Malaga through Campus de Excelencia Internacional del Mar, Grant/Award Number: CEIMAR; Ministerio de Economia y Competitividad, Grant/Award Number: MAT2016-76951-C2-2-P; University of Malaga

**Abstract**
In the present work, a methodology for structural health monitoring based on a combination of digital image correlation and an analytical elastic solution is presented. To this end, full-field displacement around a crack tip in a CT sample made of 2024-T351 Al alloy under cyclic loading was monitored at different load levels. An analytical solution based on Williams' model was used to evaluate the experimental value of the stress intensity factor (SIF) in a continuous fashion during cyclic loads. It was observed that by increasing the loading amplitude in the cyclic loading, the difference between nominal and experimental estimation of SIF increased due to the crack tip plasticity effect, which was not considered in the nominal evaluations. To consider the plasticity effect, Irwin's approach was employed. The results showed that the proposed method can successfully monitor the evolution of SIF of a sample under cyclic loading until the sudden fracture of the sample.

**KEYWORDS**
2024-T351, cyclic load, digital image correlation, stress intensity factor, structural health monitoring

## 1 | INTRODUCTION

The accuracy for structural health monitoring has been vastly improved over the last few decades thanks to the development and improvement of a wide range of techniques for monitoring the crack (damage) initiation and growth in engineering structures. Among these, non-destructive testing techniques have been extremely useful for crack monitoring. Non-destructive testing techniques can be divided into 2 main categories: direct and indirect crack length measurement methods. Direct methods are based on measuring the crack length visually, optically, or by employing X-ray radiographic testing,[1] while indirect crack length measurements are based on monitoring a change in a physical or mechanical property of the material due to the extension of the crack. For example, the change in the material electric resistance or material stiffness, due to crack growth, has led to the development

**Nomenclature:** a, crack length; $a_{corr}$, corrected crack length, sum of the crack length with first-order plastic zone size (Irwin approach); $a_n$, $b_n$, coefficients in Williams expansion; AOI, area of interest using for analysing data points inside a particular region inside the field of view; COD, crack opening displacement; CT, compact tension specimen; DIC, digital image correlation; FOV, field of view; $K_I$, $K_{II}$, stress intensity factor in modes I and II; r, radial distance from the crack-tip; $r_y$, first-order plastic zone size (Irwin approach); R, axial load ratio ($=P_{min}/P_{max}$); T, T stress, a constant stress parallel to the crack; u, v, horizontal and vertical displacement fields; $\Delta K_I$, stress intensity factor range in mode I ($=K_{I\ max} - K_{I\ min}$); $\Delta K_{II}$, stress intensity factor range in mode II ($=K_{II\ max} - K_{II\ min}$); $\Delta K_{exp}$, evaluated stress intensity factor range by mean of displacement data around the crack tip; $\Delta K_{nom}$, nominal applied stress intensity factor range calculated by analytical solution; θ, angular coordinate in the polar system; κ, $\kappa = (3-\nu)/(1+\nu)$ for plan stress and $\kappa = 3-4\nu$ for plan strain condition; μ, shear modulus; ν, Poisson ratio; σ, axial stress; $\sigma_{ys}$, yielding stress; $_\tau$, shear stress; φ, angle between axial and shear stress amplitude (see Figure 3) of electrical potential technique[2,3] and the compliance methods[4] for crack growth measurement, respectively. In the same manner, other methods such as infrared and thermal testing,[5] acoustic emission,[6] eddy current,[7,8] and ultrasonic[9,10] have been successfully employed to monitor the defect size. In addition, some efforts were aimed at improving the accuracy of these techniques by combining 2 or more of these techniques. For example, digital image correlation (DIC) has been coupled with acoustic emission technique to determine the critical stage of deformation mechanism at the onset of the plasticity of AZ31 Mg alloy.[11] Vannianparambil et al[12] combined guided ultrasonic waves, acoustic emission, and DIC with real-time and post-mortem analysis, to develop a precise structural health monitoring approach for damage detection and quantified crack length measurement. Nevertheless, most of these methods have some disadvantages that make them difficult to be adapted for industrial environments such as being very expensive and limited application to a narrow range of materials and type of defects to be detected. For example, in ultrasonic method, the accuracy is highly dependent on the operator skills, and it is not suitable for detecting short cracks.[13] The application of eddy current method is also limited to electrically conductive materials and interpretation of complex signals requires a highly skilled operator.[14] Due to the nature of the signal source, acoustic emission method is not perfectly reproducible, and it is not capable of detecting elastic deformation.[15]

While the previously described methods are used to determine the crack geometry and length, accurate damage assessment of engineering structures subjected to changing loads often requires fracture parameters of the component to be evaluated. To this end, full field techniques such as photo-elasticity,[16] thermo-elasticity,[17] Moiré interferometry,[18] DIC,[19] and synchrotron x-ray diffraction[20] have been developed to characterise crack tip fields in terms of strain, stress, and displacement. The application of DIC in fracture mechanics has increased in the last decades because it is technically easy to implement, no sophisticated sample preparation is needed, and it is basically a scale-free method. In other words, it can measure on the scale ranging from a few meters[21] to micro-meters.[22,23]This feature makes DIC very advantageous as compared with other crack tip monitoring methods. The focus of researches in DIC has been on enhancing its accuracy[24-27] and extending its application in different fields of science. Details about the principles of the method and its applications are out of the scope of this paper and are discussed elsewhere.[28,29] The stress intensity factor (SIF) is a key parameter for fatigue life prediction of engineering components prone to linear elastic failure. A number of innovative methods has been developed to evaluate SIF not only in mode I but also mixed mode of loading.[21,30,31] The prominent advantage of using the crack tip fields for evaluating SIF is that no previous knowledge of crack length, applied force, or specimen geometry is needed. This makes it very suitable for characterisation of in-service engineering components.[32] DIC has been employed[33] to study the effect of crack closure and crack tip plasticity in the evaluation of SIF for specimens under different mixed-mode loads (I + II). The SIF is normally evaluated following a multipoint over-deterministic method consisting of fitting the experimental in fitting the experimental data to an analytical model which describes the displacement field around the crack tip. In this way, the evolution of the SIF was monitored during the loading sequences. Very promising results were obtained in early studies while estimating the SIF with DIC on C-specimens and 3-point-bend specimens.[19] Improvement in digital photography allowed higher resolution images that improved the accuracy in estimating the SIF both under pure mode I and a range of mixed-mode conditions.[34] Edge-finding routines for locating the crack tip were subsequently incorporated to the program to automate the evaluation of SIF with DIC displacement data.[35] The crack-tip location was also evaluated from displacement fields with a number of numerical procedures, including reflective Newton method, Nelder-Mead Simplex method, genetic algorithm, and Pattern Search method.[36] DIC also allowed other forms of crack evaluation through different parameters. For example, T-stress and Crack Tip Opening Angle were evaluated on double cantilever specimens made of 7010T7651 aluminium alloy.[31] Elastic plastic crack assessment was achieved with different methodologies. The J-integral was estimated from a combination of DIC and finite element method displacements by applying the path and domain integral methods on annealed and unannealed pure aluminium A1050.[37] COD measurements obtained with high magnification DIC were used to evaluate crack growth and closure mechanisms for different thicknesses on 6082T6 aluminium alloy.[38] The plastic zone ahead of the crack as a way to control the rate of crack growth was assessed with DIC on specimens with artificial cracks[39] and on specimens with real fatigue cracks.[40] In this work, we show for the first time a DIC methodology for continuous monitoring of the effective SIF under a range of different cyclic loads.

## 2 | MATERIALS AND METHODS

Crack tip field was monitored by DIC method in a compact tension (CT) specimen. The specimen was machined from a rolled 2024-T351 aluminium alloy plate in the T-L direction according to ASTM standard[41] and had a thickness of 12 mm. That is, the crack propagates parallel to the rolling direction. The geometry and dimensions of the sample are shown in Figure 1. This alloy is widely used in aircraft structures such as lower wings and fuselage/pressure cabin structures due to the high strength to weight ratio and good fatigue resistance. In addition, it combines excellent fatigue properties with low environmental impact for transport applications.[42] Table 1 shows the mechanical properties of the alloy.

Following ASTM standard,[41] the sample was fatigue pre-cracked to achieve a crack length of 25.8 mm with load ratio of 0.1 ($R = 0.1$) under mode I loading. The applied nominal $\Delta K_I$ was less than 5 MPa$\sqrt{m}$ during pre-cracking, and the loading frequency was 15 Hz. Then, the surface of the sample was scratched with a 320 grade SiC sand paper to provide a random pattern required for DIC technique. Subsequent cyclic loads were applied in a ramp wave form with load ratio of 0.3 with 5 different applied nominal $\Delta K_I$ of 10, 15, 20, 25, and 30 MPa$\sqrt{m}$. Load ratio was chosen in a way to minimize the closure phenomenon[43] and maximize the range of SIF to be studied. At the end of cyclic loads, the load was increased constantly until the sudden fracture of the sample occurs under load control. Figure 2 shows the schematic of the loading sequences. Loads were applied by an Instron 8085 fatigue loading rig. Crack tip displacement fields were captured during cyclic loading with a 5 MP CCD camera coupled with a Schindler-Kreuznach Xenon 50-mm lens with a 170-mm working distance, and the

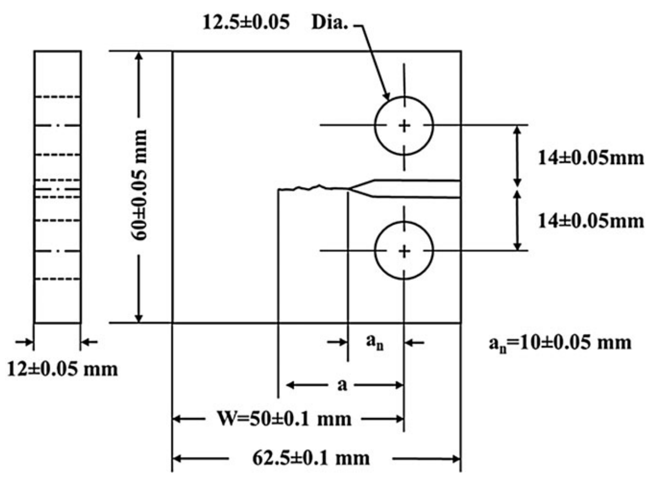


**FIGURE 1** The geometry and dimensions of the CT specimen

**TABLE 1** Mechanical properties of rolled 2024-T351 Al alloy

| Young Modulus | Yield Stress | UTS | Elongation at Break | Brinell Hardness |
|---|---|---|---|---|
| 73 GPa | 325 MPa | 470 MPa | 20% | 137 |

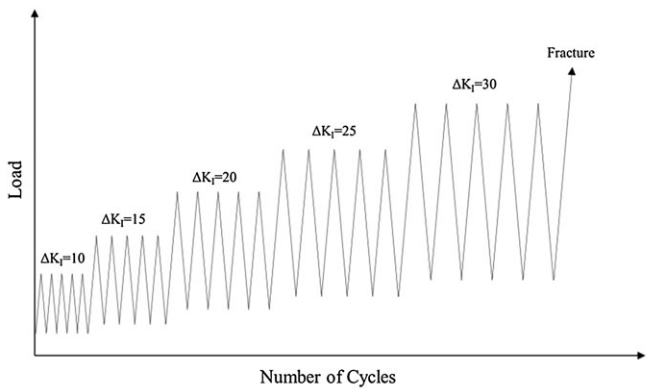


**FIGURE 2** Schematic of loading sequences

resulting field of view (FOV) was 36 × 32 mm$^2$. In this way, a resolution of 15 microns per pixel was obtained. DIC was used to generate displacement fields. The strain fields were not used in this work to avoid the numerical differentiation that often increases largely the noise level.[44]

The ring light was employed to provide an even and bright illumination over the whole field and to minimise the size of the dark region around the crack tip at high loads and the reflections (Figure 3). The position of the crack tip can be determined by analysing the displacement field with a number of numerical procedures that include reflective Newton method, Nelder-Mead Simplex method, genetic algorithm, Pattern Search method,[36] or by detecting the crack with edge-finding routines also applied on the displacement image.[35,45] In this work, the position of the crack tip was determined by direct observation of the bare surface. The image of the surface was analysed here, rather than the image of the displacement field. This is possible because the specimen surface is imaged directly, unlike other works where the actual specimen surface is covered by paint that can be applied by spray,[24] electrospray,[46] toner,[47] or others. The contrast required for the DIC algorithm to give satisfactory results is obtained by finely abrading the surface and by arranging the illumination sources in such way that reflections are minimised. Such procedure has been shown to be very useful for applications where crack tip plasticity is studied.[33]

The loading frequency was decreased to 0.5 Hz while capturing the images. This allowed 54 images to be collected during each cycle. The images were then correlated with Vic-2D software to extract the displacement data around the crack tip. The image taken at the minimum load was selected as the reference image for correlation. In order to obtain sub-pixel accuracy in the correlation, a high-order interpolation scheme of optimized 8-tap spline was employed.[48] In addition, the correlation software used a covariance matrix of the correlation equations to calculate a statistical confidence region. The confidence margin was set to 0.05 pixel, so that any data point exceeding this value

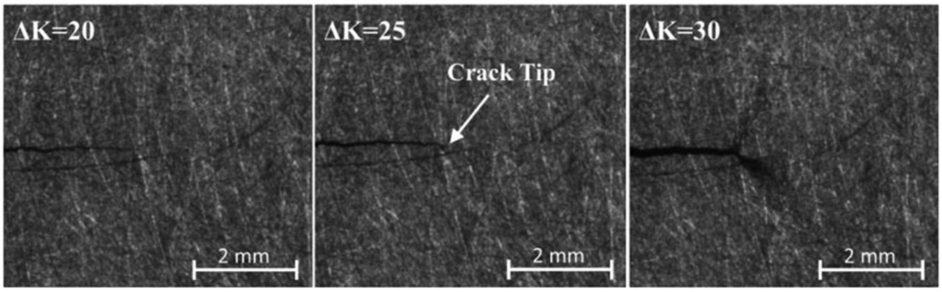


**FIGURE 3** High magnification view of the crack tip region at 3 different load levels. A small dark region can be observed only at $\Delta K_{nom} = 30\ MPa\sqrt{m}$

is removed by the algorithm.[48] To eliminate the effect of the offset and the scale in lighting, the correlation criterion was set to the zero-normalized sum of squared differences. The subset size and step-size were 39 × 39 pixels and 10 pixels, respectively (Figure 4).

A multipoint over-deterministic method was employed to calculate SIF in mode I and II, by fitting the experimental displacement data to the Williams' series[31]:

$$Model\left\{\begin{array}{l} u_I = \sum_{n=1}^{\infty} \frac{r^{\frac{n}{2}}}{2\mu} a_n \left\{\left[\kappa + \frac{n}{2} + (-1)^n\right] \cos\frac{n\theta}{2} - \frac{n}{2}\cos\frac{(n-4)\theta}{2}\right\} \\ v_I = \sum_{n=1}^{\infty} \frac{r^{\frac{n}{2}}}{2\mu} a_n \left\{\left[\kappa - \frac{n}{2} - (-1)^n\right] \sin\frac{n\theta}{2} + \frac{n}{2}\sin\frac{(n-4)\theta}{2}\right\} \end{array}\right. \quad (1)$$

and

$$ModelII\left\{\begin{array}{l} u_{II} = -\sum_{n=1}^{\infty} \frac{r^{\frac{n}{2}}}{2\mu} b_n \left\{\left[K + \frac{n}{2} - (-1)^n\right] \sin\frac{n\theta}{2} - \frac{n}{2}\sin\frac{(n-4)\theta}{2}\right\} \\ v_{II} = \sum_{n=1}^{\infty} \frac{r^{\frac{n}{2}}}{2\mu} b_n \left\{\left[K - \frac{n}{2} + (-1)^n\right] \cos\frac{n\theta}{2} + \frac{n}{2}\cos\frac{(n-4)\theta}{2}\right\} \end{array}\right. \quad (2)$$

where $u_I$, $v_I$, $u_{II}$, and $v_{II}$ are horizontal and vertical displacements in mode I and mode II, respectively, $\mu$ is the shear modulus, $\kappa = (3 - \nu)/(1 + \nu)$ for plane stress and $\kappa = 3 - 4\nu$ for plane strain condition, $\upsilon$ is the Poisson's ratio, r and θ are polar coordinates with the crack-tip being the origin of coordinates, and a and b are constants.

Equations (1) and (2) can be rearranged as follow:

$$\begin{aligned} u = {} & \frac{K_I}{2\mu}\sqrt{\frac{r}{2\pi}}\cos\frac{\theta}{2}\left(\kappa - 1 + 2\sin^2\frac{\theta}{2}\right) \\ & + \frac{K_{II}}{2\mu}\sqrt{\frac{r}{2\pi}}\sin\frac{\theta}{2}\left(\kappa + 1 + 2\cos^2\frac{\theta}{2}\right) \\ & + \frac{T}{8\mu}r(\kappa + 1)\cos\theta \end{aligned} \quad (3)$$

$$\begin{aligned} v = {} & \frac{K_I}{2\mu}\sqrt{\frac{r}{2\pi}}\sin\frac{\theta}{2}\left(K + 1 - 2\cos^2\frac{\theta}{2}\right) \\ & - \frac{K_{II}}{2\mu}\sqrt{\frac{r}{2\pi}}\cos\frac{\theta}{2}\left(K - 1 - 2\cos^2\frac{\theta}{2}\right) \\ & + \frac{T}{8\mu}r(K - 3)\sin\theta \end{aligned} \quad (4)$$

by using

$$K_I = a_1\sqrt{2\pi}, K_{II} = -b_1\sqrt{2\pi}, T = 4a_2 \quad (5)$$

where $K_I$ and $K_{II}$ represent the mode I and II of SIF, respectively, and T stands for T-stress.

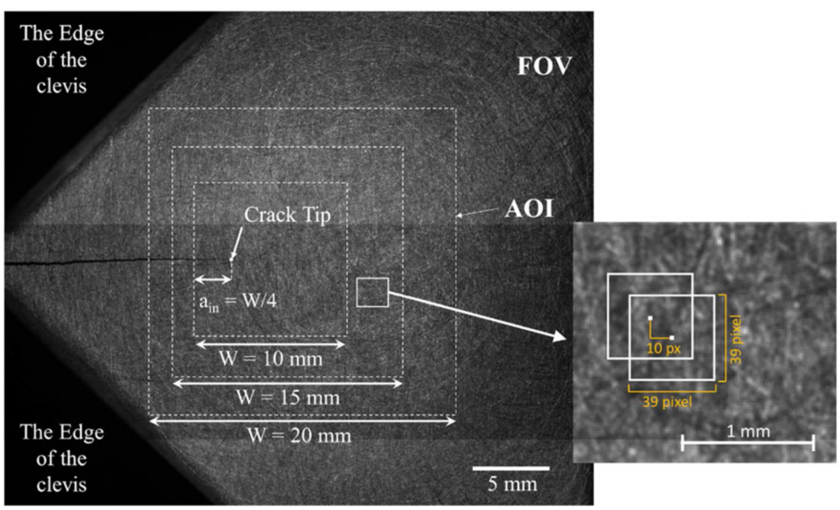


**FIGURE 4** The size and position of AOIs in the FOV of 36 × 32 mm$^2$ [Colour figure can be viewed at wileyonlinelibrary.com]

The SIF evaluated experimentally ($\Delta K_{exp}$) was compared with the nominal solution ($\Delta K_{nom}$).[49] To quantify the difference, the parameter of δ was defined as follows:

$$\delta = \left| \frac{\Delta K_{\mathrm{exp}} - \Delta K_{\mathrm{nom}}}{\Delta K_{\mathrm{nom}}} \right| \times 100. \tag{6}$$

Displacement data were collected from 3 different area of interests (AOI) including 10 × 10, 15 × 15, and 20 × 20 mm$^2$ which contain 15620, 8740, and 3900 data points, respectively. The position of the AOI in the FOV was selected in a way that the crack tip was located at the one-fourth of the width of the AOI (Figure 4). The data points located at the plastic zone are also considered in the SIF evaluations as suggested previously.[43] The crack growth during the test was considered in the calculation of nominal SIF.

## 3 | RESULTS AND DISCUSSION

Figure 5 illustrates the effect of considering a different number of terms in Williams' solution in the displacement data around the crack tip. Figure 5 is useful as a qualitative way to visualise the uncertainty in the fitting of experimental to analytical displacement data. In Figure 5, the smooth lines represent the analytical displacements, and the serrated lines represent the experimental displacements. It can be seen that considering just 1 or 2 terms of Williams' series in the solution led to a weak fitting with

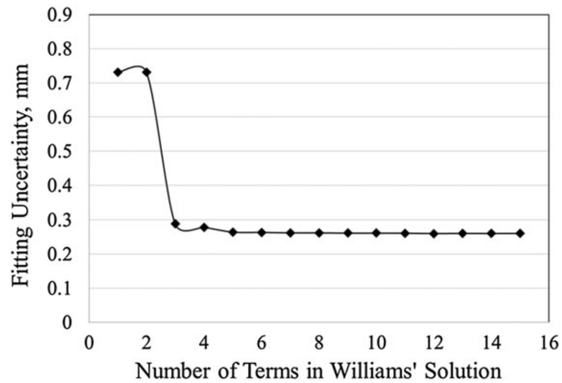


**FIGURE 6** Evolution of the quality of fitting displacement data as a function of number of Williams' terms, $\Delta K_{nom} = 20$ MPa$\sqrt{\mathrm{m}}$, AOI = 20 × 20 mm$^2$

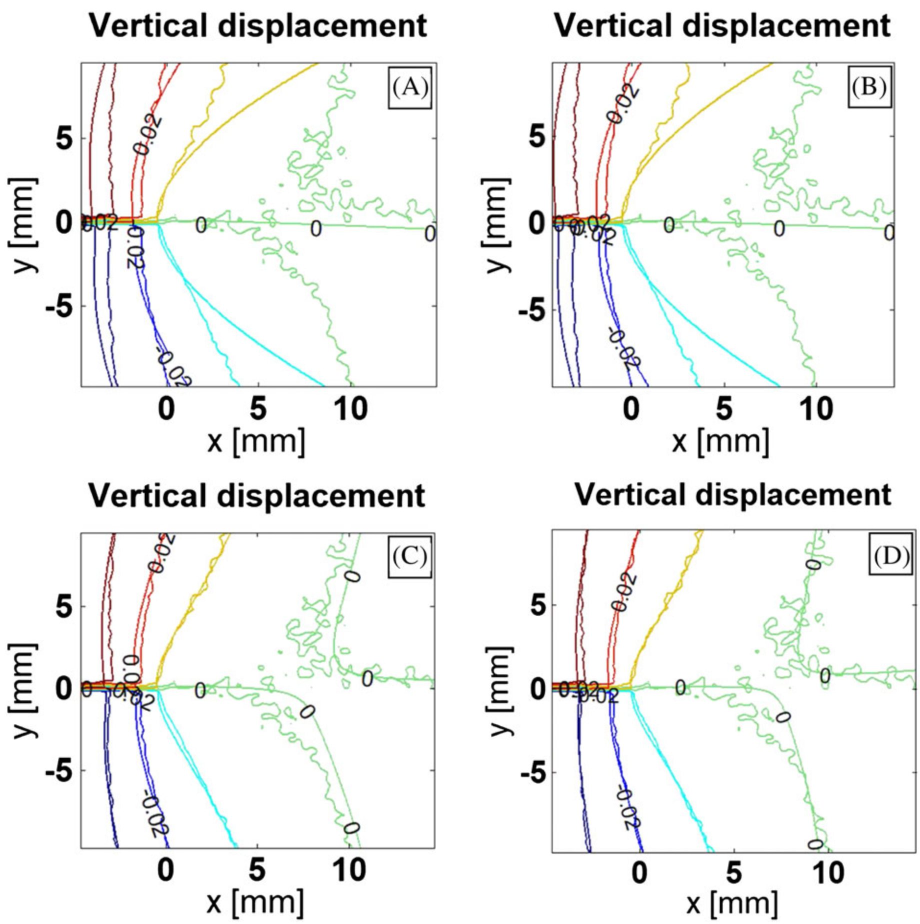


**FIGURE 5** The quality of fitting the experimental displacement field to William's solution by solving A, 1 term, B, 2 terms, C, 3 terms, and D, 7 terms when $\Delta K_{nom} = 20$ MPa$\sqrt{\mathrm{m}}$ and AOI = 20 × 20 mm$^2$ [Colour figure can be viewed at wileyonlinelibrary.com]

high uncertainty (Figure 5A,B).[31] The third term improves the fitting quality considerably (Figure 5C). At the seventh term, the fitting to the data points far from the crack tip is only slightly improved (Figure 5D). To quantify the quality of the fitting process, the difference between the value of the experimental data points and those evaluated by Williams' solution is calculated as the fitting-uncertainty. Figure 6 shows the behaviour of fitting uncertainty by increasing the solved number of terms in Williams' series when AOI = 20 × 20 $mm^2$ and $\Delta K_{nom}$ = 20 MPa$\sqrt{}$m. It can be seen that by increasing the number of terms the fitting uncertainty converges to a certain value. No further improvement in the fitting can be observed by considering more than 5 terms. Similar behaviour was observed for other loading conditions. It is consistent with published works[34,50,51] suggesting more number of terms should be used in Williams' expansion to obtain the convergence in the estimated SIF when a large AOI is selected. Therefore, in this work, 5 terms in Williams' expansion were used to describe the crack tip field.

In order to evaluate the ability of the proposed method to be used for in-service applications, continuous monitoring of the SIF is studied. The evolution of the SIF during 2 cycles is shown in Figure 7 for 3 different

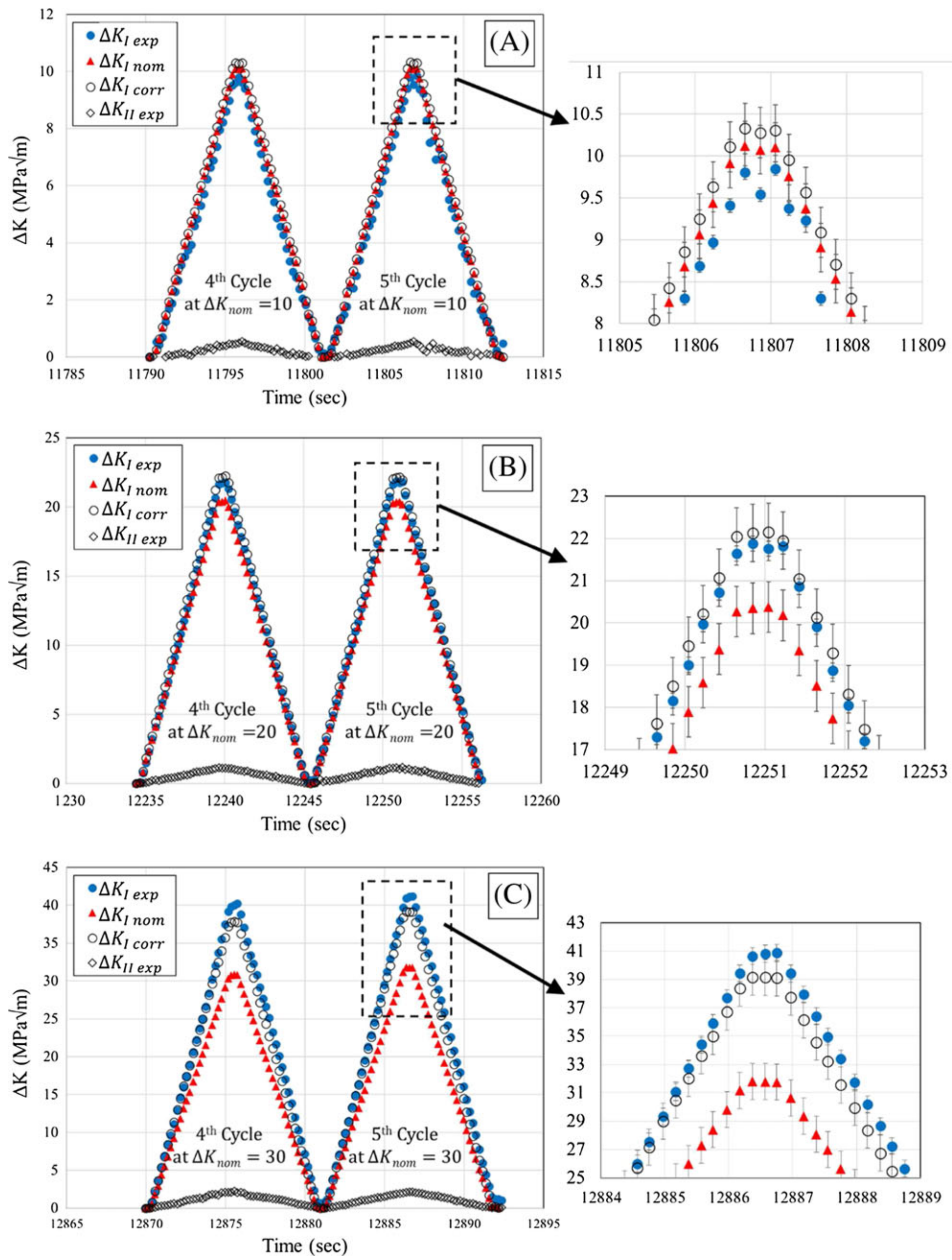


**FIGURE 7** Continuous evaluation of A, ΔK at $\Delta K_{nom}$ = 10 MPa$\sqrt{}$m, B, $\Delta K_{nom}$ = 20 MPa$\sqrt{}$m, and C, $\Delta K_{nom}$ = 30 MPa$\sqrt{}$m [Colour figure can be viewed at wileyonlinelibrary.com]

loading levels ($\Delta K = 10$, 20, and 30 $MPa\sqrt{m}$). The error bars shown in Figure 7 account for the error related to the estimation of the crack tip position. It can be seen that at low loads ($\Delta K = 10\ MPa\sqrt{m}$), the nominal and experimental $\Delta K$ agree well. For higher loads (Figure 7 B,C), the experimental $\Delta K$ always overestimates the nominal values ($\Delta K_{nom}$). For example, when $\Delta K_{nom} = 20\ MPa\sqrt{m}$, the $\Delta K_{exp}$ evaluated the higher value of 21.6 $MPa\sqrt{m}$. The difference becomes more significant for higher loads. For example, for $\Delta K_{nom} = 30\ MPa\sqrt{m}$, the experimental $\Delta K$ is equal to 40.8 $MPa\sqrt{m}$, that is 36% higher than $\Delta K_{nom}$. This behaviour can be attributed to the development of the plastically deformed zone at the crack tip. It has been stated that by extending the crack tip plastic zone, the crack behaves like a crack with larger length.[52] Consequently, the displacement field around the crack tip can be affected by enlarging the crack tip plastic zone. To compensate the effect of plasticity at the nominally evaluated SIF, Irwin's approach[53] was used. To this end, the crack tip was located at the centre of the plastic zone. In other words, the crack length was computed as the sum of crack length (a) and the plastic zone ($r_y$):

$$a_{corr} = a + r_y \tag{7}$$

where

$$r_y = \frac{1}{2\pi}\left(\frac{K_I}{\sigma_{ys}}\right)^2. \tag{8}$$

Accordingly, the nominal SIF was recalculated by replacing the crack length with the corrected crack length ($a_{corr}$).[52,54] It should be mentioned that both of theoretical and experimental methods used in this experiment were based on LEFM. Therefore, the Small Scale Yielding (SSY) condition should be met. Based on ASTM E 647,[41] for the geometry of this specimen and the crack length (a = 26.14 mm at the end of cyclic loading), the maximum SIF ($K_{max}$) which can be applied to the sample in SSY condition is 44.35 $MPa\sqrt{m}$. Considering the load ratio of 0.3 in this experiment, the maximum SIF range is 31.04 $MPa\sqrt{m}$.

Figure 7 shows that experimental estimations corrected with the plastic zone size significantly reduce the difference between experimental and nominal $\Delta K$ from 10.8 $MPa\sqrt{m}$ to 1.7 $MPa\sqrt{m}$ at $\Delta K_{nom} = 30\ MPa\sqrt{m}$. It is worth noting the small crack growth (0.06 mm) taking place between cycles at $\Delta K_{nom} = 30\ MPa\sqrt{m}$ (Figure 7C). The crack growth for individual cycles was negligible for lower loads.

The expected value of $\Delta K_{II}$ is zero because the CT geometry allows only opening mode load to be nominally applied. However, as it can be seen in Figure 6, the experimentally estimated $\Delta K_{II}$ is 0.5, 0.9, and 1.9 $MPa\sqrt{m}$ for $\Delta K$ applied of 10, 20, and 30 $MPa\sqrt{m}$, respectively. Similar behaviour was previously observed and was attributed to local deviation of the growing crack which can induce some mixed-mode component.[55] This mechanism is often referred to as wedging effect. In addition, the presence of a local mode II component at the crack tip is obscured by the poor signal to noise ratio in the horizontal displacements that in CT samples are typically one-third of an order of magnitude of the vertical displacements.

The effect of collecting data points from different AOI sizes on the δ is shown in Figure 8. It can be seen that the value of δ has been confined to less than 10% for applied $\Delta K$ up to 15 $MPa\sqrt{m}$. However, the difference between the theoretical and the experimental $\Delta K_I$ for AOI = $20 \times 20\ mm^2$ increases from 5 to 24.5% when $\Delta K$ increases from 15 to 30 $MPa\sqrt{m}$. Similar behaviour can be seen in Figure 8 for the different AOIs studied, with AOI = 10 mm having the steepest increase with growing $\Delta K$.

Figure 8 shows how crack length correction can significantly improve the accuracy of the nominal SIF evaluation for higher loads, while it has a negligible effect at low $\Delta K$. For example, for $\Delta K = 30\ MPa\sqrt{m}$, the value of δ is reduced by 24.6%, 23.6%, and 23.2% for AOIs of $10 \times 10$, $15 \times 15$, and $20 \times 20\ mm^2$, respectively. The plasticity correction has reduced the value of δ at AOI = $20 \times 20\ mm^2$ by 7.9%, 14.9%, and 23.2% for applied $\Delta K$ of 20, 25, and 30 $MPa\sqrt{m}$, respectively. The higher value of δ at $\Delta K = 10\ MPa\sqrt{m}$ rather $\Delta K = 15\ MPa\sqrt{m}$ can be attributed to the poorer noise to signal ratio at lower applied loads.

Figure 9 shows the evolution of SIFs as a function of the applied load during the last loading segment, leading to the fracture of the sample. It can be observed that by increasing the load, the difference between the experimental and nominal SIF becomes more significant. The

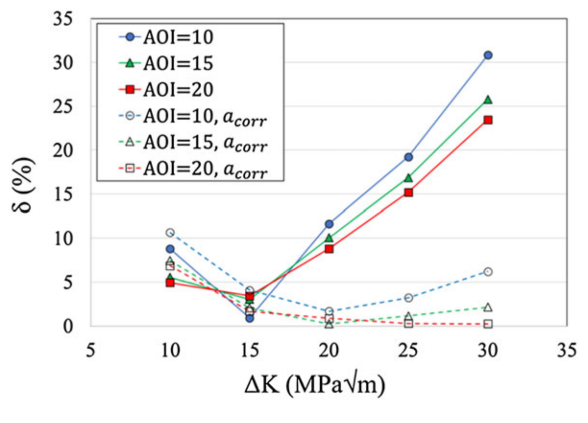


**FIGURE 8** Evolution of δ by increasing $\Delta K_{nom}$ for different sizes of AOI in mm [Colour figure can be viewed at wileyonlinelibrary.com]

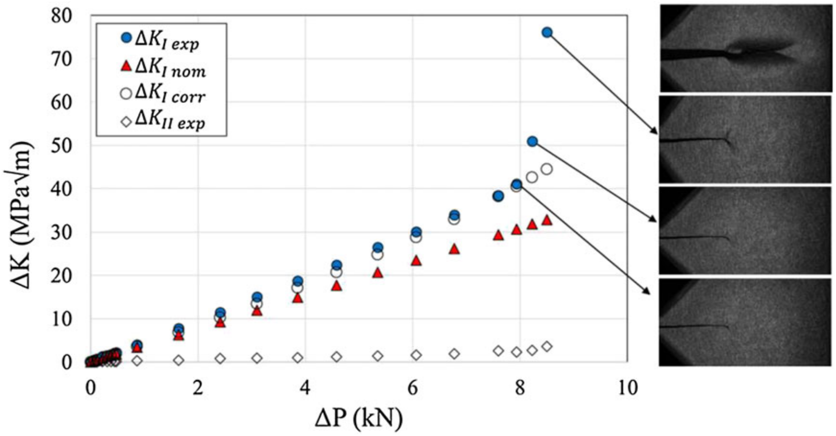


**FIGURE 9** Continuous evaluation of ΔK as a function of applied load at the last loading segment, leading to sudden fracture of the sample [Colour figure can be viewed at wileyonlinelibrary.com]

graph in Figure 9 shows a very good fit between $\Delta K_{exp}$ and $\Delta K_{corr}$ up to the $\Delta K \approx 42$ MPa$\sqrt{m}$ where there is a linear relation between SIF and load range (ΔP). Thereafter, $\Delta K_{exp}$ surges upward while $\Delta K_{nom}$ keeps increasing linearly. It worth noting that SSY condition has not met at ΔK larger than 31 MPa$\sqrt{m}$. Monitoring the crack on the surface of the sample showed that beyond ~42 MPa$\sqrt{m}$ the crack started to grow during the loading segment of the cyclic load. Photographs of the sample corresponding to the final SIF measurement are also shown in Figure 9. Sudden fracture happened just after the last measurement point (top-right photograph in Figure 9). Considering the load ratio of 0.3, at the deviation point, the $K_{max}$ is approximately 55 MPa$\sqrt{m}$ ($\Delta K \approx 42$ MPa$\sqrt{m}$). It is interesting that this value is in good agreement with the estimated $K_c$ by Newman et al[56] for a sample with similar geometry and thickness. This suggests that the point at which ΔK deviates from the linear behaviour can be used to estimate the critical SIF for this thickness. Additional experiments with larger specimens would need to be conducted to investigate this point. For the cases where the surface does not represent the complete material behaviour, probing the bulk of the material[57] and comparing it with the surface DIC results will shed light on the mechanisms taking place through the thickness. In the presence of high crack tip plasticity when SSY is not met, one can measure the J parameter. The experiments shown here suggest that current approach can be used not only for SIF monitoring while applying cyclic loads, but also as a rough estimation of the critical of SIF ($K_c$). The measured critical SIF measured here (12-mm thickness) is approximately 9 MPa$\sqrt{m}$ higher than the fracture toughness of this material.[58] Such difference is within the scatter normally observed in fracture toughness measurements. In addition, a portion of such difference is probably due to our experiment not being conducted under plan strain conditions. The recommended thickness for fracture toughness measurement in CT geometry is half of the width of the specimen (B/W = 0.5 where B is the thickness of the specimen),[59] while in our experiment this value is equal to 0.25.

## 4 | CONCLUSIONS

A set of experiments has been conducted to monitor the evolution of SIF under cyclic loading at 5 different load levels and final fracture on a CT specimen made of 2024-T351 aluminium alloy. A hybrid methodology has been employed to evaluate the SIF from experimentally evaluated displacement data around the crack tip. The results showed that the Irwin's approach that modifies the crack length to account for crack tip plasticity improves noticeably the SIF estimations. Continuous measurement of the SIF at the final loading stage to fracture of the sample showed a deviation from the linear relation between the load and the experimental SIF. Based on a previous work, this deviation might be related to the critical SIF for the thickness studied. The SSY condition was not met at load close to the fracture of the specimen. Because either the experimental method or corrected theoretical method are based on LEFM, the validity of the results in this range should be assessed with a parameter like J-integral. Nevertheless, further research is currently in progress to better understand the physics behind such deviation.

## ACKNOWLEDGEMENTS

The authors wish to acknowledge the financial support of the University of Malaga through Campus de Excelencia Internacional del Mar (CEIMAR) and Ministerio de Economia y Competitividad through grant reference MAT2016-76951-C2-2-P.

## ORCID

*M. Mokhtarishirazabad* http://orcid.org/0000-0002-5035-0397
*P. Lopez-Crespo* http://orcid.org/0000-0002-5897-5615

## REFERENCES

1. Purushothaman S, Panayotou NF, Tien JK. Synchrotron radiation microradiography of cracks in aluminum alloys. *Metall Trans A*. 1980;11A:621-625.
2. Ritchie RO, Garrett GG, Knott JF. Crack-growth monitoring: optimisation of the electrical potential technique using an analogue method. *Int J Fract Mech*. 1971;7:462-467.
3. Gandossi L, Summers SA, Taylor NG, Hurst RC, Hulm BJ, Parker JD. The potential drop method for monitoring crack growth in real components subjected to combined fatigue and creep conditions: application of FE techniques for deriving calibration curves. *Int J Press Vessels Pip*. 2001;78(11-12):881-891.
4. Neale BK, Priest RH. On the unloading compliance method for crack length measurement. *Eng Fract Mech*. 1984;19(3):441-448.
5. Wagner D, Ranc N, Bathias C, Paris PC. Fatigue crack initiation detection by an infrared thermography method. *Fatigue Fract Eng Mater Struct*. 2009;33:12-21.
6. Maslouhi A. Fatigue crack growth monitoring in aluminum using acoustic emission and acousto-ultrasonic methods. *Struct Control Health Monit*. 2011;18(7):790-806.
7. Zilberstein V, Grundy D, Weiss V, et al. Early detection and monitoring of fatigue in high strength steels with MWM-arrays. *Int J Fatigue*. 2005;27(10-12):1644-1652.
8. Hamia R, Cordier C, Dolabdjian C. Eddy-current non-destructive testing system for the determination of crack orientation. *NDT and E Int*. 2014;61:24-28.
9. Nakazawa H, Hirano K. Ultrasonic monitoring techniques of crack growth and fracture mechanics evaluation of materials. *Jpn J Appl Phys*. 1984;23(S1):12-16.
10. ASTM E1685-13, Standard practice for measuring the change in length of fasteners using the ultrasonic pulse-echo technique, West Conshohocken, PA: ASTM International; 2013.
11. Cuadra J, Vanniamparambil PA, Hazeli K, Bartoli I, Kontsos AA. Hybrid optico-acoustic NDE approach for deformation and damage monitoring. In: Kag J, Jablonski D, Dudzinski D, eds. *Evaluation of Existing and New Sensor Technologies for Fatigue, Fracture and Mechanical Testing, STP 1584*. West Conshohocken,PA: ASTM International; 2015:135-146.
12. Vanniamparambil PA, Bartoli I, Hazeli K, et al. An integrated structural health monitoring approach for crack growth monitoring. *J Intell Mater Syst Struct*. 2012;23(14):1563-1573.
13. Whittaker VN. A review of non-destructive measurement of flaw size. *Non-Destr Test*. 1972;5(2):92-100.
14. Gao P, Wang C, Li Y, Cong Z. Electromagnetic and eddy current NDT in weld inspection: a review. *Insight: Non-Destructive Testing and Condition Monitoring*. 2015;43:337-345.
15. Scruby CB. An introduction to acoustic emission. *J Phys E: Sci Instrum*. 1987;20(8):946-953.
16. Ramesh K, Gupta S, Kelkar AA. Evaluation of stress field parameters in fracture mechanics by photoelasticity—revisited. *Eng Fract Mech*. 1997;56(1):25-45.
17. Diaz FA, Patterson EA, Tomlinson RA, Yates JR. Measuring stress intensity factors during fatigue crack growth using thermoelasticity. *Fatigue Fract Eng Mater Struct*. 2004;27(7):571-583.
18. Nowell D, De Matos PFP. Application of digital image correlation to the investigation of crack closure following overloads. *Procedia Eng*. 2010;2(1):1035-1043.
19. McNeill SR, Peters WH, Sutton MA. Estimation of stress intensity factor by digital image correlation. *Eng Fract Mech*. 1987;28(1):101-112.
20. Lopez-Crespo P, Mostafavi M, Steuwer A, Kelleher JF, Buslaps T, Withers PJ. Characterisation of overloads in fatigue by 2D strain mapping at the surface and in the bulk. *Fatigue Fract Eng Mater Struct*. 2016;39(8):1040-1048.
21. Yoneyama S, Kitagawa A, Iwata S, Tani K, Kikuta H. Bridge deflection measurement using digital image correlation. *Exp Tech*. 2007;31(1):34-40.
22. Sutton MA, Li N, Joy DC, Reynolds AP, Li X. Scanning electron microscopy for quantitative small and large deformation measurements part I: SEM imaging at magnifications from 200 to 10,000. *Exp Mech*. 2007;47(6):775-787.
23. Carroll JD, Abuzaid W, Lambros J, Sehitoglu H. High resolution digital image correlation measurements of strain accumulation in fatigue crack growth. *Int J Fatigue*. 2013;57:140-150.
24. Pan B, Yu L, Wu D. High-accuracy 2D digital image correlation measurements with bilateral telecentric lenses: error analysis and experimental verification. *Exp Mech*. 2013;53(9):1719-1733.
25. Pan B, Wang B. Digital image correlation with enhanced accuracy and efficiency: a comparison of two subpixel registration algorithms. *Exp Mech*. 2016;56(8):1395-1409.
26. Luo PF, Chao YJ, Sutton MA, Peters WH. Accurate measurement of three-dimensional deformations in deformable and rigid bodies using computer vision. *Exp Mech*. 1993;33(2):123-132.
27. Sutton MA, Mingqi C, Peters WH, Chao YJ, McNeill SR. Application of an optimized digital correlation method to planar deformation analysis. *Image Vis Comput*. 1986;4(3):143-150.
28. Sutton MA, Orteu JJ, Schreier H. *Image Correlation for Shape, Motion and Deformation Measurements: Basic Concepts, Theory and Applications*. New York: Springer Science & Business Media; 2009.
29. Sutton MA, Matta F, Rizos D, et al. Recent progress in digital image correlation: background and developments since the 2013 W M Murray lecture. *Exp Mech*. 2017;57(1):1-30.
30. Hamam R, Hild F, Roux S. Stress intensity factor gauging by digital image correlation: application in cyclic fatigue. *Strain*. 2007;43(3):181-192.
31. Yates JR, Zanganeh M, Tai YH. Quantifying crack tip displacement fields with DIC. *Eng Fract Mech*. 2010;77(11):2063-2076.
32. Díaz FA, Burguete RL, Patterson EA. Evaluation using digital image correlation of stress intensity factors in an aerospace panel. *Exp Mech*. 2011;51:45-57.

33. Lopez-Crespo P, Shterenlikht A, Yates JR, Patterson EA, Withers PJ. Some experimental observations on crack closure and crack-tip plasticity. *Fatigue Fract Eng Mater Struct*. 2009;32(5):418-429.

34. Yoneyama S, Ogawa T, Kobayashi Y. Evaluating mixed-mode stress intensity factors from full-field displacement fields obtained by optical methods. *Eng Fract Mech*. 2007;74(9):1399-1412.

35. Lopez-Crespo P, Shterenlikht A, Patterson EA, Withers PJ, Yates JR. The stress intensity of mixed mode cracks determined by digital image correlation. *J Strain Anal Eng Des*. 2008;43(8):769-780.

36. Zanganeh M, Lopez-Crespo P, Tai YH, Yates JR. Locating the crack tip using displacement field data: a comparative study. *Strain*. 2013;49(2):102-115.

37. Yoneyama S, Arikawa S, Kusayanagi S, Hazumi K. Evaluating J-integral from displacement fields measured by digital image correlation. *Strain*. 2014;50(2):147-160.

38. deMatos PFP, Nowell D. Experimental and numerical investigation of thickness effects in plasticity-induced fatigue crack closure. *Int J Fatigue*. 2009;31(11-12):1795-1804.

39. Díaz FV, Kaufmann GH, Armas AF, Galizzi GE. Optical measurement of the plastic zone size in a notched metal specimen subjected to low-cycle fatigue. *Opt Lasers Eng*. 2001;35(6):325-333.

40. Vasco-Olmo JM, James MN, Christopher CJ, Patterson EA, Díaz FA. Assessment of crack tip plastic zone size and shape and its influence on crack tip shielding. *Fatigue Fract Eng Mater Struct*. 2016;39(8):969-981.

41. ASTM E647-15, Standard Test Method for Measurement of Fatigue Crack Growth Rates. West Conshohocken, PA: 2015.

42. Chaves V. Ecological criteria for the selection of materials in fatigue. *Fatigue Fract Eng Mater Struct*. 2014;37(9):1034-1042.

43. Mokhtarishirazabad M, Lopez-Crespo P, Moreno B, Lopez-Moreno A, Zanganeh M. Evaluation of crack-tip fields from DIC data: a parametric study. *Int J Fatigue*. 2016;89:11-19.

44. Shterenlikht A, Díaz-Garrido FA, Lopez-Crespo P, Withers PJ, Patterson EA. Mixed mode (KI + KII) stress intensity factor measurement by electronic speckle pattern interferometry and image correlation. *Appl Mech Mater*. 2004;1-2:107-112.

45. Lopez-Crespo P, Burguete RL, Patterson EA, Shterenlikht A, Withers PJ, Yates JR. Study of a crack at a fastener hole by digital image correlation. *Exp Mech*. 2009;49(4):551-559.

46. Lopez-Crespo P, Moreno B, Lopez-Moreno A, Zapatero J. Characterisation of crack-tip fields in biaxial fatigue based on high-magnification image correlation and electro-spray technique. *Int J Fatigue*. 2015;71:17-25.

47. Sutton MA, Turner JL, Chao YJ, Bruck HA, Chae TL. Experimental investigations of three-dimensional effects near a crack tip using computer vision. *Int J Fract*. 1992;53:201-228.

48. Vic-2D V6 Reference Manual, Correlated Solutions Incorporated (C.S.Inc). n.d.

49. Murakami Y. *Stress Intensity Factors Handbook*. Oxford: Pergamon Press; 1987.

50. Shukla A, Dally JW. *Experimental Solid Mechanics*. Second ed. LLC: College House Enterprises; 2014.

51. Yoneyama S, Morimoto Y, Takashi M. Automatic evaluation of mixed-mode stress intensity factors utilizing digital image correlation. *Strain*. 2006;42(1):21-29.

52. Irwin GR. Linear fracture mechanics, fracture transition, and fracture control. *Eng Fract Mech*. 1968;1(2):241-257.

53. Irwin GR. Plastic zone near a crack and fracture toughness. Sagamore Ordnance Materials Conference, Syracuse University: 1961.

54. Heyer RH, McCabe DE. Crack growth resistance in plane-stress fracture testing. *Eng Fract Mech*. 1972;4(3):413-430.

55. Tong J, Yates JR, Brown MW. A model for sliding mode crack closure. Parts I and II. *Eng Fract Mech*. 1995;52(4):599-623.

56. Newman JC Jr. An evaluation of fracture analysis methods. In: Newman JC Jr, Loss FJ, eds. *ASTM STP 896, Philadelphia: American Society for Testing and Materials*; 1985:5-96.

57. Withers PJ, Lopez-Crespo P, Kyrieleis A, Hung Y-C. Evolution of crack-bridging and crack-tip driving force during the growth of a fatigue crack in a Ti/SiC composite. *Proc Roy Soc A, Math Phys Eng Sci*. 2012;468(2145):2722-2743.

58. Kaufman JG. *Fracture Resistance of Aluminum Alloys: Notch Toughness, Tear Resistance, and Fracture Toughness*. ASM International; 2001.

59. ASTM E1820 Standard test Method for measurement of fracture toughness. Annual book of ASTM Standard, vol. 03, West Conshohocken, PA 19428.: ASTM International; 2003.

**How to cite this article:** Mokhtarishirazabad M, Lopez-Crespo P, Zanganeh M. Stress intensity factor monitoring under cyclic loading by digital image correlation. *Fatigue Fract Eng Mater Struct*. 2018;41:2162–2171. https://doi.org/10.1111/ffe.12825

# Appendix III

Published Paper #3

**Title:** Optical and analytical investigation of overloads in biaxial fatigue cracks

**Authors:** M. Mokhtarishirazbad[1], P. Lopez-Crespo[1], B. Moreno[1], A. Lopez-Moreno[2], M. Zanganeh[3]

[1]Department of Civil and Materials Engineering, University of Malaga, C/Dr Ortiz Ramos s/n, 29071, Malaga, Spain

[2]Department of Materials Science and Metallurgy Engineering, University of Jaen, Campus Las Lagunillas, 23071, Jaen, Spain

[3]Jacobs Technology, NASA Johnson Space Center, Houston TX, USA

**Journal:** International Journal of Fatigue, Volume 100, Part 2, July 2017, Pages 583-590

Impact Factor: 3.132 , Q1 in JCR

International Journal of Fatigue 100 (2017) 583–590

Contents lists available at ScienceDirect

International Journal of Fatigue

journal homepage: www.elsevier.com/locate/ijfatigue

# Optical and analytical investigation of overloads in biaxial fatigue cracks

M. Mokhtarishirazabad [a], P. Lopez-Crespo [a,*], B. Moreno [a], A. Lopez-Moreno [b], M. Zanganeh [c]

[a] Department of Civil and Materials Engineering, University of Malaga, C/Dr Ortiz Ramos s/n, 29071 Malaga, Spain
[b] Department of Materials Science and Metallurgy Engineering, University of Jaen, Campus Las Lagunillas, 23071 Jaen, Spain
[c] Jacobs Technology, NASA Johnson Space Center, Houston TX, USA

ARTICLE INFO

*Article history:*
Received 24 October 2016
Received in revised form 22 December 2016
Accepted 23 December 2016
Available online 27 December 2016

*Keywords:*
Biaxial fatigue
Overload
St-52-3N steel
Digital image correlation

ABSTRACT

Structural components are often subjected to complex multiaxial loading conditions. The study of fatigue cracks under such conditions is not easy from an experimental point of view and most works tend to focus more on the simpler but less realistic case of uni-axial loading. Consequently, there are many uncertainties related to the load sequence effect that is now well known and is not normally incorporated into the growth models. The current work presents a new methodology for evaluating overload effect in biaxial fatigue cracks. The methodology includes evaluation of mixed-mode ($\Delta K_I$ and $\Delta K_{II}$) stress intensity factor and the Crack Opening Displacement for samples with and without overload cycle under biaxial loading. The methodology is tested under two different load levels and a range of crack lengths. All crack-tip information is obtained with a hybrid optical-analytical methodology. It combines experimental full-field digital image correlation data and Williams' elastic model describing the crack-tip field.



## 1. Introduction

Good estimation of fracture parameters is key to achieve reliable life predictions for mechanical components. A number of successful approaches have been presented for estimating experimentally essential fracture parameters such as stress intensity factor (SIF) experimentally [1]. Apart from the conventional standard test methods [2], it has been shown that crack-tip fields (strain, stress and displacement field) include essential information for accurate estimation of fracture parameters [3]. A number of different techniques are able to provide both surface and bulk information. Surface techniques include photo-elasticity [4], thermo-elasticity [5], Moiré interferometry [6] and digital image correlation (DIC) [7]. Bulk techniques include neutron diffraction [8] and X-ray diffraction [9]. Among all these full-field techniques, DIC has received enormous attention recently [10,11] because of its many advantages compared to other techniques [12]. Simplicity, accuracy and flexibility are the most prominent merits of DIC technique for calculating displacement fields [13]. While fracture problems can be simplified by considering mode I loading, cracks in structural materials are generally under mixed-mode loading condition [3]. Therefore, estimation of the fracture parameters based on mixed-mode loading condition will be more representative of the material fracture behaviour under the actual working condition. Different optical methods have been used for obtaining full-field information required for mixed-mode loading analysis previously. Sanford and Dally [14] have determined the mixed-mode SIFs by utilising isochromatic fringes near the crack-tip. They have reported that employing an over-deterministic approach on the data points provided by the full filed fringe patterns led to a highly accurate SIF estimation. Displacement fields derived by DIC technique have been utilised by Yoneyama et al. [15] to evaluate the mixed-mode SIFs of a polymer (polymethylmethacrylate). While they used a non-linear least square method for their solutions, Réthoré et al. [16] have developed a method based on the Lagrangian conservation law for mixed-mode SIFs estimations. A good agreement between analytical displacement fields generated based on the Muskhilishvili's complex function approach and the experimentally measured displacement fields (obtained by DIC) has been also reported by Lopez-Crespo et al. [17]. By fitting the analytical model and experimental data, they have determined mixed-mode SIFs for a crack in a fastener hole.

Some of these approaches based on full-field techniques have been applied to study the effect of overload on fatigue cracks. For example, DIC was used to study the effect of overload on CT specimens made of 6082 Al alloy [18]. Comparison of the opening load obtained by DIC and that obtained by strip-yield model was useful to understand the influence of the aspect ratio of the crack on the closure behaviour. Similar conclusions were drawn by employing a combination of DIC and Muskhelishvili's complex potential development on 316L austenitic steel [19]. Full-field photo-elasticity

* Corresponding author.
*E-mail address:* plopezcrespo@uma.es (P. Lopez-Crespo).

http://dx.doi.org/10.1016/j.ijfatigue.2016.12.035
0142-1123/

**Nomenclature**

| | |
|---|---|
| a | crack length |
| $a_n$, $b_n$ | coefficients in Williams' expansion |
| AOI | area of interest used for analysing data points inside a particular region within the field of view |
| COD | crack opening displacement |
| DIC | digital image correlation |
| $K_I$ | stress intensity factor in mode I |
| $P_{max}$, $P_{min}$ | maximum and minimum applied load in the fatigue test |
| $P_{op}$ | opening load |
| r | radial distance from the crack-tip |
| $R_a$ | axial load ratio (=$P_{min}/P_{max}$) |
| $R_t$ | torsional load ratio (=$T_{min}/T_{max}$) |
| T | T-stress, a constant stress parallel to the crack |
| u, v | horizontal and vertical displacement fields |
| $\Delta K_I$ | stress intensity factor range in mode I (=$K_{I\ max} - K_{I\ min}$) |
| $\Delta K_{II}$ | stress intensity factor range in mode II (=$K_{II\ max} - K_{II\ min}$) |
| $\Delta\sigma_{OL}$ | axial stress range during the overload |
| $\Delta\tau_{OL}$ | shear stress range during the overload |
| φ | angle between axial and shear stress amplitude (see Fig. 3) |
| κ | $\kappa = (3-\upsilon)/(1+\upsilon)$ for plane stress and $\kappa = 3-4\nu$ for plane strain condition |
| μ | shear modulus |
| ν | Poisson's ratio |
| σ | axial normal stress |
| τ | shear stress |
| $\sigma_y$ | yield strength |

combined with CJP model [20] was used to understand the distortion induced by an overload and its effect on the crack growth rate on CT polycarbonate specimens [21]. The same model was used with electronic speckle pattern interferometry data to quantify the overload (OL) effect on commercially pure titanium samples [22]. The change in elastic and plastic strain fields were evaluated with DIC and synchrotron X-ray diffraction [23]. The reduction in the growth rate was related to the compressive residual stress field induced by the OL. The reliability of full-field techniques for closure studies has been proven by comparing the experimental results with FE method and other modelling methods [24,25].

The combined effect of OL and biaxial loading has been studied by potential drop technique [26]. Potential drop technique was used together with FE modelling on CTS specimens made of 7075 Al alloy to study the influence of the loading direction of the OL. The retardation effect introduced by the OL was reduced as the shear component of the load was increased. No retardation effect was observed after applying a pure shear mode overload. Shanyavsky and Orlov conducted fractographic analysis to explore the effect of an overload on cruciform D16T Al alloy specimens [27]. They studied different biaxial loads and different load ratios with a travelling microscope and related the compressive loads along the crack front and the closure in the opening direction to the retardation. Simulation of the same problem allowed the effect of the plastic size parameters on the biaxial ratio to be quantified. In addition, a delayed retardation mechanism was identified and its origin was associated to the type of stress acting on the crack [27,28].

Full-field optical techniques are very advantageous compared to other more traditional techniques. They are very versatile and can be used to study a wide range of aspects related to the OL, including evaluation of the plastic region, changes in the stress field due to the OL or experimental estimation of fracture mechanics parameters. Nevertheless, as it is described previously, they have been mostly applied to the uniaxial problem. In reality, most mechanical components are subjected to complex loading conditions with varying magnitude and direction. Therefore, it is desirable to apply full-field optical techniques to more complex loading conditions. In the present paper, we use a comprehensive optical and analytical methodology to study overloads in fatigue cracks under biaxial loading. Most experimental information is extracted from full-field DIC data. Specimens with and without overloads are compared in terms of crack growth rate, crack opening displacement (COD) and stress intensity factor.

## 2. Material and methods

Crack propagation in a low carbon steel (St-52-3N) was studied. This alloy is commonly used in offshore platforms because of its good weldability and ductility [29]. In addition, it combines good fatigue resistance with low environmental impact for applications where no energy is consumed during the use phase of the component [30]. Table 1 shows the composition of the alloy. Fig. 1 illustrates the microstructure of the material observed by optical microscope which shows the ferrite and pearlite bands [31]. The mechanical properties of the alloy are given in Table 2. A schematic of the specimen geometry is shown in Fig. 2.

An MTS 809 servo-hydraulic loading rig coupled by a biaxial extensometer Epsilon 3550 was used to apply biaxial loads under stress control mode in a similar way to previous works [32,33]. In-phase cyclic sinus signal with axial load ratio of 0.1 ($R_a = 0.1$) and torsional load ratio of $-1$ ($R_t = -1$) was applied in air at room temperature. The ratio between axial and torsional strains was measured with angle φ defined in Fig. 3. The angle φ was set to 45° in all the experiments. A hole with a diameter of about 0.35 mm was drilled in the outer surface of the specimen in order to enforce the crack to nucleate inside the field of view (Fig. 4) [33]. It should be mentioned that crack initiation in samples S3 and S4 did not occur after 1 million cycles. Therefore, a 3-step load decreasing method was employed as in [34]. Loading condition in the last step was set to be equal to the rest of the test (Table 3). The initial crack length used for crack growth measurements in samples S3 and S4 was around 550 μm. In this table, $\Delta\sigma = \sigma_{max} - \sigma_{min}$ and $\Delta\tau = \tau_{max} - \tau_{min}$. The crack length was evaluated from the crack-tip position with optical microscopy. The accuracy for locating the crack-tip was different in the crack growth direction and in the crack opening direction. The accuracy in locating the crack tip for the first time was estimated to be ±4.35 μm and ±2.17 μm in the crack growing and crack opening directions respectively. Once the initial crack tip is found, the accuracy between two successive measurements was ±1.45 μm. The related average error in measuring the crack growth rate was 0.002 μm/cycle.

In order to study the effect of the overload on the crack propagation behaviour, single overload cycle ($\Delta\sigma_{OL}, \Delta\tau_{OL}$) was applied on specimens on the half of the final crack length with the axial and torsional load ratio of 0.1 and $-1$, respectively. Tests were performed under two different baseline loads. Single overload cycles of 40% and 100% were applied on S2 and S4 samples respectively. That is, the load range in the overload cycle ($\Delta\sigma_{OL}, \Delta\tau_{OL}$) was 1.4

**Table 1**
Chemical composition in weight % of St-52-3N steel. The balance is Fe.

| C | Si | Mn | P | S | Cr | Ni | Mo |
|---|---|---|---|---|---|---|---|
| 0.17 | 0.22 | 1.23 | 0.01 | >0.0001 | 0.07 | 0.06 | 0.16 |

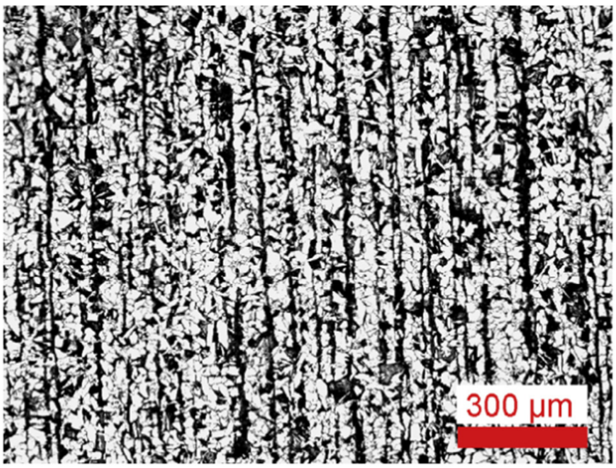


**Fig. 1.** The microstructure of St52-3N steel. Black and white vertical bands are showing the pearlite and ferrite bands, respectively [31].

**Table 2**
Monotonic properties of St-52-3N steel.

| | |
|---|---|
| Yield stress, $\sigma_y$ | 386 MPa |
| Ultimate tensile stress, $\sigma_u$ | 639 MPa |
| Young's modulus, E | 206 GPa |
| Shear Modulus | 78 GPa |

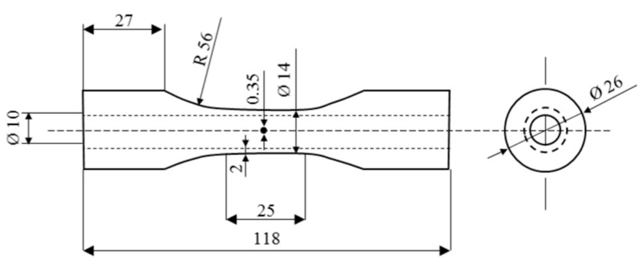


**Fig. 2.** The geometry of the hollow cylinder specimen with a central hole. All dimensions are in mm.

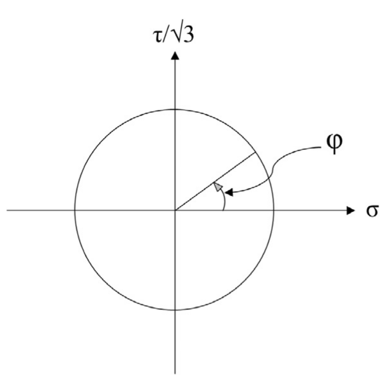


**Fig. 3.** Definition of angle between axial and shear stress amplitude.

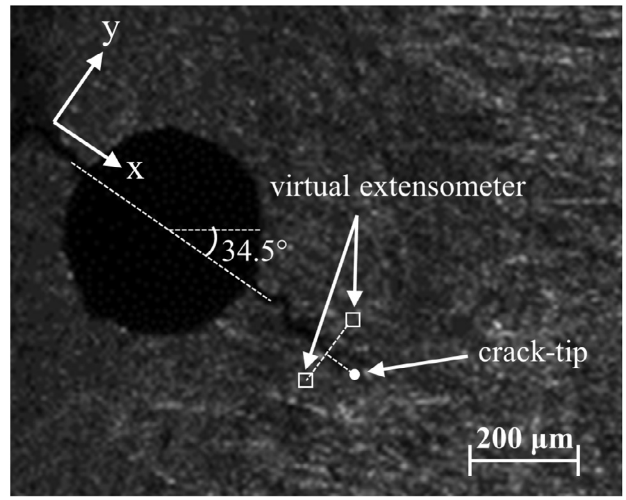


**Fig. 4.** The position of virtual extensometers for COD examination. The white bold mark shows the crack-tip position.

and 2 times larger than load range during the rest of the test ($\Delta\sigma$, $\Delta\tau$) for S2 and S4 samples, respectively. The cyclic loading then continued until the crack length reached about 1.45 mm. The secant method recommended in ASTM standard [35] has been employed to examine the rate of the fatigue crack growth. Table 3 shows the loading condition for samples with and without overload.

In addition, to evaluate the closure level, near tip crack opening displacement was measured by DIC [19,36]. To this end a virtual extensometer was placed 60 μm behind the crack-tip to measure the displacement in the crack opening direction [37]. Fig. 4 shows the positions of the virtual extensometer and crack initiation angle for S2 sample as an example.

### 2.1. Fatigue crack growth

The effect of single overload was studied by observing the evolution of the crack length versus the number of cycles. Fig. 5 shows how applying a single overload cycle can affect the crack growth behaviour for two different baseline loads. The test was stopped when the crack length was ~1.5 mm for all samples. Fig. 5a shows that high loads produced lives of 58,000 and 66,000 cycles for the specimens with no OL (S1) and with OL (S2), respectively. Fig. 5b shows that low loads produced lives of 136,000 and 138,000 cycles for the specimens with no OL (S3) and with OL (S4), respectively. It is clear that the increase in fatigue life due to OL is greater in the high baseline load. While retardation in the crack growth is observed right after the application of a 40% overload in sample S2 (Fig. 5a), a static jump of 58 μm in the crack length followed by a delayed retardation was observed after the 100% overload on sample S4 (Fig. 5b). Carlson et al. [38] argued that the fracture during the overload cycle or a few cycles afterwards of the stretched region located just ahead of the crack-tip can result in disappearing the delayed retardation period. This can rationalise the absence of the delayed retardation in sample S2 which was under higher baseline loads and the existence of the delayed retardation in S4. Delays of ~8000 and ~2000 cycles were observed at

**Table 3**
Axial and shear stress values for specimens with and without overload cycle.

| Specimen | Crack length at OL (μm) | Δσ (MPa) | Δτ (MPa) | $\Delta\sigma_{OL}$ (MPa) | $\Delta\tau_{OL}$ (MPa) |
|---|---|---|---|---|---|
| S1 | – | 216 | 277 | – | – |
| S2 | 669 | 216 | 277 | 302.4 | 388 |
| S3 | – | 162 | 230 | – | – |
| S4 | 689 | 162 | 230 | 324 | 460 |

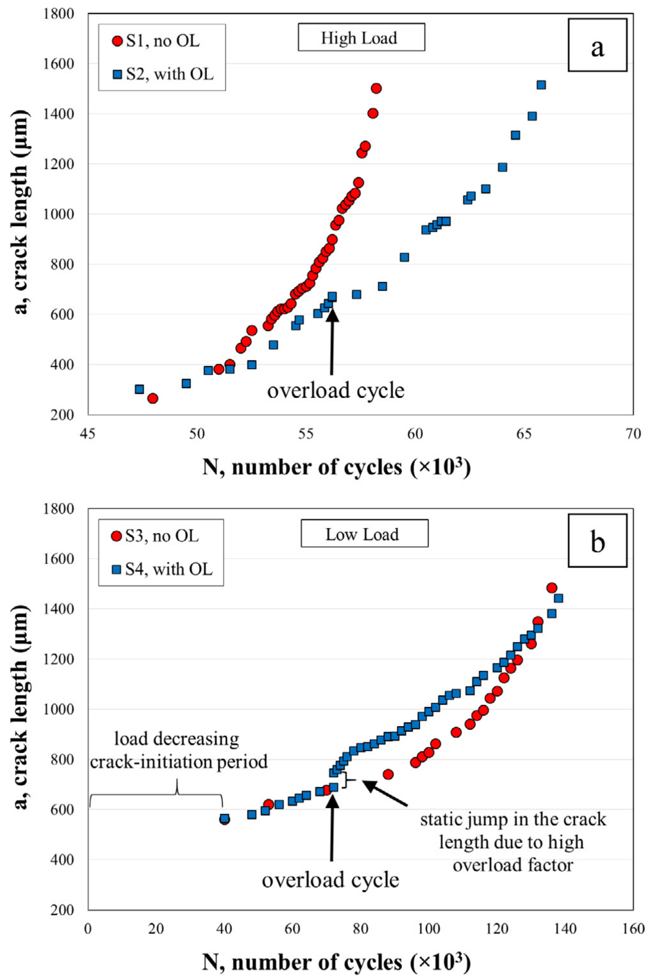


**Fig. 5.** Evolution of crack length versus number of cycles for samples with and without overload cycle, (a) samples S1 and S2 under higher cyclic loads, (b) samples S3 and S4 under lower cyclic loads.

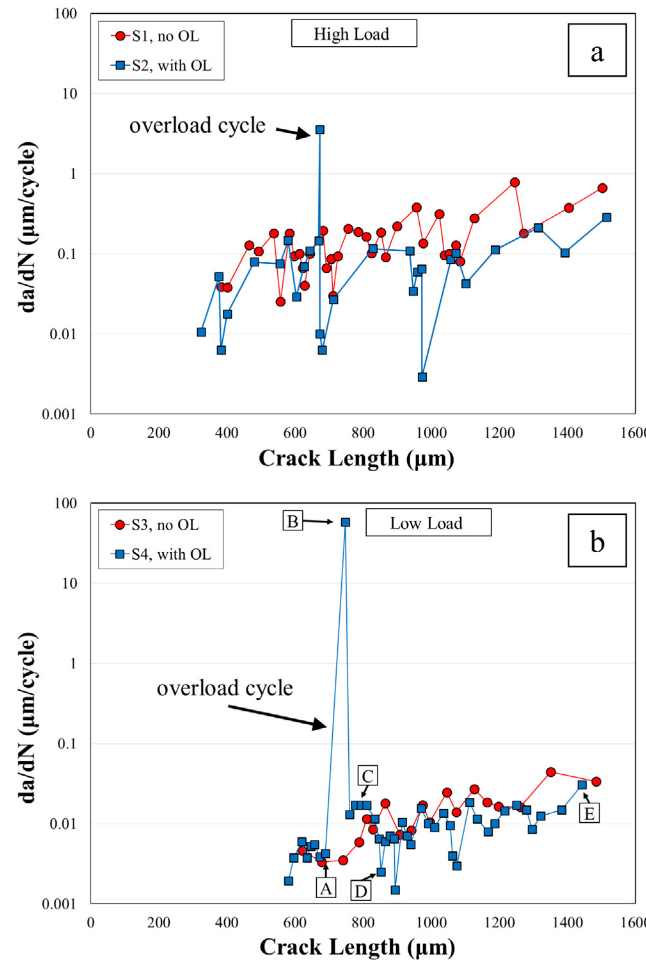


**Fig. 6.** Crack growth rate as a function of the crack length for high (a) and low (b) baseline cyclic load.

the end of the test for samples S2 and S4 respectively, as compared to the non-overload condition.

The crack growth rate is plotted as a function of crack length in Fig. 6. The overall higher da/dN values in Fig. 6a than in Fig. 6b indicate that growth rates observed in high load tests are on average 8 times faster than rates in low load tests. It is worth noting the logarithmic scale in the vertical axes in Fig. 6. The observed oscillation in this graph can be attributed to a combination of experimental error and the effect of microstructural barriers [31]. As it was mentioned previously, the microstructure of this alloy is made of ferrite and pearlite bands. Pearlite bands have a greater resistance due to higher percentage of carbon and can act as microstructural barrier [39].

The general regimes of crack growth rate after overload are acceleration, retardation and recovery [38]. Acceleration in crack growth rate just after the overload has been attributed to the crack-tip stretching which can lead to an increase in the effective stress intensity range [38].

Samples S2 and S4 exhibited different post-overload behaviour. After applying the overload cycle on S4, the growth rate did not decrease suddenly as expected [26]. Instead, the growth rate decreased gradually (from point B to point D in Fig. 6b). This phenomenon is normally referred to as delayed retardation [26,27,38,40] and lasted until the crack length was 0.890 mm. While the drop between acceleration and retardation occurred over a crack growth of 7 μm on S2, the drop required a 147 μm growth on S4 (between point C and point D in Fig. 6b). Shanyavsky and Orlov observed a very similar trend [27]. They suggested that while shear stress in mode III is the dominant fracture process on the specimen surface right after an overload cycle, subsequent crack growth acceleration (point D to E in Fig. 6b) is due to crack propagation in the interior by mode I opening. The difference between the OL condition and the non-OL condition is larger for high loads. That is, after the OL cycle, the difference between S1 and S2 in Fig. 6a is greater than the differences between S3 and S4 in Fig. 6b, even though the OL factor in S2 was smaller than the OL factor in S4. By the end of the test, there are still noticeable differences for the low loads (Fig. 6a). For the high baseline loads, the differences are smaller. The end of the retardation stage occurs when the OL growth rate curve meets the no-OL curve. Thus, by the end of the test sample S2 seems to be still in the retardation stage (Fig. 6a) and sample S4 seems to be coming out of the retardation stage (Fig. 6b). This is probably caused by the retardation induced in S2 being more pronounced than the retardation in S4.

### 2.2. Processing of displacement information

Crack-tip displacement data was measured by DIC. The obtained displacement data was then fitted into Williams' series [41,42]:

$$\text{Mode I}\left\{\begin{aligned} u_I &= \sum_{n=1}^{\infty} \frac{r^{\frac{n}{2}}}{2\mu} a_n \left\{ \left[\kappa + \tfrac{n}{2} + (-1)^n\right] \cos\tfrac{n\theta}{2} - \tfrac{n}{2}\cos\tfrac{(n-4)\theta}{2} \right\} \\ v_I &= \sum_{n=1}^{\infty} \frac{r^{\frac{n}{2}}}{2\mu} a_n \left\{ \left[\kappa - \tfrac{n}{2} - (-1)^n\right] \sin\tfrac{n\theta}{2} + \tfrac{n}{2}\sin\tfrac{(n-4)\theta}{2} \right\} \end{aligned}\right\} \tag{1}$$

and

$$\text{Mode II}\left\{\begin{aligned} u_{II} &= -\sum_{n=1}^{\infty} \frac{r^{\frac{n}{2}}}{2\mu} b_n \left\{ \left[\kappa + \tfrac{n}{2} - (-1)^n\right] \sin\tfrac{n\theta}{2} - \tfrac{n}{2}\sin\tfrac{(n-4)\theta}{2} \right\} \\ v_{II} &= \sum_{n=1}^{\infty} \frac{r^{\frac{n}{2}}}{2\mu} b_n \left\{ \left[\kappa - \tfrac{n}{2} + (-1)^n\right] \cos\tfrac{n\theta}{2} + \tfrac{n}{2}\cos\tfrac{(n-4)\theta}{2} \right\} \end{aligned}\right\} \tag{2}$$

where $u_I$ and $v_I$ are horizontal and vertical displacements in mode I respectively, $u_{II}$ and $v_{II}$ are horizontal and vertical displacements in mode II respectively, $\mu$ is the shear modulus, $\kappa = (3 - \nu)/(1 + \nu)$ for plane stress and $\kappa = 3 - 4\nu$ for plane strain condition, $\upsilon$ is the Poisson's ratio, r and θ are polar coordinates with the crack-tip being the origin of coordinates, and a and b are constants.

Eqs. (1) and (2) can be written in terms of the SIFs as follows:

$$u = \frac{K_I}{2\mu}\sqrt{\frac{r}{2\pi}}\cos\frac{\theta}{2}\left(\kappa - 1 + 2\sin^2\frac{\theta}{2}\right) + \frac{K_{II}}{2\mu}\sqrt{\frac{r}{2\pi}} \times \sin\frac{\theta}{2}\left(\kappa + 1 + 2\cos^2\frac{\theta}{2}\right) + \frac{T}{8\mu}r(\kappa+1)\cos\theta \tag{3}$$

$$v = \frac{K_I}{2\mu}\sqrt{\frac{r}{2\pi}}\sin\frac{\theta}{2}\left(\kappa + 1 - 2\cos^2\frac{\theta}{2}\right) - \frac{K_{II}}{2\mu}\sqrt{\frac{r}{2\pi}} \times \cos\frac{\theta}{2}\left(\kappa - 1 - 2\cos^2\frac{\theta}{2}\right) + \frac{T}{8\mu}r(\kappa-3)\sin\theta \tag{4}$$

by using

$$K_I = a_1\sqrt{2\pi}, \quad K_{II} = -b_1\sqrt{2\pi}, \quad T = 4a_2 \tag{5}$$

where $K_I$ and $K_{II}$ are the mode I and II of SIF respectively and T represents T-stress.

In order to improve the quality of the SIF estimations, the recommendations given in [43] were followed. Accordingly, a high order interpolation scheme of optimized 8-tap spline was used for DIC analysis to achieve sub-pixel accuracy. The zero-normalized sum of squared differences was set as the correlation criterion in order to vanish the effect of offset and scale in lighting [13]. The subset size was adjusted to 31 × 31 pixels. In addition, just 25% of the crack line was considered in the area of interest (the area where the displacement data were measured by DIC). The relative error in the estimated displacement (and consequently in COD) was 2.95%. This relative error was estimated from the quality of the correlation of the images taken at different loads. By taking to account the size of the area of interest ($0.4 \times 0.4\ mm^2$), two terms in the Williams' solution were used as suggested in [43]. Neglecting T-stress which appears at the second term of Williams' series can also induce a significant error in SIFs calculations in short crack length examinations [3].

In order to extract the vertical and the horizontal displacements with respect the axial loading axis, captured images have been rotated so that the crack appears horizontal in all images. Fig. 7 illustrates the vertical displacement contour for an area of interest around a crack with a length of 0.689 mm (sample S2)[1]. The images were rotated 37° clockwise so that the crack line was horizontal [44]. Displacement data points inside an area of $0.4 \times 0.4\ mm^2$ were extracted and fitted to Williams' solution in order to calculate SIFs.

The crack opening displacement, COD was also evaluated from the DIC data. A post processing routine was developed to measure the COD with a virtual extensometer as follows:

$$COD(x) = v_{bot} - v_{top} \tag{6}$$

where u and v are the horizontal and vertical displacement respectively, and x is the distance of the extensometer behind the crack-tip (here x = 60 μm). The subscripts "top" and "bot" refer to the position of the virtual extensometer points relative to the crack line. The compliance based algorithm proposed by Skorupa et al. [45] has been utilised to study the fatigue crack closure in this paper. This method includes six main steps: 1. Smoothing the data 2. Converting the smoothed data into a "loop data" 3. Data re-discretization in order to obtain a uniform spaced data points 4. Rotating the unload branch by 180 degrees and 6. Determination of closure parameters by finding the overlap between the loading branch with 25% of the upper part of the rotated unloading branch. The inflection point along the loading portion of the cycle is used to estimate the opening load ($P_{op}$). This method has been used by other authors for characterising fatigue crack closure using local compliance measurements [46]. A cubic spline data smoothing has been applied on extracted load-local displacement data with a smoothing parameter equal to 0.9995 [47].

## 3. Results and discussion

The evolution of COD during a complete cycle (loading and unloading) at 60 μm behind the crack-tip for different crack lengths in all samples is shown in Fig. 8. For the specimens not subjected to OL, the maximum COD in a cycle increases approximately in a linear manner with the crack length (Figs. 8a and 7c). There is a more drastic increment as the crack grows in the COD for high baseline load (Fig. 8a) than for the low baseline load (Fig. 8c), as one would expect. An increment of 54 MPa and 47 MPa in axial and shear stress between sample S3 and sample S1 (see Table 3) makes the COD rate increasing 52 times faster. Fig. 8 also shows a larger overall scattering of the COD data in low baseline loads (Figs. 8c and 7d) compared to high baseline loads (Fig. 8a and b). This is probably due to the lower signal to noise ratio of the DIC data in the low load experiments.

The effect of applying an axial-torsional overload of 40% on the evolution of COD is clear in Figs. 8a and 7b. For high baseline loads without an OL, the maximum COD measured at the end of the test (crack length ~1.4 mm) is 7.3 μm (Fig. 8a) and with an OL, the equivalent COD is 2.6 μm (Fig. 8b). That is, the 40% OL produced a reduction in the maximum COD by the end of the test of 64%. For low baseline loads, the maximum COD values at the end of the text are 3.4 μm (Fig. 8c) and 2.1 μm (Fig. 8d) for the tests without and with OL, respectively. That is, a 38% reduction caused by the 100% OL on the low baseline load. In terms of COD, the reduc-

[1] For interpretation of color in Fig. 8, the reader is referred to the web version of this article.

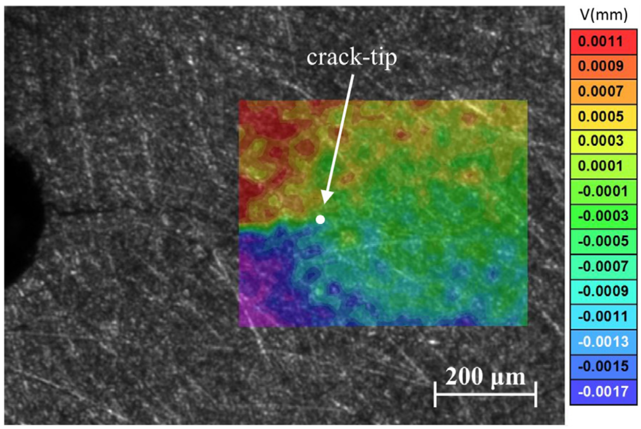


**Fig. 7.** The position of the area of interest for deriving the displacement field ahead of a crack with the length of 0.669 mm after 53,500 cycles (sample S2). The image has been rotated, so that the crack line becomes horizontal.

tion in COD is more pronounced in the high load and 40% OL than in the low load and 100% OL.

Fig. 8b shows that soon after applying the OL on the high load sample (S2), the COD falls from ~2 μm to ~1.2 μm. After the crack grows 384 μm (total crack length = 1.057 mm), the COD is reduced further to around 0.8 μm. When the crack has extended by 335 μm (total crack length = 1.392 mm), the COD increases to ~2.6 μm. The equivalent COD for the non-overloaded sample subjected to similar loads is 7.3 μm (Fig. 8a).

The maximum COD over a cycle is a useful parameter to understand the stage of the crack growth. The acceleration stage is not captured in Figs. 8b and 7d because for the level of magnification in use, it was not possible to image the crack-tip region during the OL cycle. The decrease in COD 5 cycles after applying the OL (yellow curve with square markers in Fig. 8b) indicates that the crack is in the retardation stage. After a further 6210 cycles (blue curve with diamond markers in Fig. 8b) the even lower COD values reveal that the crack is still well in the retardation stage. A comparison between the latest COD measurement in the overloaded specimens (red curve with circle markers in Fig. 8a and b) suggests that 9160 cycles after the OL the crack is still in the retardation stage. This is also in agreement with the crack growth curve in the OL case being clearly below the non-OL curve in Fig. 6a.

A closer look at the COD behaviour of S4 sample (Fig. 8d) shows that after applying the overload there has been a slight increase in the $COD_{max}$ since it raised from ~1.8 μm to ~2.1 μm at the crack length of 0.811 mm (point C in Fig. 6b). It should be noted here that large crack wake opening due to overload made it impossible to position the virtual extensometer at the exact location as for pre-overloading measurements. $COD_{max}$ has then decreased to ~1.8 μm at the crack length of 0.852 mm which is corresponding to point D in Fig. 6b. Subsequent crack growth makes the $COD_{max}$ to increase up to ~2 μm when the crack length is 1.443 mm (point E in Fig. 6b). It can be seen that applying the overload on sample S4, resulted in a 39% decrease in the $COD_{max}$ compared to the reference sample (S3) at the same crack length.

Larger COD values are indicative of higher cyclic damage in the material. Accordingly, COD can be used as an estimation of the

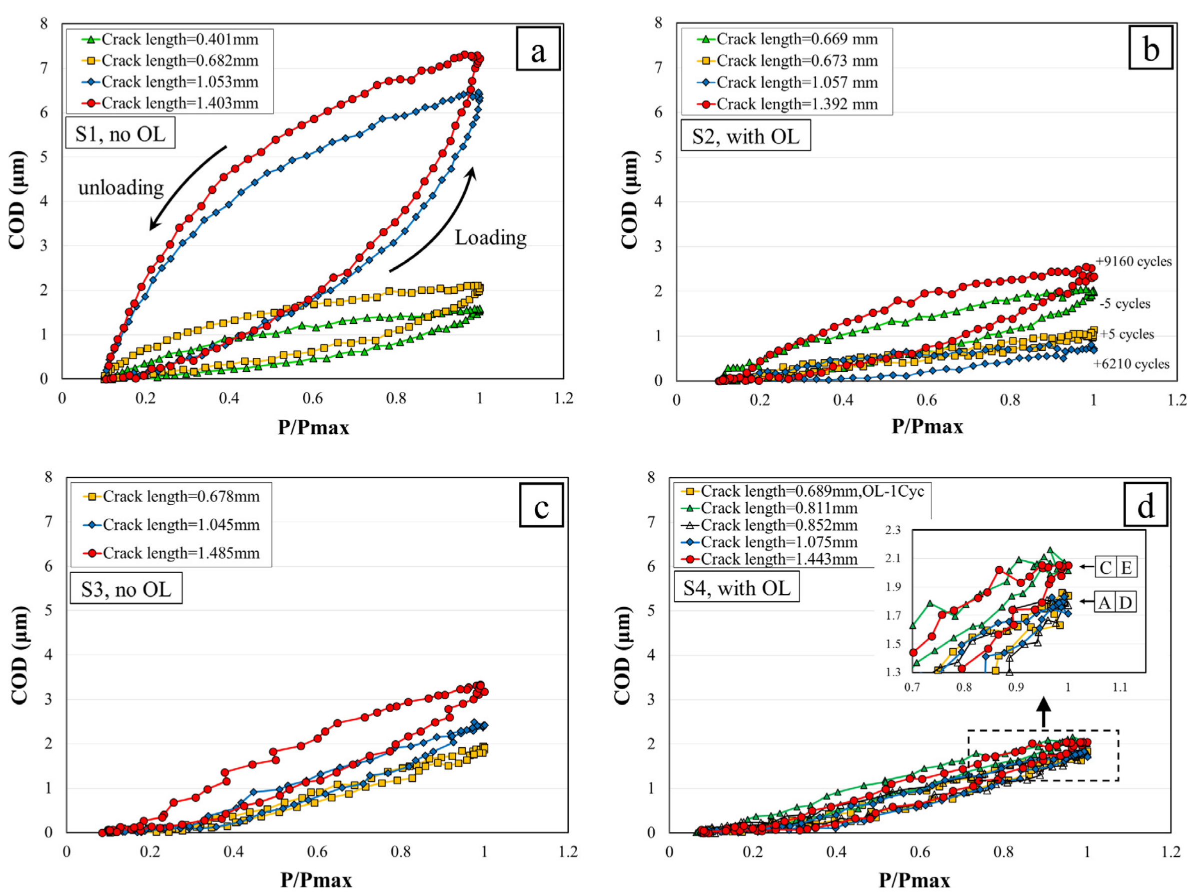


**Fig. 8.** COD behaviour during loading and unloading cycle for different crack lengths of specimens. The number of cycles before and after overload where overload cycle was considered as 0 cycles, are shown in the graph b.

driving force [48]. The shielding effect of the OL is clear after comparing COD results with and without OL.

A summary of the opening load estimated following the procedure described in previous section is shown in Table 4. It can be seen that $P_{op}$ for S1 is 19% of the $P_{max}$, whereas $P_{op}$ for S2 sample, which has experienced an overload cycle, is 27% of the $P_{max}$. Regarding samples S3 and S4 which were tested under a lower baseline load, the overload cycle only increased $P_{op}$ slightly at the longest crack length. That is, $P_{op}$ for S3 (without OL) is 29% of $P_{max}$, whereas it is 31% of $P_{max}$ for sample S4 (overloaded). On the other hand, $P_{op}$ of sample S3 is 53% higher than that of S1 with the same crack length. Both samples were tested under equal axial and torsional load ratio. The $P_{op}$ increment induced by the OL is larger for low loads than for high loads (Table 4). This agrees well with the change that the OL produces in the growth rate (Fig. 6). The difference between the OL and the non-OL curves in crack growth rate is larger for low loads (Fig. 6a) than for high loads (Fig. 6b). Thus, crack growth rate data correlate satisfactorily with opening loads.

The overload seems to have a double influence on the COD: it decreases the overall COD value and also it modifies the shape of the COD curve (Figs. 8b and d). This shape modification consists of the COD curve having a change in slope at a certain load, often referred to as knee [49,50]. This modification appears to be more evident for low loads (Fig. 8b).

Table 4 also shows higher values of $P_{op}$ for low baseline load samples (S3 and S4). This is probably due to samples S3 and S4 being subjected to a higher OL factor than samples S1 and S2 (see Table 3) and observed previously [51].

Table 5 shows the evaluated SIFs and corresponding $COD_{max}$ for two different crack lengths on each sample. It can be seen that $\Delta K_I$ and $\Delta K_{II}$ increase as the crack grows from 0.682 mm to 1.053 mm for sample S1 and from 0.675 mm to 1.045 mm for sample S3. Table 5 also shows that while a crack growth of 0.37 mm in S1 resulted in 26.8 MPa $\sqrt{m}$ increase in $\Delta K_I$, a much smaller increase in $\Delta K_I$ was observed (2.5 MPa $\sqrt{m}$) for a similar crack growth (0.39 mm) in the overloaded S2. $COD_{max}$ values in Table 5 indicate that the initial condition before applying the overload on samples S2 and S4 was equivalent to the corresponding reference samples S1 and S3. It can be seen that applying the overload drastically reduced the $COD_{max}$ value of S2. For the second crack length shown in Table 5, the $COD_{max}$ raised to 6.3 μm in S1 and, due to the overload effect, $COD_{max}$ decreased to 0.7 μm in S2. A similar behaviour can be seen for sample S4. That is, the overload inverted the trend normally followed as the crack grows; for a similar baseline load, the $COD_{max}$ increases as the crack grows. However, if an overload is applied, COD decreases as the crack grows, as long as the crack-tip is within the zone of influence of the overload.

For the non-OL specimens, $\Delta K_I$ (Table 5) follows a similar trend to the COD (Fig. 8). For a crack growth of ~370 μm, the COD increases by a factor of 3 in S1 and a factor of 1.7 in S3. Regarding the SIF, $\Delta K_I$ increases by a factor of 2.8 in S1 and a factor of 1.7 in S3. The OL effect is more visible in the COD data than in the $\Delta K_I$ data. Figs. 8b and 7d show that applying an OL reduces the COD values, as long as the crack is within the retardation stage. However, for the ~370 μm crack growth studied, applying an OL does not reduce the $\Delta K_I$. Nevertheless, the increase in $\Delta K_I$ is much smoother for the OL tests than for the non-OL tests. Estimated $\Delta K_{II}$ values follow a similar trend to $\Delta K_I$ values. The small differences in the trend of $\Delta K_I$ and $\Delta K_{II}$ values are probably due to the crack changing its orientation through the experiment [31] as a consequence of crack-tip plasticity [52], loading direction and microstructure.

**Table 4**
Crack opening loads in a complete cycle.

| Sample | $P_{op}/P_{max}$ |
|---|---|
| S1 | 0.19 |
| S2 | 0.27 |
| S3 | 0.29 |
| S4 | 0.31 |

**Table 5**
Summary of the SIFs estimated for different samples and different crack lengths.

| Specimen | Crack length (mm) | $COD_{max}$ (μm) | $\Delta K_I$ (MPa $\sqrt{m}$) | $\Delta K_{II}$ (MPa $\sqrt{m}$) |
|---|---|---|---|---|
| S1 | 0.682 | 2.1 | 13.2 | 24.5 |
| | 1.053 | 6.3 | 36.8 | 40.0 |
| S2 | 0.669 | 2.0 | 13.1 | 20.4 |
| | 1.057 | 0.7 | 15.6 | 25.3 |
| S3 | 0.678 | 1.9 | 11.8 | 0.2 |
| | 1.045 | 2.4 | 19.7 | 0.3 |
| S4 | 0.689 | 1.9 | 11.9 | 1.6 |
| | 1.075 | 1.8 | 14.0 | 3.7 |

## 4. Conclusions

In this paper, the effect of applying overload cycle on the behaviour of a crack under cyclic biaxial loading is studied with DIC technique. It is observed that applying 100% overload on a sample under low cyclic loads (S4), delayed the appearance of the retardation stage. COD examinations shows the classical sequences of overload, including acceleration and retardation. For the level of magnification employed, it was not possible to collect DIC data in the recovery stage. A hybrid method including fitting the experimental displacement data to analytical solutions based on Wiliams' series development was also used for studying the biaxial fatigue cracks. This allowed the mixed-mode SIF ($\Delta K_I$ and $\Delta K_{II}$) to be estimated on samples under different load levels, with and without applying overload. Results showed that a slower increment in $\Delta K_I$ as the crack grows for the OL case, compared to the non-OL case.

## Acknowledgements

Financial support of Junta de Andalucía through Proyectos de Excelencia grant reference TEP-3244; and the University of Malaga through Campus de Excelencia Internacional del Mar (CEIMAR) through Lineas Emergentes program and for providing PhD scholarship is greatly acknowledged.

## References

[1] Anderson TL. Fracture mechanics fundamentals and applications. 2nd ed. CRC Press; 1995.
[2] ASTM E399-90: standard test method for plane-strain fracture toughness of metallic materials. Am. Soc. Test. Mater. Annu. B. Stand., vol. 3; 1991. p. 451–85.
[3] Suresh S. Fatigue of materials. 2nd ed. New York: Cambridge University Press; 1998.
[4] Ramesh K, Gupta S, Kelkar AA. Evaluation of stress field parameters in fracture mechanics by photoelasticity - revisited. Eng Fract Mech 1997;56(1):25–45.
[5] Díaz FA, Yates JR, Patterson EA. Some improvements in the analysis of fatigue cracks using thermoelasticity. Int J Fatigue 2004;26:365–76.
[6] Nowell D, Paynter RJH, De Matos PFP. Optical methods for measurement of fatigue crack closure: moiré interferometry and digital image correlation. Fatigue Fract Eng Mater Struct 2010;33:778–90.
[7] McNeill SR, Peters WH, Sutton MA. Estimation of stress intensity factor by digital image correlation. Eng Fract Mech 1987;28(1):101–12.
[8] Smith J, Bassim MN, Liu CD, Holden TM. Measurement of crack tip strains using neutron diffraction. Eng Fract Mech 1995;52(5):843–51.

[9] Lopez-Crespo P et al. Overload effects on fatigue crack-tip fields under plane stress conditions: surface and bulk analysis. Fatigue Fract Eng Mater Struct 2013;36:75–84.
[10] Sutton MA, McNeill SR, Helm JD, Chao YJ. Advances in two-dimensional and three-dimensional computer vision. In: Rastogi PK, editor. Photomechanics. Berlin, Heidelberg: Springer; 2000. p. 323–72.
[11] Pan B, Qian K, Xie H, Asundi A. Two-dimensional digital image correlation for in-plane displacement and strain measurement: a review. Meas Sci Technol 2009;20(6):62001.
[12] Patterson EA, Olden EJ. Optical analysis of crack tip stress fields: a comparative study. Fatigue Fract Eng Mater Struct 2004;27(January):623–35.
[13] Sutton MA, Orteu J-J, Schreier HW. Image Correlation for shape, motion and deformation measurements. New York: Springer; 2009.
[14] Sanford RJ, Dally JW. A general method for determining mixed-mode stress intensity factors from isochromatic fringe patterns. Eng Fract Mech 1979;11:621–33.
[15] Yoneyama S, Ogawa T, Kobayashi Y. Evaluating mixed-mode stress intensity factors from full-field displacement fields obtained by optical methods. Eng Fract Mech 2007;74:1399–412.
[16] Réthoré J, Gravouil A, Morestin F, Combescure A. Estimation of mixed-mode stress intensity factors using digital image correlation and an interaction integral. Int J Fract 2005;132:65–79.
[17] López-Crespo P, Burguete RL, Patterson EA, Shterenlikht A, Withers PJ, Yates JR. Study of a crack at a fastener hole by digital image correlation. Exp Mech 2009;49:551–9.
[18] Nowell D, De Matos PFP. Application of digital image correlation to the investigation of crack closure following overloads. Procedia Eng 2010;2(1):1035–43.
[19] Yusof F, Lopez-Crespo P, Withers PJ. Effect of overload on crack closure in thick and thin specimens via digital image correlation. Int J Fatigue 2013;56:17–24.
[20] Christopher CJ, James MN, Patterson EA, Tee KF. Towards a new model of crack tip stress fields. Int J Fract 2007;148(4):361–71.
[21] Colombo C, Vergani L. A numerical and experimental study of crack tip shielding in presence of overloads. Eng Fract Mech 2010;77(11):1644–55.
[22] Vasco-Olmo JM, Díaz FA, Patterson EA. Experimental evaluation of shielding effect on growing fatigue cracks under overloads using ESPI. Int J Fatigue 2016;83:117–26.
[23] Lopez-Crespo P, Mostafavi M, Steuwer A, Kelleher JF, Buslaps T, Withers PJ. Characterisation of overloads in fatigue by 2D strain mapping at the surface and in the bulk. Fatigue Fract Eng Mater Struct 2016;39(8):1040–8.
[24] Leser WP, Newman JA, Johnston WM. Fatigue crack closure analysis using digital image correlation. NASA/TM-2010-216695; 2010.
[25] Carroll RCJ, Efstathiou C, Lambros J, Sehitoglu H, Hauber B, Spottswood S. Investigation of fatigue crack closure using multiscale image correlation experiments. Eng Fract Mech 2009;76:2384–98.
[26] Sander M, Richard H. Experimental and numerical investigations on the influence of the loading direction on the fatigue crack growth. Int J Fatigue 2006;28(5–6):583–91.
[27] Shanyavsky AA, Orlov EF. Fracture surface development in an overloaded D16T Al-alloy subjected to biaxial loading. A fractographic analysis. Fatigue Fract Eng Mater Struct 1997;20(2):151–66.
[28] Shanyavskiy A. Fatigue cracking simulation based on crack closure effects in Al-based sheet materials subjected to biaxial cyclic loads. Eng Fract Mech 2011;78(8):1516–28.
[29] Langseth BM, Lindholm US, Larsen PK, Lian B. Strain-rate sensitivity of mild steel grade St-52-3N. J Eng Mech 1991;117(4):719–32.
[30] Chaves V. Ecological criteria for the selection of materials in fatigue. Fatigue Fract Eng Mater Struct 2014;37(9):1034–42.
[31] Lopez-Crespo P, Moreno B, Lopez-Moreno A, Zapatero J. Study of crack orientation and fatigue life prediction in biaxial fatigue with critical plane models. Eng Fract Mech 2015;136:115–30.
[32] Lopez-Crespo P, Garcia-Gonzalez A, Moreno B, Lopez-Moreno A, Zapatero J. Some observations on short fatigue cracks under biaxial fatigue. Theor Appl Fract Mech 2015;80:96–103.
[33] Lopez-Crespo P, Moreno B, Lopez-Moreno A, Zapatero J. Characterisation of crack-tip fields in biaxial fatigue based on high-magnification image correlation and electro-spray technique. Int J Fatigue 2015;71:17–25.
[34] Shih TT, Wei RP. A study of crack closure in fatigue. NASA CR-2319, Wachington, D.C.; 1973.
[35] ASTM E647-00: standard test method for measurement of fatigue crack growth rates. Am. Soc. Test. Mater. Annu. B. Stand.; 1999.
[36] de Matos PFP, Nowell D. Experimental and numerical investigation of thickness effects in plasticity-induced fatigue crack closure. Int J Fatigue 2009;31(11–12):1795–804.
[37] Sutton MA, Zhao W, McNeill SR, Helm JD, Piascik RS, Riddell WT. Local crack closure measurements: development of a measurement system using computer vision and a far-field microscope. In: McClung RC, Newman JC, editors. Advances in fatigue crack closure measurement and analysis: second volume, ASTM STP 1343. West Conshohocken, PA. p. 145–56.
[38] Carlson RL, Kardomates GA, Bates PR. The effects of overloads in fatigue crack growth. Int J Fatigue 1991;13(6):453–60.
[39] Miller KJ. The behaviour of short fatigue cracks and their initiation, Part I – a review of two recent books. Fatigue Fract Eng Mater Struct 1987;10(1):75–91.
[40] Matsuoka S, Tanaka K, Kawahara M. The retardation phenomenon of fatigue crack growth in HT80 steel. Eng Fract Mech 1976;8(3):507–23.
[41] Williams ML. On the stress distribution at the base of a stationary crack. J Appl Mech 1957;24(3):109–14.
[42] Zanganeh M, Lopez-Crespo P, Tai YH, Yates JR. Locating the crack tip using displacement field data: a comparative study. Strain 2013;49:102–15.
[43] Mokhtarishirazabad M, Lopez-Crespo P, Moreno B, Lopez-Moreno A, Zanganeh M. Evaluation of crack-tip fields from DIC data: a parametric study. Int J Fatigue 2016;89:11–9.
[44] Lopez-Crespo P, Shterenlikht A, Patterson EA, Yates JR, Withers PJ. The stress intensity of mixed mode cracks determined by digital image correlation. J Strain Anal Eng Des 2008;43:769–80.
[45] Skorupa M, Beretta S, Carboni M, Machniewicz T. An algorithm for evaluating crack closure from local compliance measurements. Fatigue Fract Eng Mater Struct 2002;25(3):261–73.
[46] Vasco-Olmo JM, Díaz FA. Experimental evaluation of the effect of overloads on fatigue crack growth by analysing crack tip displacement fields. Eng Fract Mech 2016;166:82–96.
[47] Pollock DSG. Smoothing with cubic splines. In: Signal processing and its applications, handbook of time series analysis, signal processing, and dynamics. London: Academic Press; 1999. p. 293–322.
[48] Sutton MA, Zhao W, McNeill SR, Helm JD, Piascik RS, Riddell WT. Local crack closure measurements: development of a measurement system using computer vision and a far-field microscope. Adv. Fatigue Crack Clos. Meas. Anal. ASTM STP 1343; 1999. p. 145–56.
[49] Joyce JA, Sutton GE. An automated method of computered-controlled low-cycle fatigue crack growth testing using the elastic-plastic parameter cyclic J". In: Cullen WH, Landgraf RW, Kaizand LR, Underwood JH, editors. Automated test methods for fracture and fatigue crack growth. American Society for Testing and Materials; 1985. p. 225–47.
[50] Lopez-Crespo P, Shterenlikht A, Yates JR, Patterson EA, Withers PJ. Some experimental observations on crack closure and crack-tip plasticity. Fatigue Fract Eng Mater Struct 2009;32:418–29.
[51] de Matos PFP, Nowell D. On the accurate assessment of crack opening and closing stresses in plasticity-induced fatigue crack closure problems. Eng Fract Mech 2007;74:1579–601.
[52] Lopez-Crespo P, Pommier S. Numerical analysis of crack tip plasticity and history effects under mixed mode conditions. J Solid Mech Mater Eng 2008;2(12):1567–76.